

**EPITHELIAL ELECTROPHYSIOLOGY USING INTRACELLULAR ROBOTICS  
AND EXTRACELLULAR IMPEDANCE SPECTROSCOPY**

A Dissertation  
Presented to  
The Academic Faculty

By

Colby Foster Lewallen

In Partial Fulfillment  
of the Requirements for the Degree  
Doctor of Philosophy in the  
School of Mechanical Engineering

Georgia Institute of Technology

December 2021

© Colby Foster Lewallen 2021

**EPITHELIAL ELECTROPHYSIOLOGY USING INTRACELLULAR ROBOTICS  
AND EXTRACELLULAR IMPEDANCE SPECTROSCOPY**

Thesis committee:

Dr. Craig R. Forest  
George W. Woodruff School of Mechanical Engineering  
*Georgia Institute of Technology*

Dr. Krishnendu Roy  
Coulter Department of Biomedical Engineering  
*Georgia Institute of Technology*

Dr. Jun Ueda  
George W. Woodruff School of Mechanical Engineering  
*Georgia Institute of Technology*

Dr. Kapil Bharti  
Ocular and Stem Cell Translational Research Section  
*National Eye Institute*

Dr. C. Ross Ethier  
George W. Woodruff School of Mechanical Engineering  
*Georgia Institute of Technology*

Date approved: December 9, 2021

## ACKNOWLEDGMENTS

I would like to thank my advisor, Craig, for providing both emotional and scientific guidance. I have learned more than I ever expected during my degree, and I would have missed out on so much that I now cherish if you had not emailed me out of the blue during my first semester at Georgia Tech.

I would like to thank my committee members, Jun, Krish, Ross, and Kapil for their thoughtful questions and feedback during my proposal and defense. In particular, I would like to thank Kapil for hosting me every summer in Bethesda. I was able to immerse myself amongst scientists of the highest caliber, and truly learn from the best; an experience I will never forget.

Thank you to all the members of the Precision Biosystems lab with whom I've had the pleasure of working: Bo, Greg, Caitlin, Ilya, Will, Tim, Corey, Mighten, Mercedes, Amanda, Sofia, Aditi, Max, Riley, Nina, Athena, and Mohamed. I owe so much of who I am now to the friendships I formed with all of you.

Thanks to the members of the National Eye Institute lab with whom I spent nearly every summer with: Ruchi, Mitra, Francesca, Russ, Devika, and Malika. I had so much fun getting to learn from you in lab and with you after hours. Special thanks to Davide, Eric, and Dominik for sparing critical time and resources for to help me reach the finish line of my PhD. Extra special thanks to Arvydas and Qin, who have provided exhaustive mentorship over the last 5.5 years of my PhD. Without your guidance, I would surely still be lost.

Finally, I would like to thank my family for taking my late night phone calls to talk about life, and even research, but most importantly, for supporting me every step of the way as I pursued this crazy dream of mine.

## TABLE OF CONTENTS

<b>Acknowledgments</b> . . . . .	iii
<b>List of Tables</b> . . . . .	vii
<b>List of Figures</b> . . . . .	viii
<b>List of Acronyms</b> . . . . .	xi
<b>Summary</b> . . . . .	xii
<b>Chapter 1: Introduction and Background</b> . . . . .	1
1.1 Cell membranes: ion transport and phospholipid organization . . . . .	1
1.2 Epithelia: structure, function, and electrophysiology . . . . .	7
1.3 Induced pluripotent stem cells . . . . .	13
<b>Chapter 2: Develop a robot capable of automated intracellular measurement of epithelial electrophysiology</b> . . . . .	15
2.1 Motivation . . . . .	15
2.2 Methods . . . . .	17
2.2.1 Primary hFRPE cell culture . . . . .	17
2.2.2 Generation, differentiation, and characterization of human iPSC-RPE	18
2.2.3 Pipette fabrication . . . . .	18

2.2.4	Cell culture medium and physiology solution compositions . . . . .	19
2.2.5	Tissue preparation . . . . .	19
2.2.6	Electrophysiology experiments . . . . .	20
2.2.7	Pipette position algorithm . . . . .	22
2.3	Results and discussion . . . . .	25
2.3.1	Break-in algorithm . . . . .	25
2.3.2	Validation of cell health . . . . .	27
2.4	Conclusions . . . . .	31
<b>Chapter 3: Develop a mathematical model to measure the previously unobservable apical and basolateral membrane properties using extracellular electrochemical impedance spectroscopy . . . . .</b>		<b>33</b>
3.1	Motivation . . . . .	33
3.2	Methods . . . . .	34
3.2.1	Intracellular electrophysiology equations . . . . .	34
3.2.2	A workflow for the direct solution of membrane-specific properties .	40
3.3	Results and discussion . . . . .	42
3.3.1	Theory validation using model cell circuit . . . . .	42
3.3.2	Membrane-specific response of RPE induced by apical ATP . . . . .	46
3.4	Conclusions . . . . .	50
<b>Chapter 4: Apply electrochemical impedance spectroscopy to elucidate membrane specific properties of epithelia using extracellular electrophysiology . . . . .</b>		<b>51</b>
4.1	Motivation . . . . .	51
4.1.1	Methods . . . . .	56

4.1.2	Immunostaining . . . . .	56
4.1.3	Scanning electron microscopy . . . . .	57
4.1.4	Mathematical modeling . . . . .	57
4.2	Results and discussion . . . . .	60
4.2.1	Chamber design and extracellular epithelial properties . . . . .	60
4.2.2	Extracellular EIS as an analog for intracellular properties . . . . .	70
4.2.3	Briefly exploring the potential links between cell morphology and capacitance . . . . .	74
4.3	Conclusions . . . . .	78
<b>Chapter 5: Research conclusions and future work . . . . .</b>		<b>80</b>
5.1	Summary of major contributions . . . . .	80
5.2	Future work . . . . .	81
<b>References . . . . .</b>		<b>84</b>

## LIST OF TABLES

2.1	Stable hFRPE electrical properties reported in the literature (manual) compared with values obtained with the automated method. . . . .	28
3.1	Selected resistance and capacitance values used in the model circuit to validate the intracellular technique for extracting membrane-specific properties of epithelia. . . . .	43
3.2	Measured resistance and capacitance values from the model circuit used to validate the technique for extracting membrane-specific properties of epithelia. . . . .	45

## LIST OF FIGURES

1.1	Simplified phospholipid bilayer . . . . .	2
1.2	Cell membrane with embedded channels . . . . .	3
1.3	A circuit model for the transfer of charged ions across a cell membrane. . .	5
1.4	Schematics of the connection between epithelial structure and the equivalent charge transfer pathways. . . . .	8
1.5	Hans Üssing's chamber . . . . .	9
1.6	Sheldon Miller's modified Üssing chamber . . . . .	11
1.7	Picture of retinal pigment epithelia (RPE) with photoreceptors and intracellular pipette for scale . . . . .	12
2.1	SolidWorks render of the Üssing chamber . . . . .	20
2.2	Five stage break in algorithm . . . . .	23
2.3	Indent depth break in probability . . . . .	25
2.4	Buzz depth break in probability . . . . .	26
2.5	hfRPE and induced pluripotent stem cell (iPSC)-RPE evoked responses compared with manual technique . . . . .	30
3.1	A model circuit, constructed out of resistors and capacitors, used to validate the direct measurement of epithelial circuit terms. . . . .	42
3.2	Power spectral density plot used to measure membrane-specific properties of epithelia. . . . .	44

3.3	Representative impedance ratio and Nyquist diagram used to measure membrane-specific properties of epithelia. . . . .	45
3.4	Fitting error magnitude for all permutations of the model cell using the intracellular measurement technique. . . . .	46
3.5	Theoretical mechanisms of RPE response to apical adenosine triphosphate (ATP). . . . .	47
3.6	Example time series data with membrane-specific resistances extracted. . .	48
3.7	Example time series data with membrane-specific capacitances extracted. .	49
4.1	Two circuits that fit electrochemical impedance spectroscopy (EIS) measurements of epithelia with near-perfect correlation. . . . .	52
4.2	Schiffederdecker’s electrical circuit model for epithelia . . . . .	54
4.3	Picture of custom chamber used to study intact, 12-well Transwells. . . . .	61
4.4	Schematic of custom chamber used to study intact, 12-well Transwells. . . .	62
4.5	Perfusion versus Üssing chamber extracellular electrophysiological differences. . . . .	64
4.6	All normalized total tissue resistance ( $R_t$ ) response of iPSC-RPE (Z8) to apical ATP exposure. . . . .	65
4.7	All normalized tissue potential responses (transepithelial potential (TEP)) of iPSC-RPE (Z8) to apical ATP exposure. . . . .	66
4.8	All normalized tissue capacitance response ( $C_t$ ) of iPSC-RPE (Z8) to apical ATP exposure. . . . .	67
4.9	All normalized extracellular time constant ratios ( $\tau_1/\tau_2$ ) for iPSC-RPE (Z8) response to apical ATP exposure. . . . .	69
4.10	Example Nyquist diagrams of iPSC-RPE (Z8) before, during, and after ATP exposure. . . . .	71
4.11	Quantitative comparison between extracellular EIS and the voltage divider ratio ( $a$ ). . . . .	73
4.12	Extracellular EIS properties for 3 iPSC-RPE cell lines. . . . .	75

4.13	REShAPE morphology from fluorescent imaging of a Transwell punch-out measured with EIS. . . . .	76
4.14	An example of how EIS and REShAPE can be leveraged to investigate the relationships between tissue capacitance and cell cross-sectional area. . . .	77

## LIST OF ACRONYMS

<b>AMD</b>	age-related macular degeneration
<b>ATP</b>	adenosine triphosphate
<b>CF</b>	cystic fibrosis
<b>EIS</b>	electrochemical impedance spectroscopy
<b>EMF</b>	electromotor force
<b>hESC</b>	human embryonic stem cell
<b>hf</b>	human fetal
<b>hPSC</b>	human pluripotent stem cell
<b>iPSC</b>	induced pluripotent stem cell
<b>LP</b>	light peak
<b>NEI</b>	National Eye Institute
<b>PSD</b>	power spectral density
<b>QC</b>	quality control
<b>RPE</b>	retinal pigment epithelia
<b>SEM</b>	scanning electron microscope
<b>SRS</b>	sub retinal space
<b>TEC</b>	transepithelial capacitance
<b>TEM</b>	transmission electron microscope
<b>TEP</b>	transepithelial potential

## SUMMARY

Epithelia are barrier-type cells that regulate the transport of materials into and out of the body. Dysfunction of these cells is implicated in numerous diseases such as cystic fibrosis, age-related macular degeneration, and diabetes. Since the discovery of induced pluripotent stem cells (iPSCs) by Takahashi and Yamanaka in 2006, scientists around the world have begun utilizing iPSC-based therapies to halt, and potentially reverse, the progression of these diseases. For epithelia-based therapies, validation of tissue polarity and function is an essential component of a thorough physiological exam, and are commonly performed electrochemically, but existing methods are some combination of (1) destructive to the cells, (2) incomplete, (3) extremely difficult, and (4) low throughput (e.g., 1-2 tissues/day). Therefore, in this work, novel tools and measurement techniques were developed to study epithelial cell function that addresses these issues.

For example, an algorithm that automates the insertion of a pipette into the cytoplasm of a cell was developed (chapter 2). This algorithm outperforms a highly trained expert at a much lower operator skill level; enabling more labs to explore the physiology, drug toxicity, and disease processes of epithelia. In addition, a new mathematical model was developed that combines a technique called electrochemical impedance spectroscopy (EIS) with intracellular voltage data to extract membrane-specific properties of epithelia (chapter 3). Furthermore, experimental data demonstrating an inverse relationship between tissue capacitance and the median cell cross-sectional area is presented (chapter 4). Finally, a mathematical link between membrane-specific properties of epithelia and the time constant ratio, a property that does not require intracellular voltage data, is derived and experimentally tested. This link can act as a bridge between the comprehensive, yet slow and invasive, intracellular measurements and the fast, yet simple, extracellular measurements of epithelial function (chapter 4).

# CHAPTER 1

## INTRODUCTION AND BACKGROUND

### 1.1 Cell membranes: ion transport and phospholipid organization

Reports of investigations into the electrochemical behavior of semi-permeable membranes go back as far as the 4th century BCE when Aristotle described a method for obtaining fresh drinking water from seawater using a sealed wax vessel as a filter [1]. However, it was Ostwald in 1890 who helped kick-start living membrane electrophysiology when he postulated that the observed "electromotive phenomena" in living tissues may arise because they can selectively prevent or permit the passage of ions [2].

To understand how tissues can selectively transport ions, it is imperative to first study the composition of a cell membrane. The outer shell (i.e., membrane) of a cell is composed of a plasma membrane which, itself, is composed primarily of phospholipids. In general, phospholipids are composed of two fatty acids, a phosphate group, and a glycerol molecule. The unique organization and physical chemistry of each phospholipid give rise to the classic, bi-layer, organization of cell membranes and explain many of their most important properties. Specifically, the fatty acid tails of a phospholipid are non-polar molecules that lack the charged groups that would encourage any interactions with water (i.e., *hydrophobic*). Conversely, the phosphate head groups - connected to the tails by a glycerol molecule - are charged or polar and, thus, are very water-soluble (i.e., *hydrophilic*). Because phospholipids combine hydrophilic heads and hydrophobic tails, they will spontaneously organize themselves in the manner shown below when submerged in aqueous solutions (Figure 1.1).

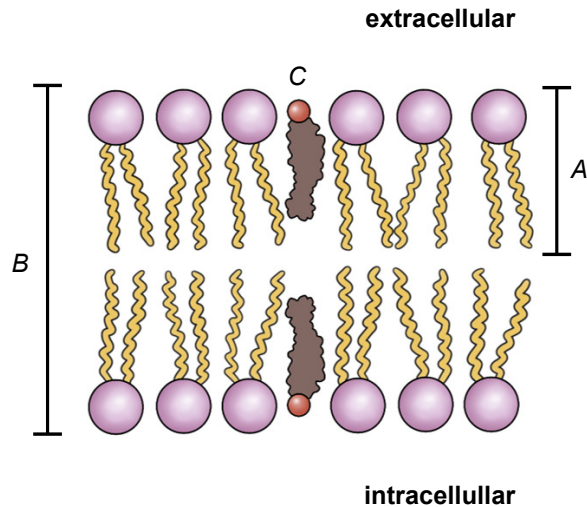


Figure 1.1: Cross-sectional view of a phospholipid bilayer. (A) Identifies the traditional icon for a phospholipid with its characteristic, hydrophobic, twin tails, and a single hydrophilic head. (B) Demonstrates the traditional phospholipid bilayer organization when fully submerged in a water-based solution with the polar head facing out on each surface to interact with water, and with the hydrophobic tails driven inward. (C) Shows cholesterol embedded into the phospholipid membrane. Cholesterol, in particular, is an example of cellular material that contributes to cell membrane stiffness.

In this bilayer configuration, the phospholipids form a membrane that is nearly impermeable to charged, water-soluble substances (e.g.,  $\text{Ca}^{2+}$ ,  $\text{Cl}^-$ ,  $\text{K}^+$ ,  $\text{Na}^+$ ) and large molecules (e.g., sugars and extracellular proteins). For ions to travel through the phospholipid bilayer, it normally requires special proteins embedded within the membrane to create an opening as shown in Figure 1.2.

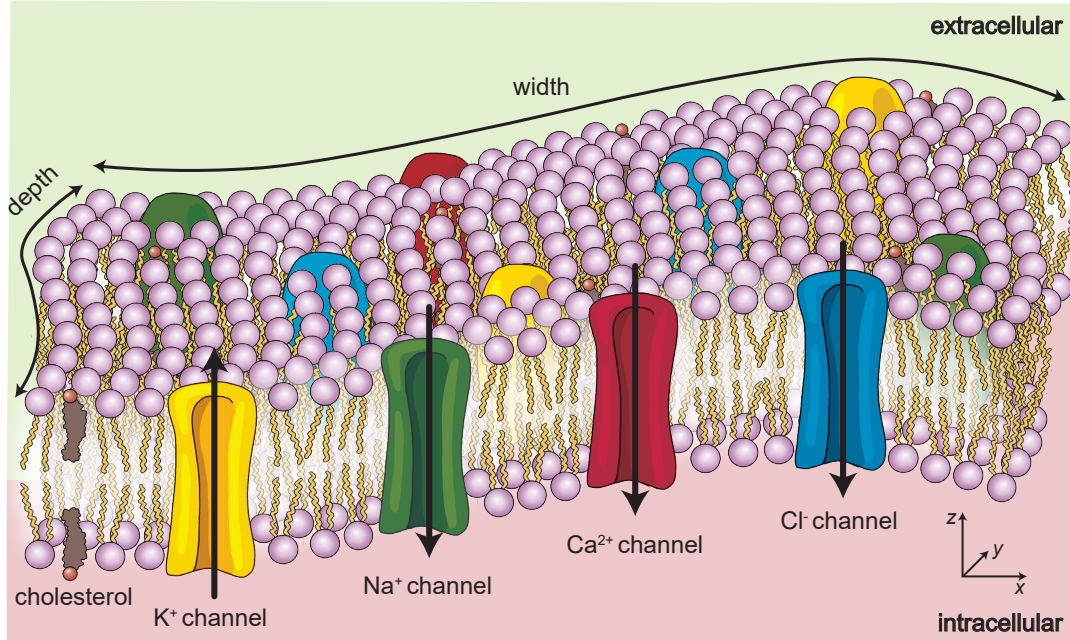


Figure 1.2: Cross-sectional view of a 3D phospholipid bilayer, separating the extracellular and intracellular environments of a cell with embedded proteins that selectively transport  $K^+$ ,  $Na^+$ ,  $Ca^{2+}$ , and  $Cl^-$ .

Given an aqueous solution in a closed system, small, suspended particles tend towards a homogeneous distribution given the sporadic interactions with neighboring particles spurred by temperature-induced vibrations. These interactions amongst ions generate an osmotic pressure that generally results in a flow down the concentration gradient. Furthermore, the net charge of ions within the solution (or applied by external devices) can similarly drive ion flow towards areas of opposite charge. Therefore, the electrochemical potential energy of an ion is equal to the sum of the osmotic pressure and electrostatic potential energy gradients across a membrane as described by the following equation:

$$\Delta\mu_X = RT \ln \left( \frac{[X]_i}{[X]_e} \right) + z_X F (V_i - V_e) \quad (1.1)$$

where  $\Delta\mu$  is the electrochemical potential energy of an ion ( $X$ ). The gas constant ( $R$ ) multiplied by the absolute temperature ( $T$ ) and the natural log of the ratio between the

intracellular and extracellular concentrations ( $[X]_i$  and  $[X]_e$ , respectively) describes the osmotic pressure across the membrane. Additionally, the valence of the ion ( $z_X$ ) multiplied by Faraday's constant ( $F$ ) and the difference between the intracellular and extracellular solution potentials ( $V_i$  and  $V_e$ , respectively) describe the electrostatic potential energy.

When the osmotic pressure and electrostatic forces acting on any ion are at equilibrium,  $\Delta\mu_X = 0$ , and this equation reduces to the membrane equilibrium equation described by Nernst where  $V_i - V_e = V_m$ .

$$V_m = -\frac{RT}{z_X F} \ln \left( \frac{[X]_i}{[X]_e} \right) \quad (1.2)$$

Given the size constraints and number of channels present in a typical membrane, the ion transport rate through the membrane (i.e., ion current,  $I_X$ ) is significantly restricted. To characterize the rate that these ions can transport through a membrane, David Goldman in 1943 presented an explicit solution to the Nernst-Plank equation [3]:

$$I_X = \frac{P_X z_X^2 F^2 V_m}{RT} \left( \frac{[X]_i e^{z_X F V_m / RT} - [X]_e}{e^{z_X F V_m / RT} - 1} \right) \quad (1.3)$$

where  $P_X$  is the permeability - or effective diffusion rate - of an ion through a membrane.

In order to derive this equation, Goldman made the following assumptions:

1. The membrane composition is homogeneous.
2. The electric field through a membrane is constant so that the membrane potential varies linearly across the membrane (*constant field assumption*). In Figure 1.2, this would mean that  $dV/dz \approx V_m/d$  where  $d$  corresponds to the membrane thickness.
3. The permeant ions do not interact with each other during transport (*independence principle*).

4. Permeability does not vary with osmotic or electrostatic driving forces.

With these equations, and assuming that the system is a linear time-invariant system, the flow of ions through a membrane can be modeled with equivalent electrical circuits as shown in Figure 1.3 [4].

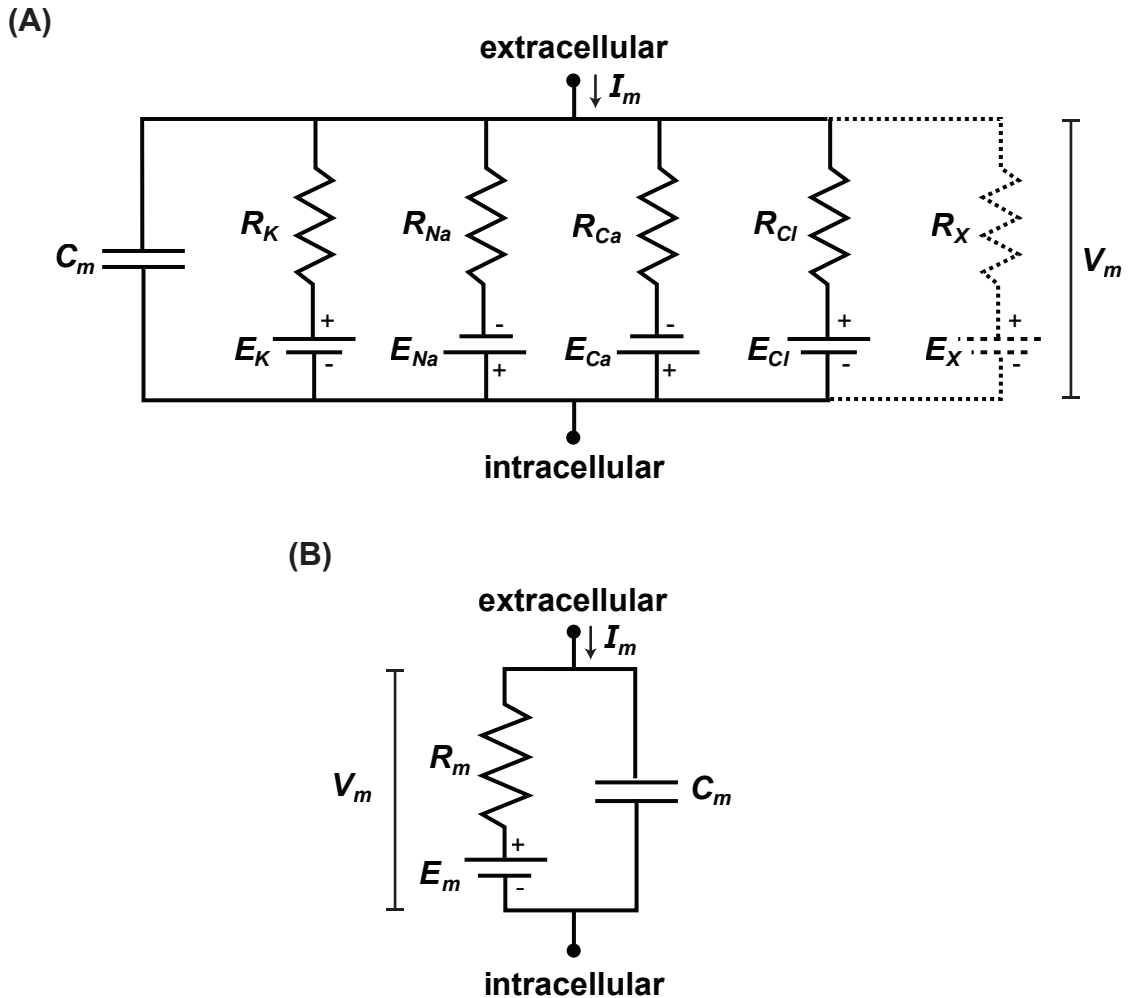


Figure 1.3: A circuit model for the transfer of charged ions across a cell membrane. (A) Circuit model showing how each ion ( $X$ ) transfers charge through unique and distinct pathways, represented by parallel membrane resistances,  $R$ , and equilibrium potentials,  $E$ . The membrane also has a capacity to store charge which is represented by  $C_m$ . (B) The simplified circuit model for a cell membrane combines the resistance and equilibrium potentials for each ion into single terms.

Thus, the net current flowing through the membrane ( $I_m$ ) for  $n$  ions as a function of time ( $t$ ) can be described by:

$$I_m = C_m \frac{dV_m}{dt} + \sum_{X=1}^n I_X \quad (1.4)$$

The capacitance of the membrane arises due to the sections of the membrane that do not permit the free transport of ions (e.g., the phospholipids). In these areas, the charge can accumulate by concentrating local ions near the surface of the membrane. Therefore, the magnitude of membrane capacitance is proportional to the surface area of the solution in contact with the membrane ( $A = \text{width} \times \text{depth}$  in Figure 1.2), the composition of the membrane represented by a dielectric constant ( $\epsilon$ ), and inversely proportional to the membrane thickness ( $d$ ) as shown in:

$$C_m = \frac{\epsilon A}{d} \quad (1.5)$$

When the osmotic and electrostatic forces acting on an ion are not at equilibrium, a current will form ( $I_X$ ) with a magnitude proportional to:

$$I_X = \frac{1}{R_X} (V_m - E_X) \quad (1.6)$$

The circuit shown in Figure 1.3A is a complete representation of how ions flow across a membrane, but, in practice, it is difficult and time consuming to measure. To study Figure 1.3A, the concentration of each ion must be monitored to account for their relative contribution to the overall membrane voltage. This can be performed, for example, by inserting calibrated, ion-specific electrodes in the extracellular and intracellular baths - one for each ion - to track their concentrations. The ion-selective electrodes must be fully reversible (electrochemically) and have a fast reaction rate to be useful for biologically

relevant electrophysiological assays. Selection of suitable electrodes or alternative experimental design can be complicated, and scientists often simplify the circuit to - similarly - reduce the complexity of analysis. This simplified circuit is shown in Figure 1.3B where:

$$\frac{1}{R_m} = \frac{1}{R_K} + \frac{1}{R_{Na}} + \frac{1}{R_{Ca}} + \frac{1}{R_{Cl}} + \dots + \frac{1}{R_X} \quad (1.7)$$

and at steady state (i.e.,  $dV_m/dt = 0$ ):

$$E_m = V_m - I_m R_m \quad (1.8)$$

These equivalent circuit models have become the foundation for the electrophysiological analysis of cell membranes, and similarly are the foundation that this research was built upon.

## 1.2 Epithelia: structure, function, and electrophysiology

The sheet of cells (one or more layers thick) that separate an organism's internal organs from the outside world and line internal organs is called an epithelium. Epithelia are a unique membrane of the body because they form connections with their neighbors that allow them to regulate the transfer of ions, nutrients, and waste products to help maintain critical organism functions. These junctions form the barrier that separates two distinct cell membranes; often called the apical and basolateral (or basal) membranes. The composition of these membranes are often remarkably different, which results in a polarization of the tissue that is used to facilitate critical transport processes (Figure 1.4).

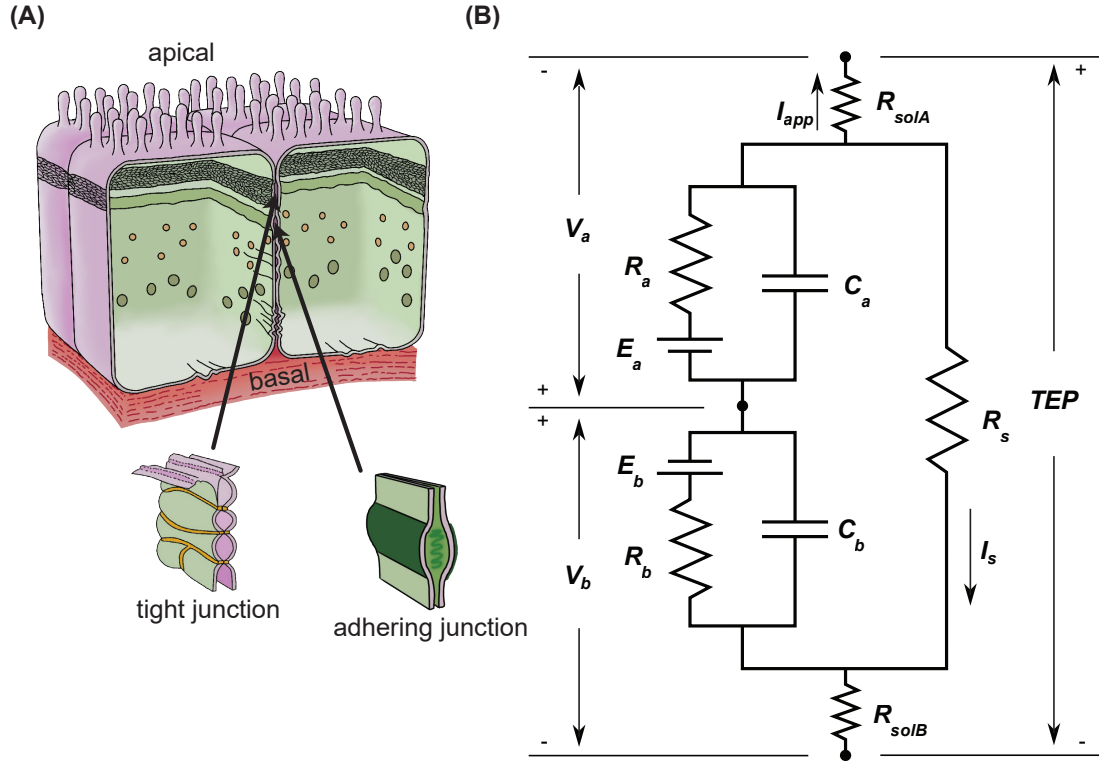


Figure 1.4: Schematics of the connection between epithelial structure and the equivalent charge transfer pathways. (A) 3D model showing the structure of a single layer of epithelia with cutouts highlighting the tight and adhering junctions that help bind each epithelium with the neighboring cells. (B) The equivalent circuit for epithelia summarizes the pathways for ion flux across the cell.  $I_{app}$  is the applied current by an external device,  $I_s$  indicates the shunt current that can arise by active transport processes, TEP represents the net potential gradient across the tissue,  $R_s$  represents the resistance of the shunt pathway for ions to bypass the epithelia by traveling through the tight junctions, and  $R_{solA}$  and  $R_{solB}$  represent the resistance of the apical and basolateral baths, respectively.

Dysfunction of ion-selective behavior in epithelia has been implicated in numerous, common diseases including cystic fibrosis (CF), age-related macular degeneration (AMD), and diabetes [5, 6, 7]. AMD, for example, is one of the most prevalent forms of blindness in elderly people over 60, and is caused by atrophy of the RPE [8, 9, 10, 11, 12, 13, 14]. Thus, ion-selective behavior is a critical function of epithelia and manifests as potential gradients and resistances that can be measured by appropriate devices [2]. Hans Üssing presented such a device in 1951 to study the electrophysiological properties of a living membrane; specifically, the isolated frog skin Figure 1.5 [15]. Üssing's device has since become the

standard platform for studying the electrophysiology of most epithelia.

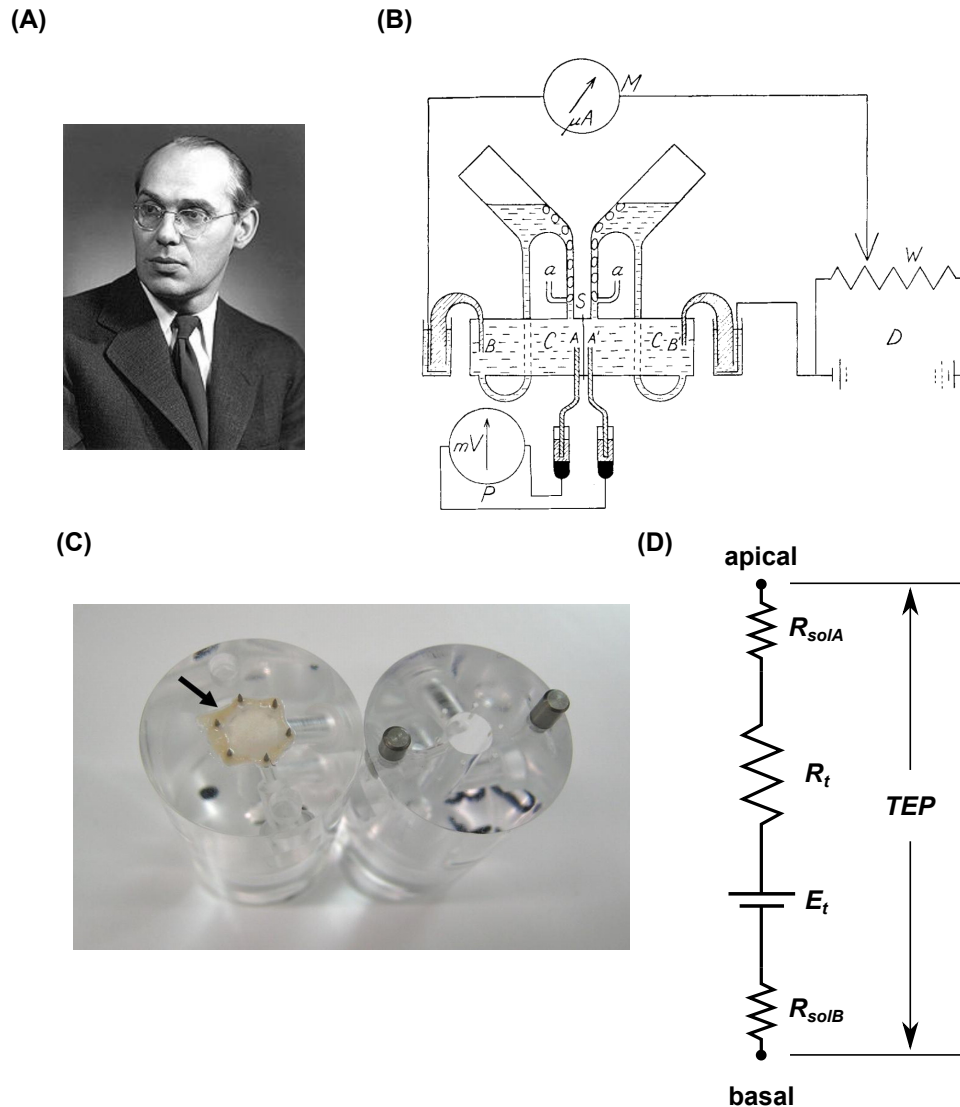


Figure 1.5: The invention of a chamber to study epithelia electrophysiology. (A) Photograph of the inventor, Hans Üssing. (B) A diagram that depicts the chamber design as presented by Han Üssing to study the existence of the sodium pump in frog skin. The frog skin,  $S$ , was clamped between two half chambers,  $C$ , containing solutions of identical composition. By bubbling air through the inlets,  $a$ , oxygen was supplied to the preparation while pH was kept constant by the buffer. The TEP was recorded by  $P$  via agar bridges,  $A$  and  $A'$ . A pair of matched, calomel electrodes were controlled by passing an electric current through the skin via  $Ag|AgCl$  half cells and agar bridges,  $B$ , from an external current source, i.e., a battery,  $D$ , in parallel with a manually operated slide rheostat,  $W$  [15]. (C) Picture of mouse intestine mounted in an Üssing chamber from a paper published in 2009, demonstrating that Üssing's device is still useful today [16]. (D) The equivalent circuit that is measured using the Üssing chamber.  $E_t$  represents the electromotor force (EMF) of the tissue, and  $R_t$  represents the tissue's net resistance to ion transport.

Since the inception of Üssing's chamber, scientists have been working to expand its capabilities and enhance its throughput. For example, Sheldon Miller in 1977 presented a modification to the traditional Üssing chamber that enabled intracellular access for a tiny electrode (100 nm to 200 nm in diameter) – called a pipette – to separately record the potentials of the top and bottom (apical and basal, respectively) membranes of RPE (Figure 1.6 and Figure 1.7) [4].

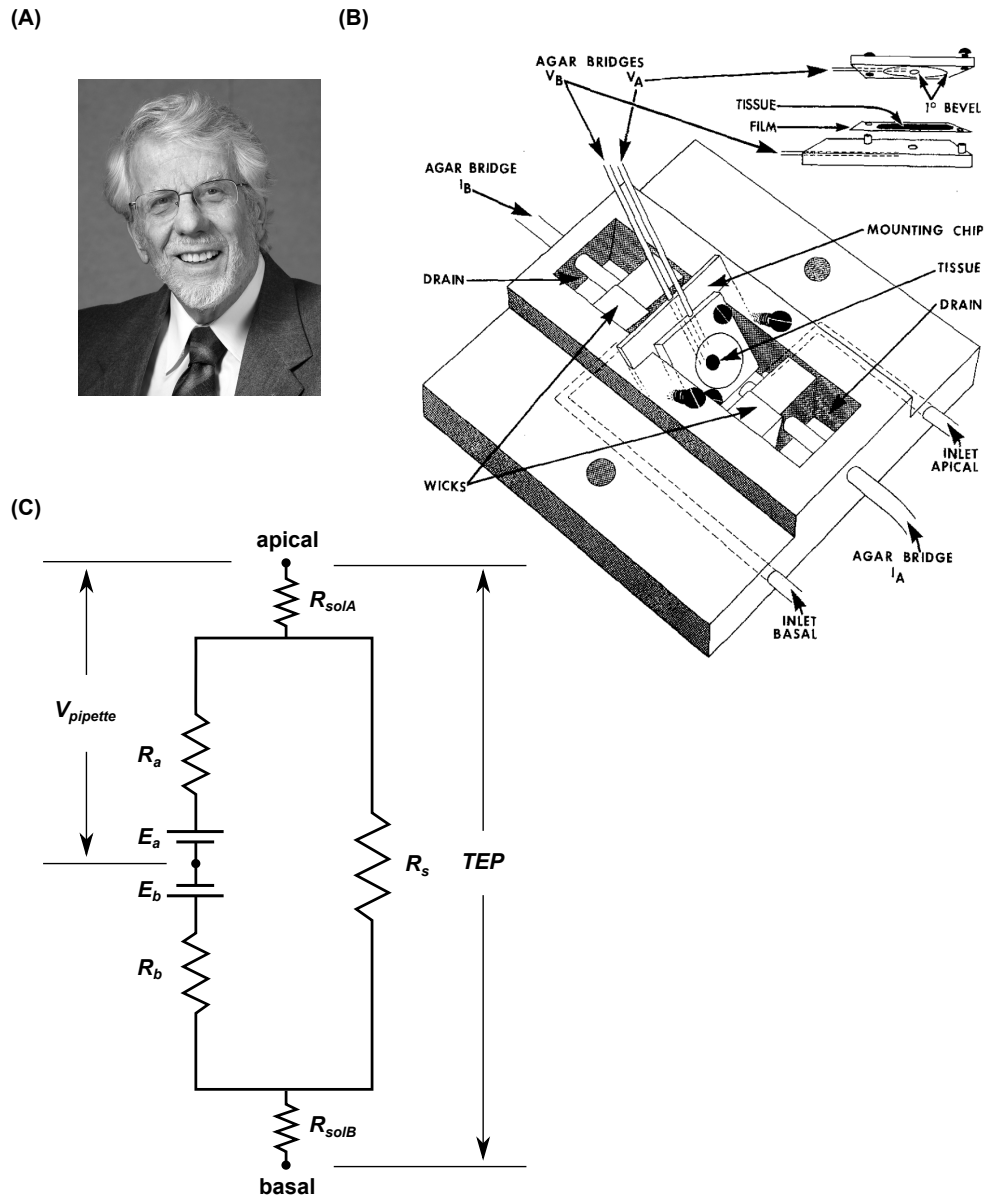


Figure 1.6: A modification to the Ussing chamber to study membrane-specific properties of epithelia. (A) Photograph of the inventor Sheldon Miller. (B) The modified chamber contains the same fundamental components of Ussing's chamber with a structural modification that allowed a pipette to access the apical membrane of the epithelia. (C) The equivalent circuit that is measured with Miller's chamber.  $V_{pipette}$  represents the voltage measured with the pipette.

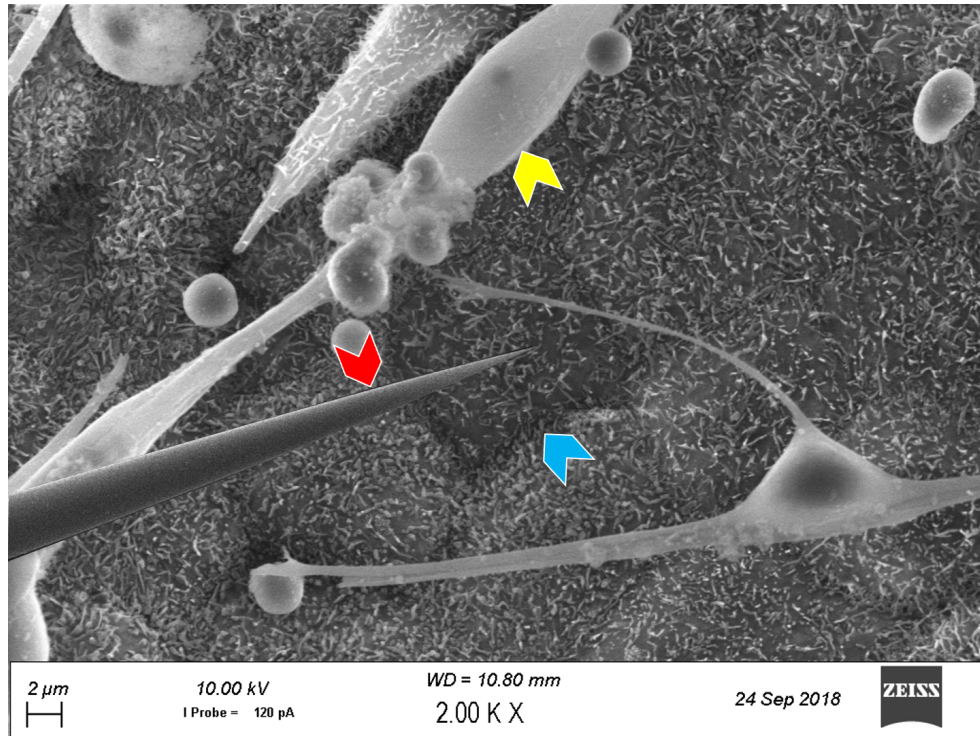


Figure 1.7: A scanning electron microscope (SEM) image of RPE with photoreceptors and intracellular pipette for scale. The red chevron indicates the pipette, the blue chevron indicates an epithelial tight junction (cell border), and the yellow chevron locates a photoreceptor outer segment. RPE are approximately  $10\ \mu\text{m}$  thick. The pipette must be inserted into the cytoplasm quickly to ensure that the pipette punctures the membrane rather than displacing the cell. If the solution perfusion and the electrode position are relatively stable, the membrane will seal around the perimeter of the pipette, causing electrical isolation from the apical bath due to the relatively high resistance of the seal.

The delicate positioning of this pipette into the cytoplasm of a cell traditionally requires mounting the pipette into a holder that is rigidly connected to a translating stage. When a button is pressed, the pipette rapidly descends towards the epithelia, and spontaneously stops movement when detecting a voltage decrease that surpasses a predetermined threshold, indicating successful pipette insertion. However, in some cases, no voltage drop is detected during descent (e.g., the pipette tip was clogged, or it penetrated the perimeter tight junctions rather than the cytoplasm). In these cases, the pipette will likely puncture a hole in the epithelial monolayer. If a hole is created, the entire sample needs to be discarded because it creates an electrical “short-circuit.” The resulting free exchange of ions

between baths can alter the measured electrical properties enough to contaminate the results of subsequent experiments. Therefore, experiments require a trained user to closely monitor an oscilloscope (that charts the real-time pipette potential) and determine when to halt the translation of the pipette and avoid tissue damage.

Visual guidance of the pipette under microscopy could ameliorate the pipette insertion issues with traditional, manual intracellular recordings, but visual guidance would significantly complicate the modified Üssing chamber setup due to a lack of space for a microscope lens – with sufficient magnification – and an opposing light source. Thus, the pipette insertion process is typically performed without conventional optical feedback techniques [17]. As a result, intracellular electrophysiology of epithelia is something of an art form, requiring great skill and years of training, and, thus, has been limited to isolated laboratory studies on carefully selected cells and drugs [7, 18, 19, 20, 21, 22, 23, 24, 25, 26, 27, 28, 29]. For intracellular electrophysiology of epithelia to become a broadly accepted technique for high-quality validation of cell-replacement therapies and drug screening, it must achieve higher yield and require less technical skill.

### **1.3 Induced pluripotent stem cells**

The discovery of iPSCs in 2006 by Takahashi and Yamanaka has revolutionized regenerative medicine and is spurring increased demand for high throughput and high-quality techniques for at- or in-line cell quality control (QC) assays [7, 30, 31]. In particular, autologous iPSC transplantation as a means of replacing damaged or dysfunctional tissue has garnered significant interest because it avoids both immune rejection and many of society's ethical issues with embryonic stem cells [32]. Methods for treating diseases such as AMD and CF using iPSC-derived epithelia have shown early promise. For example, recent work by Co-I Kapil Bharti has demonstrated functional recovery of damaged photoreceptors in a porcine model of AMD by transplanting iPSC-derived RPE into the eye [33]. For CF, Miller et al. have successfully engrafted human pluripotent stem cell (hPSC)-derived lung

epithelia in a murine lung injury model [34].

For iPSC therapies to be effective, these cells must be capable of replicating the physiology of native tissue. QC of iPSC-derived tissues is typically performed with imaging and staining, but these techniques often require cells to be in suspension, are generally time-consuming, need labeling, and can be destructive [35]. Electrophysiology is a critical QC metric for iPSC-derived epithelial tissues which are used to evaluate membrane polarity and cell function [7, 33]. However, there is an unmet need for a device that can non-destructively perform high-throughput and high-quality electrophysiological QC on iPSC-derived epithelia. The aim of this Ph.D. was to develop such a device.

## CHAPTER 2

### DEVELOP A ROBOT CAPABLE OF AUTOMATED INTRACELLULAR MEASUREMENT OF EPITHELIAL ELECTROPHYSIOLOGY

Portions of the results described in this chapter have been previously published in [36].

#### 2.1 Motivation

Anti-inflammatory abilities of epithelia are dependent on the induction of cell polarity and selective permeability across the monolayer. For example, within the healthy human eye, RPE are responsible for the transport of ions, metabolites, and fluid between the neural retina and the choriocapillaris [37, 11, 38]. The disruption of RPE structure or function is implicated in several forms of retinal degeneration. For instance, AMD, the most prevalent form of blindness in elderly people over 60, is caused by atrophy of the RPE [8, 10, 9, 11, 12, 13, 14]. Several commonly used drugs including anti-malaria drug (Chloroquine [39]), glaucoma drug (Latanoprost [40]), anti-allergy drug (Epinephrine), multiple sclerosis drugs (Corticosteroids and Fingolimod [41]), and anti-cancer drugs (MEK-inhibitors – Pimasertib, Trametinib, Binimetinib, Cobimetinib, and Selumetinib [42]) increase the chance of developing sight-threatening conditions such as macular edema and retinal detachment, perhaps by disrupting channel/transporter function in the RPE and inhibiting fluid transport.

No cure for macular degenerative diseases exist, yet promisingly, recent phase-I clinical trials using a monolayer of human embryonic stem cell (hESC)-derived RPE, transplanted in the sub retinal space (SRS), have demonstrated some signs of visual recovery in humans suffering from severe exudative (wet) and late-stage (dry) AMD [43, 11, 44, 14]. In addition, recent studies utilizing an iPSC-derived RPE patch, also transplanted in the SRS, have demonstrated anatomical and functional recovery of damaged photoreceptors in a pig

model with laser-induced RPE injury [33]. For therapeutic use, iPSC and hESC-derived RPE health and function must be verified using a variety of metrics such as: gene/protein expression, imaging, and electrophysiology of the cells in an intact monolayer [7, 33]. This latter metric, electrophysiology, is used to quantify epithelial responses to physiologically relevant stimuli.

For example, in the intact cat eye, it has been shown that the transition between light and dark environments causes a drop in potassium ( $K^+$ ) concentration in the SRS [45, 46]. This physiological condition has been simulated, *in vitro*, by artificially altering apical bath ion concentrations and observing the effects on RPE electrical responses [47, 48, 49, 50]. Similar *in vitro* intracellular electrophysiology assays are used to study ion permeability and disease mechanisms (e.g., CF and cigarette smoke) with epithelia such as tracheal, skin, mammary, respiratory, and kidney [24, 23, 25, 26, 27, 28, 51]. Consequently, *in vitro* electrophysiology assays are a powerful tool to study underlying epithelia channel distribution patterns that can be used to study cell physiology, disease processes, and drug toxicity [7].

*In vitro* epithelia electrophysiology measurements are conventionally performed in a modified Üssing chamber with separate apical and basal bath perfusion (Figure 1.6B) [47, 52, 4]. To record the intracellular potential ( $V_{pipette}$  in Figure 1.6C), a sharp glass pipette, approximately 100 nm to 200 nm in diameter at the tip (validated with SEM as seen in Figure 1.7), must be delicately positioned and inserted, blindly, into the cell's cytoplasm, termed "break-in" [18].

In conventional, manual experiments, the pipette is mounted in a pipette holder that is rigidly connected to a microelectrode amplifier that is attached to the translating stage of a piezoelectric motor. To initiate pipette descent towards the tissue, a user must continuously press a button on a custom-made instrument. When the button is pressed, the pipette rapidly descends towards the cell monolayer, and spontaneously stops movement when detecting a voltage decrease that exceeds a predetermined threshold. However, in some cases, no

voltage drop is detected during descent (e.g., the pipette tip was clogged, or it penetrated the cell tight junction rather than the cytoplasm). In these cases, the pipette will likely puncture a hole in the RPE monolayer. If a hole is created, the entire tissue needs to be discarded because it creates an electrical ‘short-circuit’ across the monolayer; allowing for the free exchange of ions between the apical and basal baths. The free exchange of ions between baths could alter the measured electrical properties enough to contaminate the results of subsequent experiments. Therefore, manual experiments require a trained user to closely monitor an oscilloscope and determine when to halt the translation of the pipette and avoid tissue damage.

Visual guidance of the pipette under microscopy could ameliorate the issues with manual intracellular recordings and would enable stable and high-quality recordings, but visual guidance would significantly complicate the modified Üssing chamber setup due to a lack of space for a microscope lens – with sufficient magnification – and an opposing light source. Thus, the pipette insertion process must be performed without conventional optical feedback techniques [17]. As a result, intracellular electrophysiology of epithelia is something of an art form, requiring great skill and years of training, and thus has been limited to isolated laboratory studies on carefully selected cells and drugs [22, 24, 23, 25, 20, 21, 19, 18, 7, 29, 26, 27, 28]. For *in vitro* intracellular electrophysiology of epithelia to become a broadly accepted technique for high-quality validation of cell-replacement therapies and drug screening, it must achieve higher yield and require less technical skill.

## **2.2 Methods**

### 2.2.1 Primary hFRPE cell culture

Previously published protocols for culturing human fetal (hf) RPE were followed [18]. Briefly, hFRPE were isolated from fetal eyes at 16-18 weeks gestation (Advanced Bioscience Resources, Alameda, CA) and cultured in Primaria tissue culture flasks (BD Biosciences, Franklin Lakes, NJ). The culture medium was changed every 3 days and cells

were subcultured with a trypsin-EDTA treatment and seeded on semipermeable Transwells (Corning Costar). Only cells of passage 1 were used for all studies. The experiments were usually performed after 6-8 weeks of culture or after the cells formed a completely confluent monolayer. Confluence was determined by observing uniform, pigmented coverage of the Transwell and when the tissue  $R_t$  was greater than  $300 \Omega \text{ cm}$  [7]. All cells were maintained on Transwells at  $37^\circ \text{C}$  in a  $5\% \text{ CO}_2$  humidified incubator with medium change 3 times per week.

### 2.2.2 Generation, differentiation, and characterization of human iPSC-RPE

Cells, isolated from donor tissue, were reprogrammed using Sendai virus-mediated delivery (CytoTune, Life Technologies) of the four Yamanaka factors (c-MYC, KLF4, OCT4, and SOX2), following the manufacturer's recommendations. Three-germ layer differentiation of iPSC lines were performed using a published protocol [53]. Antibodies against NESTIN, TUJ1, SOX17, AFP, BRACHYURY, and SMA were used for the characterization of cells of all three germ layers. Karyotyping was performed at Cell Line Genetics (Madison, WI). iPSCs were differentiated into RPE using a previously published protocol [54] with modifications [33]. Differentiated RPE cells were characterized with a transmission electron microscope (TEM) for morphology, gene expression, and immunostaining for RPE specific markers. All human work was done under institutional review board-approved protocol 11-E1-0245.

### 2.2.3 Pipette fabrication

Sharp microelectrode pipettes were pulled from 1 mm outer diameter, 0.5 mm inner diameter, fire-polished borosilicate glass with a filament (Sutter Instruments) on a P-97 puller with a 2.5x2.5 mm box filament (Sutter Instrument). The pipettes were pulled in a single cycle of the puller. The resulting pipette had a tip size approximately 100 nm to 200 nm in diameter (validated with SEM) and resistance between  $120 \text{ M}\Omega$  to  $250 \text{ M}\Omega$ .

#### 2.2.4 Cell culture medium and physiology solution compositions

Methods were originally developed by Maminishkis et al. [18], and are briefly summarized here. MEM- $\alpha$  modified medium (Sigma-Aldrich) was used to formulate 5% and 15% serum-containing media for culturing RPE cells. The solution contained fetal bovine serum (Atlanta Biologicals), N1 supplement (Sigma-Aldrich) 1:100 mL/mL, glutamine-penicillin-streptomycin (Sigma-Aldrich) 1:100 mL/mL, and nonessential amino acid solution (Sigma-Aldrich) 1:100 mL/mL.

The bulk Ringer solution, used in electrophysiology experiments, consisted of (in mM) 5 KCl, 116.5 NaCl, 23 NaHCO<sub>3</sub>, 0.5 MgCl<sub>2</sub>, 1.8 CaCl<sub>2</sub>, 2 taurine, 5 glucose, and 10 sucrose. The Ringer solution was bubbled with 5% CO<sub>2</sub>, 10% O<sub>2</sub>, and 85% N<sub>2</sub> to bring the Ringer solution to a pH near 7.4 and an osmolarity around 295 $\pm$ 5 mOsM. When experiments were performed, 100  $\mu$ M ATP was added to the bulk Ringer solution, or 1 mM K<sup>+</sup> modified Ringer's solution was prepared using the same bulk recipe except for the isosmotic substitution of NaCl for decreased KCl.

#### 2.2.5 Tissue preparation

Prior to an experiment, a 7 mm circular section of the RPE culture was cut out with a punch (Acuderm inc.), then placed on a supporting nylon mesh to increase the monolayer stiffness, reduce the magnitude of oscillation due to fluctuations and bubbles of the perfusion solution, and maximize measured tissue resistance. The RPE was placed – apical side up – between the two halves of a modified Üssing chamber [4]. The two halves of the modified Üssing chamber were sealed to create physical and electrochemical separation of RPE apical and basolateral membranes. To ensure this seal, a thin layer of silicone vacuum grease (Beckman Coulter), was applied, by hand, to the inner side of the chamber halves. The chamber is depicted in Figure 2.1.

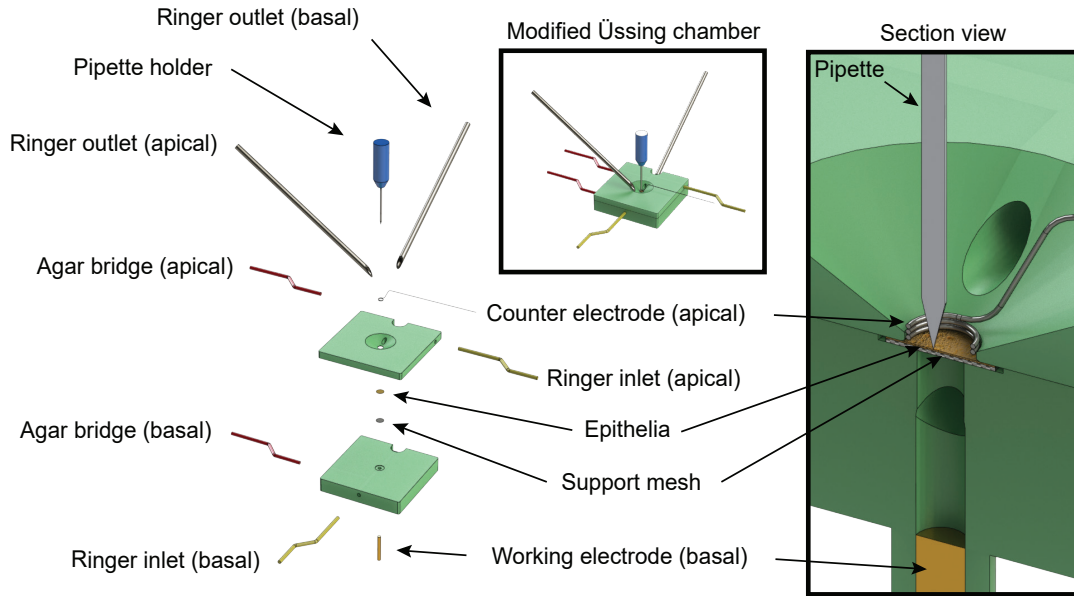


Figure 2.1: Exploded view of the chamber used to automate the study of membrane-specific epithelia electrophysiology. Red tubing indicates the location of the agar bridge connections to the Ringer solution. The yellow tubing indicates the location of the Ringer inlets. The silver tubing indicates the location of the vacuum lines [36].

Figure 2.1 shows how the pipette accesses the RPE from the apical side while it is flanked by a pair of agar bridges (connected to Calomel electrodes), as well as Ag|AgCl working and counter electrodes placed in the basal and apical halves, respectively. Perfusion inlets deliver the apical and basal Ringer solution to the RPE through ports machined in the modified Ussing chamber. Perfusion outlets remove Ringer solution through vacuum lines positioned so that fluid height, and, consequently, fluid pressure remains constant across the RPE membrane. The modified Ussing chamber was rotated approximately 30 degrees from horizontal.

### 2.2.6 Electrophysiology experiments

Some of the hardware used for RPE electrophysiology was based on the previously reported apparatus for automated patch-clamp electrophysiology [55]. A Multiclamp 700B (Molecular Devices) amplifier was utilized to amplify measured membrane potentials. Signals were acquired with a NI USB-6211 (National Instruments) and processed in LabView

2016 at 50 Hz (National Instruments). Break-in protocols were optimized using a combination of a 3-axis, MP-285 micromanipulator (Sutter Instrument) with a PT1-Z8 Motorized Translation Stage (Thorlabs), and 1 mm pipette holder (Molecular Devices) were used to constrain and translate the pipette. The pipette was back-filled with 150 mM KCl solution. In later experiments, it was found that stability and backlash of the thread-based PT1-Z8 were unsuitable for long term experiments, resulting in lost recordings due to small - yet significant (estimated  $\pm 1 \mu\text{m}$ ) - oscillations and significant backlash (up to  $8 \mu\text{m}$ ) causing poor membrane sealing around the exterior of the pipette. Thus, the linear stage was replaced with a N-565.260 piezoelectric motor connected with an E-861.1A1 single-axis controller box (Physik Instrumente) due to its 0.5 nm positional resolution and relatively negligible backlash.

Calomel electrodes, in series with agar bridges, were connected to the apical and basal Ringer solution baths (see Figure 2.1) to measure the voltage across the RPE monolayer. The voltage difference across the RPE monolayer measured with these bridges is equal to the TEP shown in Figure 1.6C.  $R_t$ , which includes 3 parallel resistors (cellular resistance, resistance between adjoining cells at tight-junctions, and the resistance between the tissue and chamber walls), was determined by sending one period of a symmetrical square wave ( $\Delta I_{app} = 1 \mu\text{A}$ , period = 3 s) every 40 s, measuring the corresponding change in TEP ( $\Delta TEP$ ), and inserting these values into Ohm's law:

$$R_t = \frac{\Delta TEP}{\Delta I_{app}} \quad (2.1)$$

The pipette, once inserted into the cytoplasm of a single RPE, measures the voltage potential between the pipette and the apical reference electrode (see Figure 1.6C); referred to as the apical membrane potential ( $V_a$ ). The basal membrane potential ( $V_b$ ) was calculated by rearranging the following equation:

$$TEP = V_b - V_a \quad (2.2)$$

Continuous perfusion across both the apical and basal side of the RPE must be electrically isolated from the source to the waste collection flask to prevent an electrical short circuit. Perfusion was gravity-driven and the flow rate was adjusted with a threaded tube clamp to be approximately 4.5 mL/min. Bubbles were reduced in the modified Üssing chamber by coating the chamber surface with Sigmacote hydrophobic solution (Sigma-Aldrich), and by keeping the Ringer solution temperature along the perfusion line approximately 37 °C with a custom-made water jacket around the Ringer inlets. Ringer solution was removed, after crossing the RPE tissue, with a vacuum line and deposited in one of two 1 L vacuum flasks; one flask for the apical solution and one flask for the basal solution. Solution temperature inside the chamber was typically between 35.5 °C to 36.5 °C.

Once the pipette was successfully inserted into a cell and approximately 5 min had elapsed to allow the system to reach steady-state, the apical Ringer solution was replaced with a solution containing a different salt composition or pharmacological agent to induce cell physiological changes. Specifically, two unique, physiologically relevant solutions were used to assess RPE function: (1) a Ringer solution, identical to the original recipe, except that the potassium ( $K^+$ ) concentration was changed from 5 mM to 1 mM and (2) a Ringer solution containing 100  $\mu$ M ATP. These solutions were perfused continually until the TEP began to reach a new equilibrium. Once the new equilibrium was reached, the original Ringer solution replaced the modified solution until it returned to baseline.

### 2.2.7 Pipette position algorithm

To initiate a recording, five discrete stages of pipette positioning were developed that compose the pipette position algorithm (see Figure 2.2). In the first stage, called “Approach,”

pipettes installed in the robot were localized directly above the tissue and lowered until the surface of the apical solution was detected. The pipette detected the surface of the solution by monitoring pipette tip resistance at 50 Hz. When the tip resistance was less than  $1\text{ G}\Omega$ , the pipette was deemed to be in the solution.

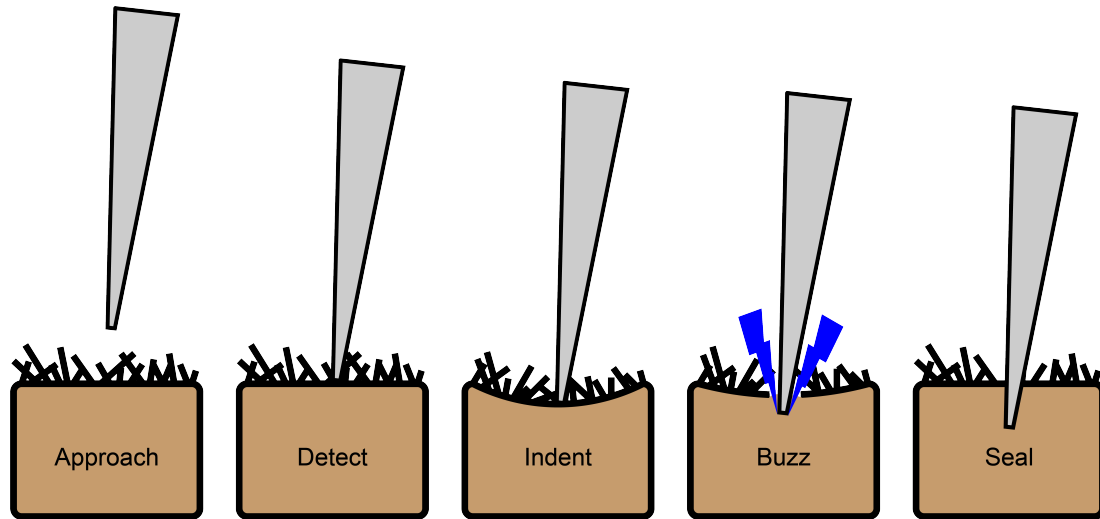


Figure 2.2: The algorithm used to break into RPE (from left to right). (1) Pipette (grey) “Approach” at a constant velocity while continuously monitoring tip resistance. (2) When the pipette tip resistance increase was detected, the pipette descent was paused, and the head stage was switched to current-clamp mode (do not measure resistance anymore). (3) If the pipette does not spontaneously break through the membrane (brown), rapidly descend the pipette at maximum velocity to “indent” the membrane. (4) While indenting the membrane, send a brief “buzz” command to the head stage. (5) Check the resultant change in measured tip potential and see if the membrane “seals” around the pipette [36].

Before proceeding to the detection stage of the five-stage algorithm (Figure 2.2), the pipette resistance was verified to be greater than  $100\text{ M}\Omega$ . If the resistance was below this target, the pipette was likely broken during installation and was discarded; thus, the procedure should be restarted with a new pipette. If the pipette was above the resistance target, it approached the RPE apical membrane at  $15\text{ }\mu\text{m/s}$  while resistance was measured continuously. The pipette resistance was measured using a  $1.1\text{ nA}$ ,  $50\text{ Hz}$  square wave and measuring the resultant voltage amplitude. These values were used in Ohm’s law ( $V = IR$ ) to calculate the pipette tip resistance. When the resistance difference over a 1-second rolling window exceeded  $4\text{ M}\Omega$ , the RPE apical membrane was likely “detected,”

and the robot was paused for 3 s.

If the pipette spontaneously broke into the cell membrane during the 3 s pause and, consequently, the measured potential decreased by more than 1 mV, the remaining break-in procedure was skipped. However, if the measured potential change was less than 1 mV, a 6  $\mu\text{m}$  pipette descent (60% of average cell thickness) was initiated at maximum velocity (peak velocity during descent was approximately 15  $\mu\text{m}/\text{s}$  for the PT1-Z8 stage) to “indent” the local apical membrane (see Figure 2.2). This decent depth was optimized by measuring the yield for depths from 0  $\mu\text{m}$  to 10  $\mu\text{m}$  in 1  $\mu\text{m}$  steps. The “buzz” command, available in current-clamp mode while using the Multiclamp 700B software (Molecular Devices), was initiated after the pipette had advanced 83% (or 5  $\mu\text{m}$ ) of the 6  $\mu\text{m}$  indent depth. Like decent depth, buzz depth was optimized by varying the location where the buzz was initiated relative to the target indent depth. Specifically, a buzz depth of 0  $\mu\text{m}$  would indicate that the buzz was initiated when the pipette reached the indent depth, and a buzz depth of -1  $\mu\text{m}$  would indicate that the buzz was initiated when the pipette was 1  $\mu\text{m}$  above the desired indent depth. Additionally, the pipette was not paused to initiate the buzz during the indent. To minimize potential deleterious effects caused by calcium influx during electroporation, the buzz duration was set to 100  $\mu\text{s}$  because it was the shortest duration that was repeatably executed by the Multiclamp 700B software.

After electroporating the RPE membrane, the break-in was considered successful if the measured potential decreased by more than 30 mV from the baseline for more than 1 s; indicating electrical access to the interior of the cell. Additionally, a recording was considered stable if the measured basal membrane potential was approximately  $-51 \pm 7$  mV – the typical basal membrane potential for hRPE – for more than 5 min [20, 21, 18, 7, 29]. The threshold for a stable recording was set at 5 min because that is the minimum duration for a complete evoked response from RPE [52], and, cell loss (after the 5 min threshold) can be caused by multiple other factors not necessarily related to the cell impalement algorithm. For example, unstable or turbulent perfusion can cause small perturbations of the

tissue relative to the intracellular pipette, or cell swelling and shrinking in response to the introduction of new drugs could break the tight seal at the pipette-membrane interface. In both cases, cell loss would not be related to the insertion technique.

## 2.3 Results and discussion

### 2.3.1 Break-in algorithm

The break-in process was systematically optimized by separating into five stages (Figure 2.2). In this algorithm, the buzz event occurs prior to the full depth of indentation and triggers a potential drop, due to break-in, virtually instantaneously. The additional pipette advancement after break-in seems to enhance seal yield. This observation was tested by attempting random combinations of both buzz and indent depths and observing break-in yields. Break-in probability was measured at 1  $\mu\text{m}$  depths, as shown in Figure 2.3.

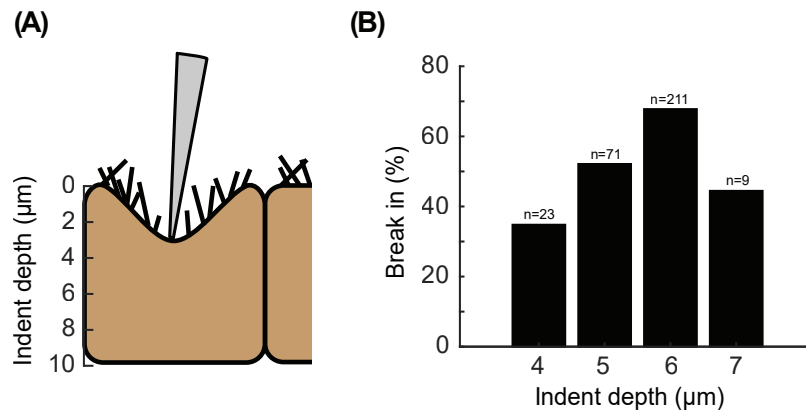


Figure 2.3: Indent depth break in probability. (A) Graphical representation of the pipette and cell configuration during the indent step of the break-in algorithm. (B) The probability of a successful break-in as a function of pipette indent depth [36].

Indent depths less than 4  $\mu\text{m}$  did not generate enough force on the membrane to consistently break into the cell membrane. In addition, indent depths greater than 6  $\mu\text{m}$  occasionally broke the pipette tip. This is likely because RPE monolayers are, on average, 10  $\mu\text{m}$  thick at the center with a slight decrease near the extremities, and, if the pipette makes first contact near the cell junctions, could descend far enough to collide with the Transwell

membrane [56]. Puncturing the Transwell membrane is catastrophic for an electrophysiology experiment because it creates a hole that electrically connects the apical and basal Ringer solutions; thus, requiring complete replacement of the tissue. Therefore, from Figure 2.3 it was concluded that the optimum descent depth was in the range of 4  $\mu\text{m}$  to 6  $\mu\text{m}$  for RPE.

A chi-squared test verified that break-in chance was a function of indent depth ( $p = 0.003$ ). Regardless of buzz depth (less than or equal to indent depth), there appeared to be a maximum break in probability of 68% ( $n=211$  trials) at an indent depth of 6  $\mu\text{m}$  (60% of average RPE thickness).

The effect of relative buzz depth was evaluated as shown in Figure 2.4. Regardless of indent depth, a buzz depth of 1  $\mu\text{m}$  before the target indent depth,  $x$ , resulted in a maximum break in probability of 69% ( $n=143$ ). Initiating a buzz before the target descent depth is not common practice, and, surprisingly, seemed to result in higher yield than at full depth. The significance was verified with a chi-square test ( $p = 0.033$ ) with the null hypothesis that relative depth and break in chance are not related.

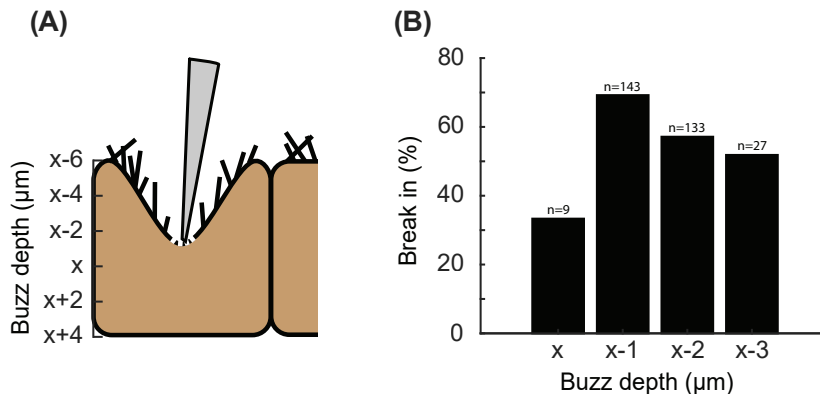


Figure 2.4: Buzz depth break in probability. (A) graphical representation of the pipette approximately 1  $\mu\text{m}$  above a target indent depth,  $x$ . (B) the probability of a successful break-in as a function of relative buzz signal depth only [36].

I theorize at least two possible explanations for the observed results: (1) the electroporated region on the cell membrane, generated during the buzz, is optimally resealed by descending the tapered pipette tip an additional 1  $\mu\text{m}$ , or (2) the pipette could be dragging

the membrane for 1  $\mu\text{m}$  in a way that helps secure the membrane to the pipette. In either scenario, the membrane seal would be a function of the contact surface area between the cell membrane and pipette.

Other experimental parameters, outside of the control of the algorithm, were adjusted to see what effects, if any, they had on this yield. Specifically, the thickness of the supporting mesh, the velocity of the motors during break-in, and the buzz duration were adjusted. Consequently, it was noted that the thickness of the supporting nylon mesh, placed below the epithelia and clamped between the two halves of the  $\ddot{U}$ ssing chamber, had a significant effect on break-in and recording yield. This phenomenon could be explained by the specific construction of the modified  $\ddot{U}$ ssing chamber. This chamber was designed to mount a range of tissues and barrier-type cells that have a correspondingly large range of possible thickness. In order to mount thicker tissues, the chamber must have a large gap between the two halves. To fill the remaining gap when mounting thinner tissues – and ensure sufficient electrical and fluid clamping around the tissue – a nylon supporting mesh is used. Consequently, the thickness of the nylon mesh is determined by maximizing the measured  $R_t$  for the cell line because this is an indication of high clamping resistance at the interface between the cells and the  $\ddot{U}$ ssing chamber. If the nylon mesh was not sufficiently thick, the tissue could drift relative to the pipette position, negatively impacting measured yields. After optimizing the mesh thickness, indent depth, and relative buzz depth, with the PT1-Z8 linear stage motor, the break-in and stable recording yield for a 6  $\mu\text{m}$  indent depth and a 5  $\mu\text{m}$  buzz depth were 74% and 22% (n=120), respectively. Furthermore, the stable recording yield was vastly improved after transitioning to the N-565.260 piezomotor and pulling even sharper pipettes (i.e., resistance greater than 250  $\text{M}\Omega$ ) to 62% (n=26).

### 2.3.2 Validation of cell health

To ensure that the new, automated insertion technique did not significantly alter the health of the epithelia, the electrical properties can be compared to data presented in the literature

(Table 2.1).

Table 2.1: Stable human fetal-derived retinal pigment epithelia (hFRPE) electrical properties reported in the literature (manual) compared with values obtained with the automated method. The properties compared across literature include the basal membrane voltage ( $V_b$ ), the transepithelial potential ( $TEP$ ), and the total tissue resistance ( $R_t$ ). *Note:* 26 stable attempts with our automated method were recorded. However, the exact magnitude of the first 3 stable recordings was not documented. Thus, we report average responses for 23/26 stable recordings using the automated method. All data are shown as mean  $\pm$  standard deviation. \*n=35 for TEP and  $R_t$  recordings [36].

Method	n	$V_b$	$TEP$ (mV)	$R_t$ ( $\Omega.cm^2$ )
[20]	9	$-46 \pm 6$	$3.2 \pm 1.5$	$227 \pm 90$
[21]	5	$-58 \pm 14$	$1.7 \pm 0.3$	$326 \pm 92$
[18]	12	$-50 \pm 4$	$2.6 \pm 0.8^*$	$501 \pm 138^*$
[7]	9	$-52 \pm 2$	$7.3 \pm 2.1$	$647 \pm 120$
Automated	23	$-53 \pm 3$	$1.2 \pm 0.9$	$544 \pm 79$

Statistical analysis of hFRPE data presented in literature reveals a lack of agreement on what constitutes acceptable TEP and  $R_t$  ( $p < 0.001$  for both cases). The largest outlier appears to be the data presented by [7]. However, the variance in TEP and  $R_t$  can be explained by factors unrelated to tissue health or quality. For example, TEP is directly affected by the relative pressures of the apical and basal fluid which are set, by hand, prior to each experiment. In addition, the quality of the clamping force separating the apical and basal solutions is usually optimized before the experiment by maximizing the measured  $R_t$  for the desired cell line; implying that clamping force and quality also plays a role in reported  $R_t$ . Therefore, it seems that tissue TEP and  $R_t$  would be a poor indicator of the effect that the automated insertion process has on tissue health.

In contrast to TEP and  $R_t$ ,  $V_b$  is a cell-specific parameter and should not be drastically affected by experimental settings such as the chamber clamping force and the relative fluid pressures, and it should be more directly related to the balance of ions both inside and outside the cell as governed by the Goldman equation presented in Chapter 1. If the electroporation process during the insertion of the electrode damages the cell, ions would spontaneously transfer in and out of the cell; drastically altering the measured membrane

potential [57]. Therefore,  $V_b$  from RPE in literature – submerged in similar extracellular Ringer’s solutions – can be averaged together to give an expected resting membrane potential ( $-51 \pm 7$  mV). A two-tailed t-test comparing the distributions of  $V_b$  reported in the literature and the  $V_b$  measured with the automated method reveals that they are not statistically different ( $p > 0.2$ ), and it can be concluded that the automated pipette insertion process has no statistically detectable deleterious effect on cell health.

Furthermore, the results of a complete electrophysiology experiment performed using both the optimized algorithmic methods and the original, manual method give insight into channel function and distribution of RPE (Figure 2.5).

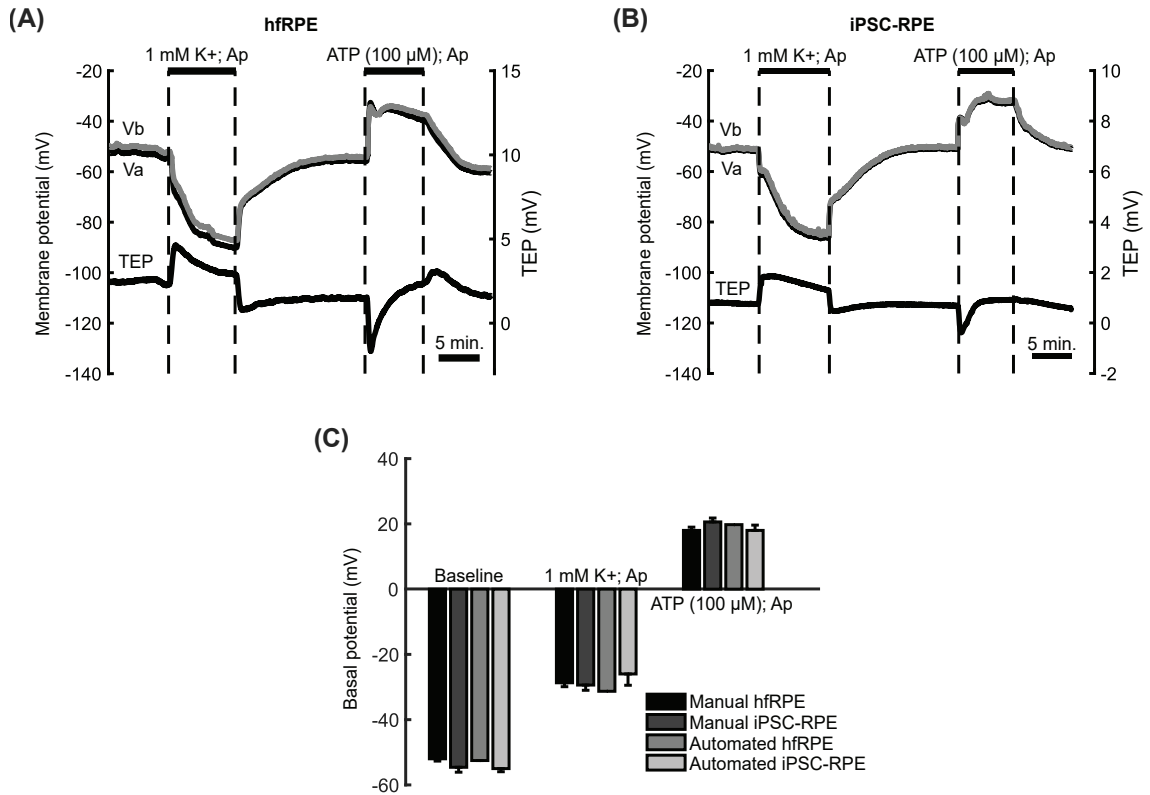


Figure 2.5: hfRPE and iPSC-RPE evoked responses compared with manual technique. (A-B) Representative electrical responses to apical application of low  $K^+$  and ATP in cultured hfRPE (A) or iPSC-RPE (B) recorded using the automated method with optimal indent depth of  $6\ \mu\text{m}$  and buzz depth of  $5\ \mu\text{m}$ . For each graph, the top traces show the changes of apical and basal membrane potential ( $V_a$ ,  $V_b$ ), The bottom trace shows the changes of TEP.  $V_a$ ,  $V_b$ , and TEP were measured simultaneously in each experiment. The black horizontal bars indicate the time during which  $1\ \text{mM}\ K^+$  or  $100\ \mu\text{M}\ \text{ATP}$  were perfused to the apical bath. Time scale bar: 5 minutes. (C) Summary data for the resting and evoked  $V_b$  changes in response to low  $K^+$  and ATP application using the manual or automated method. The bar chart shows the mean  $\pm$  SE of the evoked electrical responses measured using the conventional, manual technique during a previous study (hfRPE,  $n=9$  and iPSC-RPE,  $n=15$  [7]) and the new, automated technique (hfRPE,  $n=1$  and iPSC-RPE,  $n=10$ ) [36].

Intracellular recordings of RPE membrane potential in response to apical low  $K^+$  or ATP provide important functional assessments to authenticate RPE physiology. Altering the apical bath  $K^+$  concentration from  $5\ \text{mM}$  to  $1\ \text{mM}$  mimics the extracellular  $K^+$  concentration drop that occurs *in vivo* in the SRS of the eye, which is initiated by changes in photoreceptor activity following the transition from dark-to-light [58, 38]. ATP is a proposed light peak (LP) substrate; ATP acts on apical membrane purinergic P2Y2 receptors,

causing subsequent downstream signaling that leads to channel activity changes on RPE apical and basal membrane; thus, driving fluid transport across the RPE monolayer [59]. These two physiological stimuli are critical indicators of the health and integrity of the RPE monolayer.

With the automated method, in both hfrPE and iPSC-RPE, the potassium concentration drop in the apical bath caused a 30 mV hyperpolarization of the RPE apical and basal membranes and a 1 mV to 2 mV increase in the TEP (Figure 2.5 A-B). In contrast, apical ATP application on hfrPE and iPSC-RPE induced about a 20 mV membrane depolarization in both membranes (Figure 2.5 A-B). These responses have been observed previously, using the manual method, in primary cultured hfrPE and various iPSC-RPE; derived from different tissue sources and donors [7]. In particular, the iPSC-RPE evoked response data (Figure 2.5C) shows no distinguishable difference between the automated (n=10) and manual (n=15) methods for each experimental condition ( $-54.6 \pm 1.5$  mV vs.  $-55.0 \pm 1.0$  mV for baseline,  $-29.4 \pm 1.6$  mV vs.  $-26.0 \pm 3.5$  mV for low  $K^+$  response,  $20.6 \pm 1.2$  mV vs.  $18.0 \pm 1.6$  mV for ATP response; two-tailed t-test,  $p=0.8$ ,  $p=0.3$ ,  $p=0.2$ , respectively) [7].

## 2.4 Conclusions

This chapter presents an optimized technique for high-yield, automated intracellular electrophysiology of epithelial cultures; such as hfrPE. This technique improved break-in yield from 44% to 74% and stable recording yield from 17% to 62% using conventional techniques and a five-stage algorithm, respectively. The algorithm was developed and optimized systematically, yielding optimal manipulator speeds, buzz duration, as well as buzz and indent depths. The baseline membrane potential and measured responses of RPE to low  $K^+$  and ATP were indistinguishable from those measured with the manual technique which indicates that the methodology utilized by the algorithm did not alter the physiology of the epithelia. Surprisingly, advancing the pipette 60% through the RPE (6  $\mu\text{m}$ ), yet buzzing at 83% of this depth (5  $\mu\text{m}$ ) maximized yield. This technique overturns common practice

in the field and improves yield at a much lower operator skill level; enabling more labs to explore the physiology, drug toxicity, and disease processes of epithelia. Future work could explore recent advancements in automated electrophysiology to further improve yield using techniques such as pipette swapping or pipette cleaning [60, 61].

**CHAPTER 3**

**DEVELOP A MATHEMATICAL MODEL TO MEASURE THE PREVIOUSLY  
UNOBSERVABLE APICAL AND BASOLATERAL MEMBRANE PROPERTIES  
USING EXTRACELLULAR ELECTROCHEMICAL IMPEDANCE  
SPECTROSCOPY**

**3.1 Motivation**

Electrochemical impedance spectroscopy (EIS) is a powerful measurement technique that leverages the unique properties of capacitors and resistors to extract the frequency-dependent behavior of complex circuits. At present, few labs have attempted to capitalize on the usefulness of this technique, and fewer still have attempted to merge it with intracellular data. Previous attempts to measure membrane-specific properties of epithelia involved (1) making assumptions about cell function, (2) often required an extra measurement prior to each experiment (e.g., measuring paracellular flux to estimate the shunt resistance), and (3) were highly sensitive to measurement bias due to pipette clogging or poor membrane-to-pipette seals [62, 35, 63, 64, 65, 66, 67, 68, 69, 70, 71, 72, 73, 74]. The ability to directly monitor individual membrane properties would vastly reduce experimental complexity by eliminating the need to perform follow-up confirmation experiments - discussed in the previous chapter - to validate the observed changes in the voltage divider ratio ( $a$ ) and total tissue resistance ( $R_t$ ). Thus, this chapter outlines and validates a mathematical model that can be used to solve for individual membrane properties of epithelia - without requisite assumptions about cell function - by merging intracellular recordings with EIS.

## 3.2 Methods

### 3.2.1 Intracellular electrophysiology equations

For reference, the most complete circuit that can be studied when performing an intracellular recording of epithelia is presented in Figure 1.4B.

#### *Equations for analysis assuming very low measurement frequencies*

Despite utilizing an intracellular pipette in the modified Üssing chamber of Figure 1.6B or Figure 2.1, the apical and basal membrane resistances ( $R_a$  and  $R_b$ , respectively) cannot be directly measured, since it is not possible to simultaneously monitor the magnitude of current and voltage flowing through the apical and basolateral membranes with a single pipette. However, as was shown in Figure 1.6C, if the pipette is used to monitor the intracellular voltage with respect to the apical bath ( $V_a$ ), the external sense and reference electrodes monitor *TEP* ( $V_a$  and  $V_b$  agar bridges in Figure 1.6B), and the working and counter electrodes control the net transepithelial current  $I_{app}$  ( $I_a$  and  $I_b$  agar bridges in Figure 1.6B), the instantaneous value of the basolateral voltage ( $V_b$ ) can be calculated by rearranging the TEP equation ( $TEP = V_b - V_a$ ). Therefore, the magnitude of current flowing through  $R_a$  must be equal to the current in  $R_b$  from Kirchoff's Current Law, and the following resistance ratio can be calculated as a function of membrane voltages:

$$a = \frac{R_a + R_{solA}}{R_b + R_{solB}} = \frac{V_a}{V_b} \quad (3.1)$$

where  $a$  is frequently referred to as the voltage divider ratio.

Further analysis of Figure 1.4B shows the apical and basolateral membranes of the epithelia contain an equivalent EMF ( $E_a$  or  $E_b$ ) in series with a resistor,  $R_a$  or  $R_b$ , respectively. The paracellular pathway (comprised of the parallel combination of tight junctions

and mechanical seal between the epithelia and chamber walls) is represented as a shunt resistor,  $R_s$ . This shunt resistance pathway, in combination with active transport processes in epithelia generates a short circuit current ( $I_s$ ) that flows in a loop around the circuit. Thus, the application of Kirchoff's voltage law to Figure 1.4B yields the following differential equations for  $V_a$  and  $V_b$ :

$$V_a + \frac{C_a R_a dV_a}{dt} = R_a(I_{app} + I_s) - E_a + I_{app} R_{solA} \quad (3.2)$$

$$V_b + \frac{C_b R_b dV_b}{dt} = -E_b - R_b(I_{app} + I_s) - I_{app} R_{solB} \quad (3.3)$$

where

$$I_s = \frac{V_b - V_a}{R_s} \quad (3.4)$$

If the system is allowed to reach steady-state ( $dV/dt = 0$ ), the previous differential equations can be simplified to:

$$V_a = R_a(I_{app} + I_s) - E_a + I_{app} R_{solA} \quad (3.5)$$

$$V_b = -E_b - R_b(I_{app} + I_s) - I_{app} R_{solB} \quad (3.6)$$

Furthermore, if no current is applied by the external hardware ( $I_{app} = 0$ ), then:

$$V_a = I_s R_a - E_a \quad (3.7)$$

$$V_b = -E_b - I_s R_b \quad (3.8)$$

When the current flowing through the circuit is allowed to reach steady state, then the current that flows through the capacitors is necessarily 0. Thus, the circuit for intracellular electrophysiology can be reduced to the form shown in Figure 1.6C. For this circuit, the total tissue resistance ( $R_t$ ) can be calculated using conventional rules for combining resistors in parallel as follows:

$$R_t = R_{\text{solA}} + R_{\text{solB}} + \frac{R_s(R_a + R_b)}{R_s + R_a + R_b} \quad (3.9)$$

Electrophysiologists use the voltage divider ratio ( $a$ ) and the total tissue resistance ( $R_t$ ) to make *assumptions* about which membranes are responding to a stimulus. For example, if a concomitant decrease in  $a$  and increase in  $R_t$  is recorded, then it is most likely that  $R_b$  increased. However, it is also possible that  $R_b$  was constant and  $R_a$  decreased if  $R_s$  increased sufficiently to obfuscate the results in the measurement of  $R_t$ . Therefore, to conclude that the dominant contributor to the observed change in  $a$  and  $R_t$  was  $R_b$ , the experimenter must perform a follow-up test that targets the proposed mechanisms in the basolateral membrane to inhibit the changes. If the changes can be blocked with a drug known to target the proposed mechanisms on the basolateral membrane, only then is it safe to conclude that the observed changes in  $a$  and  $R_t$  are due to  $R_b$ .

### *Equations for analysis at any frequency*

To analyze a circuit with capacitors, it is useful to model all circuit elements using the formal impedances ( $Z$ ) that are comprised of a real and imaginary component. These impedance terms consider the complex behavior of circuit elements in response to a general AC input signal; often represented as a sinusoid ( $A \sin wt + \phi$ ). This more general formulation of input signal is a function of amplitude  $A$ , frequency  $w$  (in rad/s), time  $t$ , and phase shift  $\phi$ . For the simple case of a resistor, the complex impedance is directly proportional to the magnitude of the real circuit resistance ( $R$ ) such that:

$$Z_R(w) = R \quad (3.10)$$

However, the complex number ( $i = \sqrt{-1}$ ) must be introduced to convert a capacitor's response to an AC signal to impedance because, in a purely capacitive circuit, the current will lead the voltage by  $\pi/2$  radians as the surfaces of the capacitor charge:

$$Z_C(w) = \frac{1}{Cwi} \quad (3.11)$$

When a resistor and capacitor are in parallel, as is the case for cell membranes, their impedances can be combined using the same equations used to combine two parallel resistors. Therefore, the equivalent impedance of the apical and basal membranes of epithelia ( $Z_a$  and  $Z_b$ , respectively) are:

$$Z_a(w) = \frac{R_a}{1 + C_a R_a w i} \quad (3.12)$$

$$Z_b(w) = \frac{R_b}{1 + C_b R_b w i} \quad (3.13)$$

These equivalent impedance equations are, in fact, equations for low-pass filters. The time constant for each of these filters is described by the time constant ( $\tau$ ) which is extracted from the coefficient of the terms multiplied by  $iw$  in the previous equations such that:

$$\tau = CR \quad (3.14)$$

The time constant term has units of seconds. The apical and basal membrane impedances can be summed together like two resistors in series to get the net transcellular resistance of an epithelium.

At this point, it is important to consider the assumptions regarding the lack of shunt capacitance. (1) The shunt membrane surface area ( $A_s$ ) is a tiny fraction of the total epithelial surface area. In other words, since the shunt membrane surface area is comprised, exclusively, of the border between cells, its area - relative to the apical and basal membranes - is minuscule. (2) The thickness of the tight junctions ( $d_s$ ) is much larger than the thickness of each cell membrane. The cell membrane thickness is approximately the height of two phospholipids whereas the thickness of the tight junctions can span much larger distances. For example, in the mammalian urinary bladder, the tight junctions are approximately 100 Å wide and up to 20 μm deep [71]. Thus, considering  $C_s = \varepsilon A_s / d_s$ , it is reasonable to assume that  $C_s \ll C_a$  and  $C_b$ . Therefore, the shunt impedance is simply:

$$Z_s(w) = R_s \quad (3.15)$$

and the total epithelial tissue impedance ( $Z_{abs}$ ) can be calculated by combining the paracellular shunt and the net transcellular impedance equations to get:

$$Z_{abs}(w) = R_{solA} + R_{solB} + \frac{R_s \left( \frac{R_a}{1+\tau_a w i} + \frac{R_b}{1+\tau_b w i} \right)}{R_s + \frac{R_a}{1+\tau_a w i} + \frac{R_b}{1+\tau_b w i}} \quad (3.16)$$

To confirm that this equation makes sense, consider the case where the circuit was measured at low frequencies (i.e.,  $w \approx 0$ ). In this case, Figure 4.1 can be simplified to Equation 3.9, the previous equation for the total tissue resistance.

Following similar logic from the derivation for the voltage divider ratio  $a$ , the intracellular pipette could be used to solve for an apical to basal impedance divider ratio. The limitations with hardware again come into play as two separate devices will be used to measure the voltage response of the tissue,  $TEP$ , and the apical membrane,  $V_a$ . Therefore, the exact current and voltage flowing through the apical membrane at any time will be difficult to resolve. However, the magnitude of the voltages at any point for the apical and basal membranes *can* be measured, just like with the voltage divider ratio where the impedance ratio ( $z$ ) is:

$$z = \frac{|Z_a(w)|}{|Z_b(w)|} = \frac{|\Delta V_a|}{|\Delta V_b|} \quad (3.17)$$

where

$$|Z_a(w)| = \sqrt{\frac{C_a^2 R_a^2 R_{solA}^2 w^2 + R_a^2 + 2 R_a R_{solA} + R_{solA}^2}{C_a^2 R_a^2 w^2 + 1}} \quad (3.18)$$

$$|Z_b(w)| = \sqrt{\frac{C_b^2 R_b^2 R_{solB}^2 w^2 + R_b^2 + 2 R_b R_{solB} + R_{solB}^2}{C_b^2 R_b^2 w^2 + 1}} \quad (3.19)$$

Thus, it can be shown that:

$$\lim_{w \rightarrow 0} z = a \quad (3.20)$$

If the reasonable assumption that the solution resistances are significantly smaller than the membrane resistances ( $R_{\text{solA}}$  and  $R_{\text{solB}} \ll R_a$  and  $R_b$ ), then these ratios can be used to approximate the ratio of individual membrane properties ( $a \approx R_a/R_b$ ). Furthermore, this impedance ratio allows the experimenter to monitor any changes in the resistance of the apical and basal solutions based on the following limit:

$$\lim_{w \rightarrow \infty} z = \frac{R_{\text{solA}}}{R_{\text{solB}}} \quad (3.21)$$

The ability to track and compensate for changes in Equation 3.21 is useful for scientists who want to apply solution gradients across the epithelia that would result in concomitant solution resistance fluctuations during the experiment. Normally, an experimenter would need to perform independent control experiments to calculate the changes in these values. However, Equation 3.17 enables real-time monitoring of solution resistance perturbations; completely eliminating this issue.

### 3.2.2 A workflow for the direct solution of membrane-specific properties

The values for  $R_a$ ,  $R_b$ ,  $R_s$ ,  $C_a$ , and  $C_b$  were calculated in a post-processing algorithm, developed in Matlab 2021b. To understand the function of the code, it is first useful to understand how the data was collected.

### *EIS hardware*

EIS measurements were performed with an Autolab PGSTAT204 with a FRA32M integrator module (Utrecht, Netherlands). The device was controlled with the provided NOVA 2.1.5 software to perform frequency sweeps from 0.1 Hz to 10 kHz. The NOVA software was used to send up to 5 simultaneous frequencies, spaced to approximately 5 unique measurements per decade. The PGSTAT working electrode was connected to the working electrode and counter electrode as shown in Figure 2.1, the sense and reference electrodes were connected to the basal and apical baths through the Ringer-based agar bridges (connected to Ag|AgCl reference electrodes in a saturated KCl bath), respectively. The remaining hardware was the same as described in the previous chapter.

### *Data processing*

Due to hardware limitations, it was necessary to capture the raw  $V_{pipette}$  and  $TEP$  data during each frequency sweep. This data was collected with an NI USB-6356 DAQ at 20.1 kHz (just above the Nyquist frequency). Each frequency sweep was saved to a unique text file and stored with the measurements recorded by the NOVA software for the transepithelial impedance data. At the end of each experiment, there was a folder that contained the raw data for each recording, combined with the raw data collected by the PGSTAT204 device.

The Matlab script used to fit the raw data used the following pseudo-code:

1. Load raw data into memory.
2. Append relevant metadata (e.g., date, cell line, passage number, etc.)
3. Make an array of random initial guesses for raw data.
4. Normalize measured values to fit within the range of  $0 \rightarrow 1$ .
5. Fit the data using the “lsqcurvefit” function available in Matlab.

6. Repeat until all recordings have been processed.
7. Store resulting data in a new, summary text file.

### 3.3 Results and discussion

#### 3.3.1 Theory validation using model cell circuit

To validate the application of the theory presented above, a circuit was constructed on a breadboard using commercially available resistors and capacitors Figure 3.1.

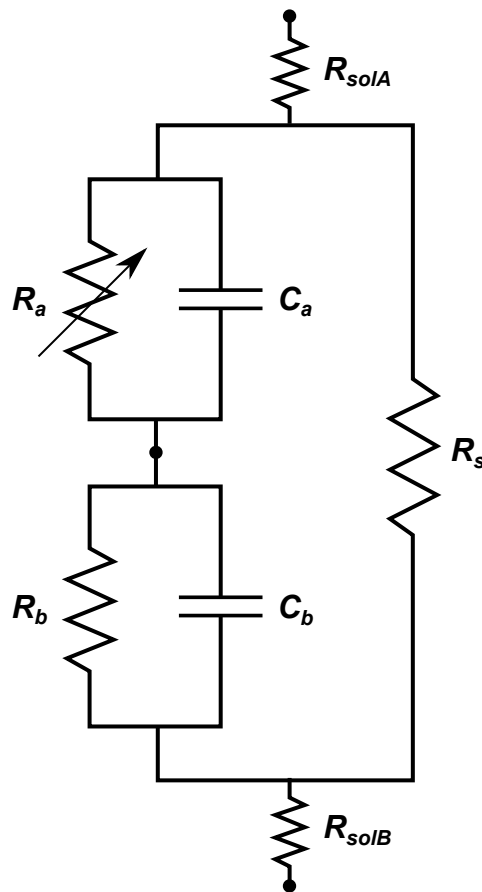


Figure 3.1: A model circuit, constructed out of resistors and capacitors, used to validate the direct measurement of epithelial circuit terms. The diagonal arrow across  $R_a$  indicates the parameter that was manually adjusted between each experiment.

The magnitude of the resistors and capacitors was selected to be similar in magnitude to the expected values of RPE, however, the exact values were unknown at this point. In

total, 6 unique values for  $R_a$  were tested while the remaining parameters were constant (Table 3.1).

Table 3.1: Selected resistance and capacitance values used in the model circuit to validate the intracellular technique for extracting membrane-specific properties of epithelia.

$R_a$ ( $\Omega$ )	$R_b$ ( $\Omega$ )	$R_s$ ( $\Omega$ )	$C_a$ ( $\mu F$ )	$C_b$ ( $\mu F$ )	$R_{solA}$ ( $\Omega$ )	$R_{solB}$ ( $\Omega$ )
<b>1000</b>	5524	3259	4.7	1	15	68
<b>2000</b>	5524	3259	4.7	1	15	68
<b>2500</b>	5524	3259	4.7	1	15	68
<b>3000</b>	5524	3259	4.7	1	15	68
<b>4200</b>	5524	3259	4.7	1	15	68
<b>4500</b>	5524	3259	4.7	1	15	68

For each experiment, the amplitude of the voltage response for the apical and basolateral membrane needed to be extracted from the raw data. This was done by using a power spectral density (PSD) plot and windowing. Specifically, the measurement start and end times of each frequency were stored in a metadata file. Thus, with a PSD, each time window corresponding to the desired frequency could be extracted from the plot and the power could be calculated by finding the peak value within the window (Figure 3.2).

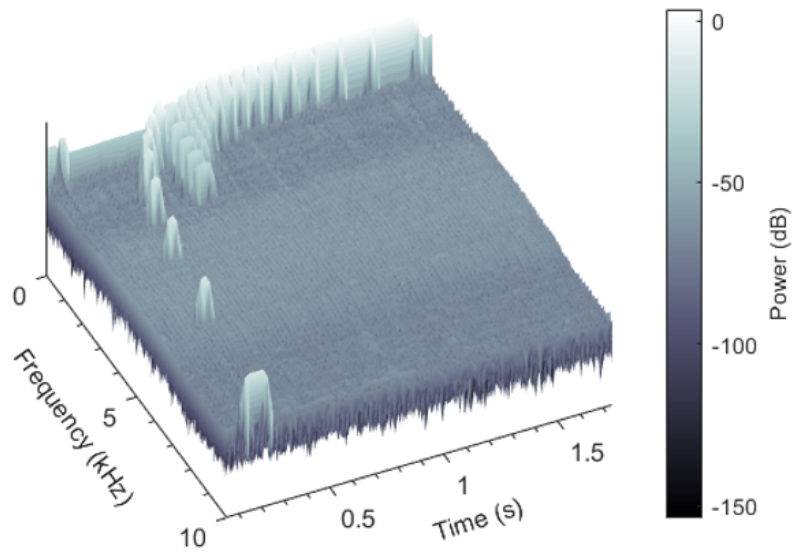


Figure 3.2: Power spectral density plot of the voltage response from a model cell used to measure membrane-specific properties of epithelia. The particular model circuit values, used to generate this plot, are shown in Table 3.1, row  $R_a = 4500 \Omega$ . The amplitude of the input current signal was  $5 \mu\text{A}$  and the data were sampled at 20.1 kHz.

The power ( $P$ ) could be converted to voltage amplitude ( $V$ ) using the following equation:

$$V = \sqrt{2P} \quad (3.22)$$

Using the extracted amplitudes for the impedance ratio at each distinct frequency, the following impedance ratio ( $z$ ) and Nyquist diagram could be fit using the Matlab code I created. The raw data and fit for this calibration data is shown in Figure 3.3

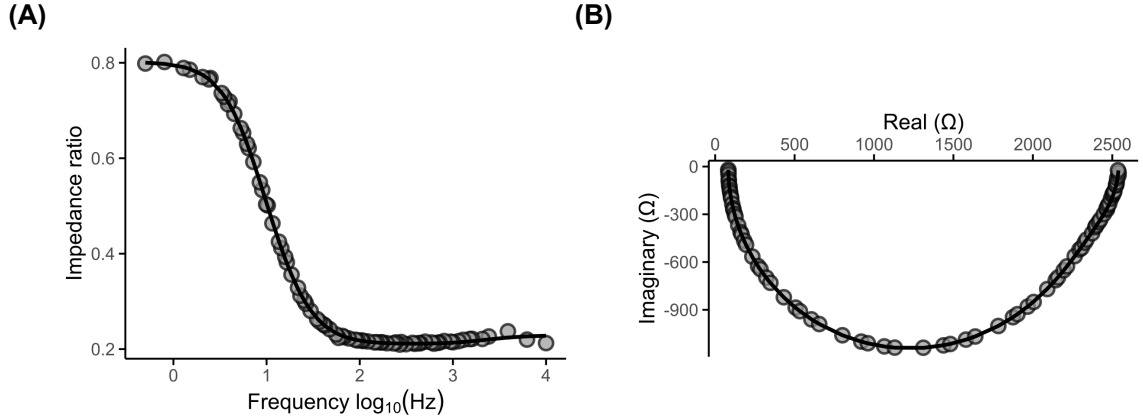


Figure 3.3: Representative (A) impedance ratio and (B) Nyquist diagram used to measure membrane-specific properties of epithelia when  $R_a$  was 4500  $\Omega$ .

The impedance ratio in Figure 3.3A can be sanity checked by looking at the limits as  $w \rightarrow 0$  and  $w \rightarrow \infty$ . According to Table 3.1, the actual voltage divider ratio for the plot is approximately 0.8 and the solution resistance ratio is approximately 0.2. The left and right asymptotes of Figure 3.3A appear to be trending to those limits, lending more confidence to the accuracy of the model presented. This process was repeated for all permutations of  $R_a$  in Table 3.1. The measured values for all permutations are collected in Table 3.2.

Table 3.2: Measured resistance and capacitance values from the model circuit used to validate the technique for extracting membrane-specific properties of epithelia.

$R_a$ ( $\Omega$ )	$R_b$ ( $\Omega$ )	$R_s$ ( $\Omega$ )	$C_a$ ( $\mu F$ )	$C_b$ ( $\mu F$ )	$R_{solA}$ ( $\Omega$ )	$R_{solB}$ ( $\Omega$ )
1004	5388	3281	4.76	1.02	16	70
2074	5653	3211	4.77	1.02	16	70
2553	5602	3229	4.77	1.02	16	69
3039	5585	3234	4.77	1.02	16	68
4211	5566	3241	4.79	1.02	16	68
4487	5546	3246	4.80	1.02	16	69

The magnitude of error for each measured circuit parameters was calculated and is shown in Figure 3.4.

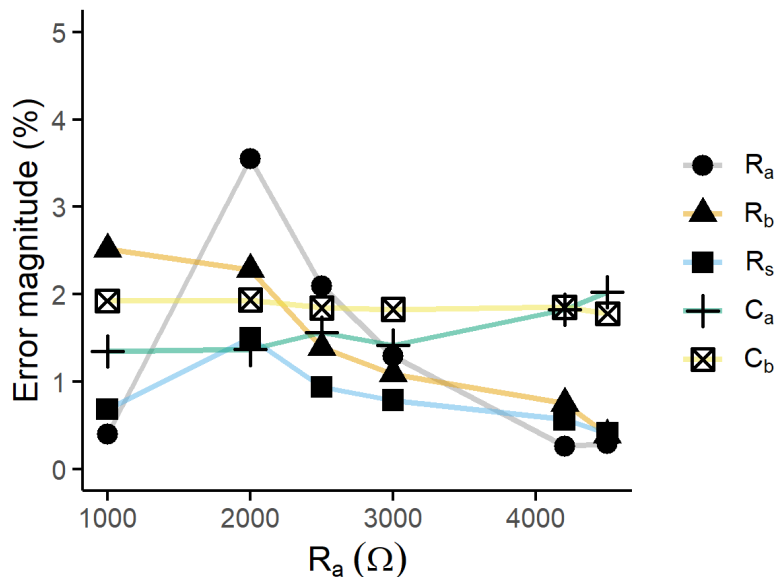


Figure 3.4: Fitting error magnitude for all permutations of the model cell using the intracellular measurement technique.

The error for all parameters was below 5% across the range tested. Therefore, if an individual property of the epithelia changes more than 5% of its baseline during a perturbation, it is very likely that my fitting algorithm would correctly identify which parameters were responsible and in what direction the change occurred. This is very useful information for an electrophysiologist.

### 3.3.2 Membrane-specific response of RPE induced by apical ATP

One of the standard methods for assessing RPE function involves the apical application of ATP [7]. ATP is selected because it impacts many mechanisms that all need to function correctly for a “healthy” cell response from normal RPE. Specifically, ATP increase in the SRS (apical) activates calcium signaling within RPE via apical membrane purinergic P2Y<sub>2</sub> receptors. Subsequent downstream signaling should lead to the inhibition of apical membrane K<sup>+</sup> channels and the activation of basolateral membrane Cl<sup>-</sup> channels that - along with appropriate counter ions - osmotically drive fluid across the epithelium from the apical to the basal side of the tissue (Figure 3.5) [7, 59].

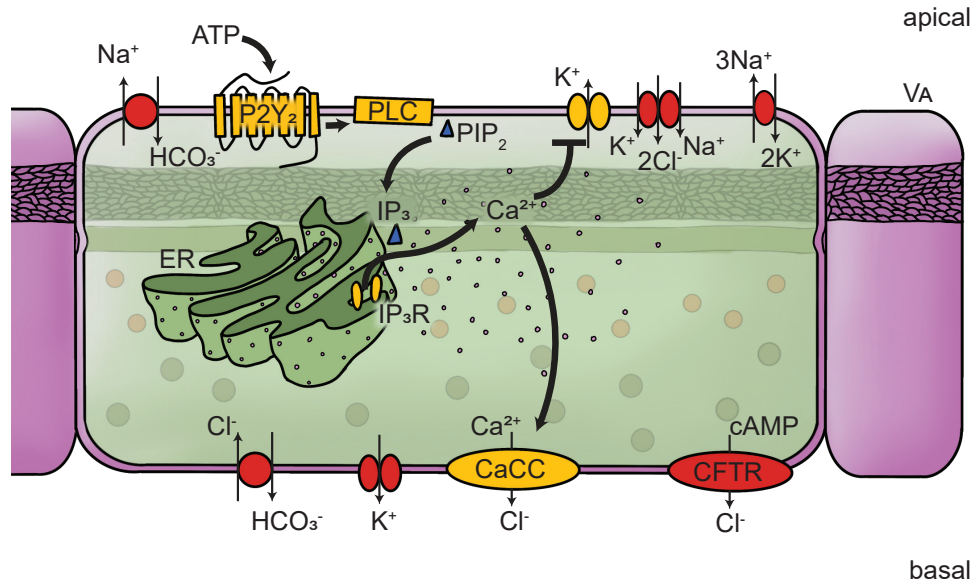


Figure 3.5: Theoretical mechanisms of RPE response to apical ATP. ATP stimulates P2Y<sub>2</sub> which, in turn, triggers a cascade of processes in RPE, indicated with black arrows. When measuring the membrane-specific electrophysiology of RPE, apical ATP should trigger the closing of apical K<sup>+</sup> channels, increasing  $R_a$  and activate basal Cl<sup>-</sup>-sensitive channels, lowering  $R_b$ .

Therefore, the techniques described in the preceding section were tested on RPE using ATP since the mechanisms are well studied and unique, membrane-specific responses should be detectable. An example of the extracted membrane-specific resistances during the application of 100  $\mu$ M ATP is shown in Figure 3.6 below.

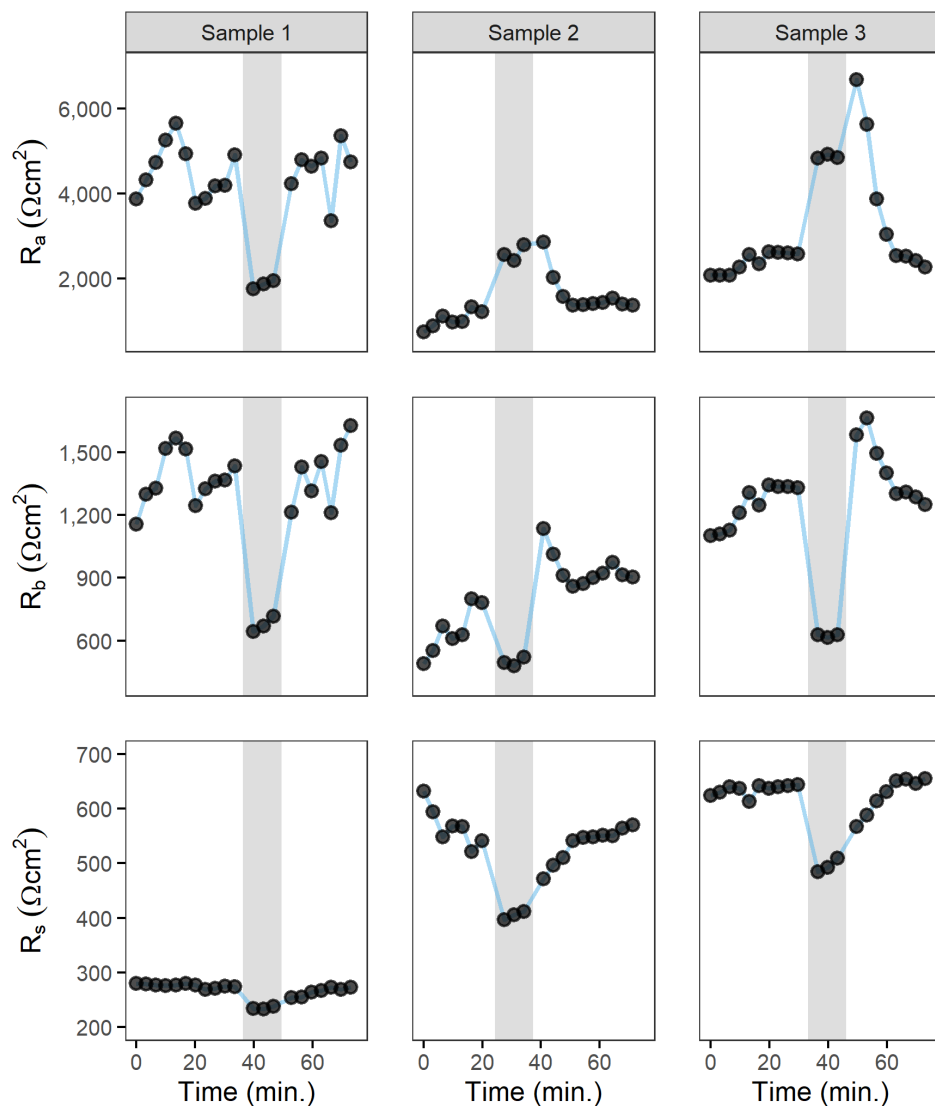


Figure 3.6: Example time series data of membrane-specific resistances extracted for an iPSC-RPE cell line called Z8. Points on the plot correspond to measured data before, during, and after 100  $\mu\text{M}$  apical ATP exposure. In particular, the grey box in the background indicates the time during ATP exposure. Cells were allowed to stabilize for, on average, 30 min prior to ATP application.

Immediately after the application of ATP, there were distinct, membrane-specific resistance responses detected with the techniques presented in this chapter. Interestingly, not all iPSC-RPE, of the same line of Z8 (seeded December 24, 2020, from patient line LORCF1, all tested around 300 days old, passage 27, and seeding density of 300k), responded the same to apical ATP. In particular, sample 1 in Figure 3.6 shows a strong decrease in apical

membrane resistance; the opposite direction observed in samples 2 and 3. The apical membrane resistance in samples 2 and 3 increased by 89% and 139%, respectively, while the apical membrane in sample 1 decreased by 62%. A similarly inverse response was detected in the capacitance of the tissue as seen in Figure 3.7 below.

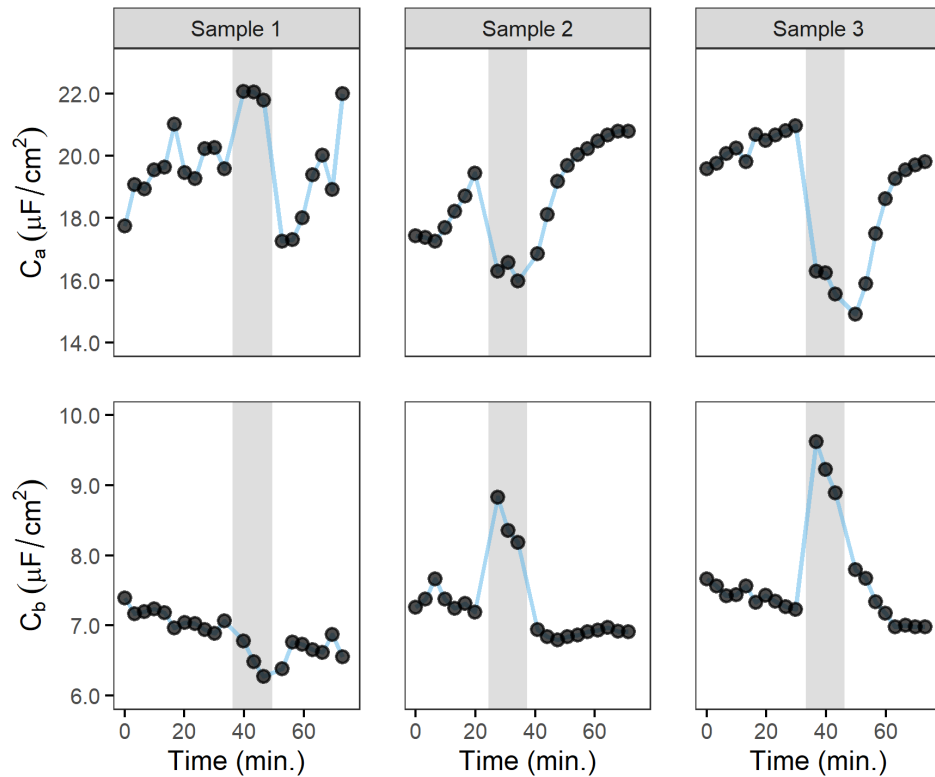


Figure 3.7: Example time series data of membrane-specific capacitances extracted for an iPSC-RPE cell line called Z8. Points on the plot correspond to measured data before, during, and after apical ATP. In particular, the grey box in the background indicates the time during ATP exposure. Cells were allowed to stabilize for, on average, 30 min prior to ATP application.

In Figure 3.7, samples 2 and 3, the apical membrane capacitances significantly decreased while the basal capacitances increased while sample 1 showed the opposite behavior;  $C_a$  and  $C_b$  changed by 12%, and -6%, respectively. The direction of the changes observed in membrane capacitance appears to be in concert with the membrane resistances. What is different from the membrane resistances is that the capacitances for *all* samples appear to slowly decrease during the application of ATP. Without a comprehensive study of

the theoretical mechanisms, it is not easy to speculate on the causes of these observations, given the lack of published literature that studies the properties of epithelia that most dramatically impact cell membrane capacitance.

### **3.4 Conclusions**

In this chapter, a novel technique for evaluating membrane-specific properties of epithelia is presented. This method leverages the pipette insertion algorithm - described in the previous chapter - to simultaneously record the intracellular and extracellular frequency response of epithelia. The technique was experimentally tested using a model circuit with known resistances and capacitances and is sensitive to changes in cell properties that are greater than 5% of baseline. ATP responses are frequently used to validate cell health in RPE due to the complex sequence of membrane-specific properties required for normal cell function. Therefore, these responses were tested with the techniques described in this chapter. From Figure 3.6, it is clear that membrane-specific properties can vary, even within a single donor line of epithelia (Z8). The detection of this variability with intracellular measurements highlights why it is critical to include membrane-specific measurements in future cell validation and drug screening protocols.

## CHAPTER 4

### APPLY ELECTROCHEMICAL IMPEDANCE SPECTROSCOPY TO ELUCIDATE MEMBRANE SPECIFIC PROPERTIES OF EPITHELIA USING EXTRACELLULAR ELECTROPHYSIOLOGY

#### 4.1 Motivation

Today, many scientists continue to rely on extracellular measurements to track the evolution of electrophysiological properties despite the additional, useful data that intracellular measurements provide. In particular, extracellular measurements are selected due to their simplicity, reduced cost, and significant throughput improvements. Furthermore, the non-invasive nature of extracellular experiments enables the return of Transwells back to culture after an experiment; assuming sufficient sterility.

The ability to measure the evoked responses *and* recovery of epithelia due to extracellular perturbations (e.g., 100  $\mu$ M ATP) provides extra insight into cell function and health [59]. Unfortunately, commercially available devices do not provide the hardware connections for simultaneous perfusion and electrophysiological assays (e.g., WPI's Endohm and Üssing chamber devices). In this chapter, a custom device was assembled to facilitate rapid and non-invasive extracellular analysis of RPE with continuous perfusion.

As discussed in earlier chapters, scientists have turned to a technique called EIS to maintain the throughput advantages of extracellular experiments while attempting to maximize the amount of information collected during an experiment [66, 62, 75, 76, 77]. For example, Schifferdecker and Frömter [62] considered that the apical and basal membranes of confluent epithelia are electrically separated via the strong connections they make with neighboring cells (e.g., with the tight junctions). Consequently, both membranes have the ability to uniquely transfer and store charge and, thus, should behave as distinct low-pass

filters, in series. Based on this theory, Schifferdecker and Frömter developed a mathematical model for epithelia that included two, parallel resistance and capacitance circuits in series (Figure 4.1B). In their model, the distinction between the transcellular (through the cell) and shunt pathways (around and between the cells) is lost. However, the equivalent filtering performed by the two membranes is preserved.

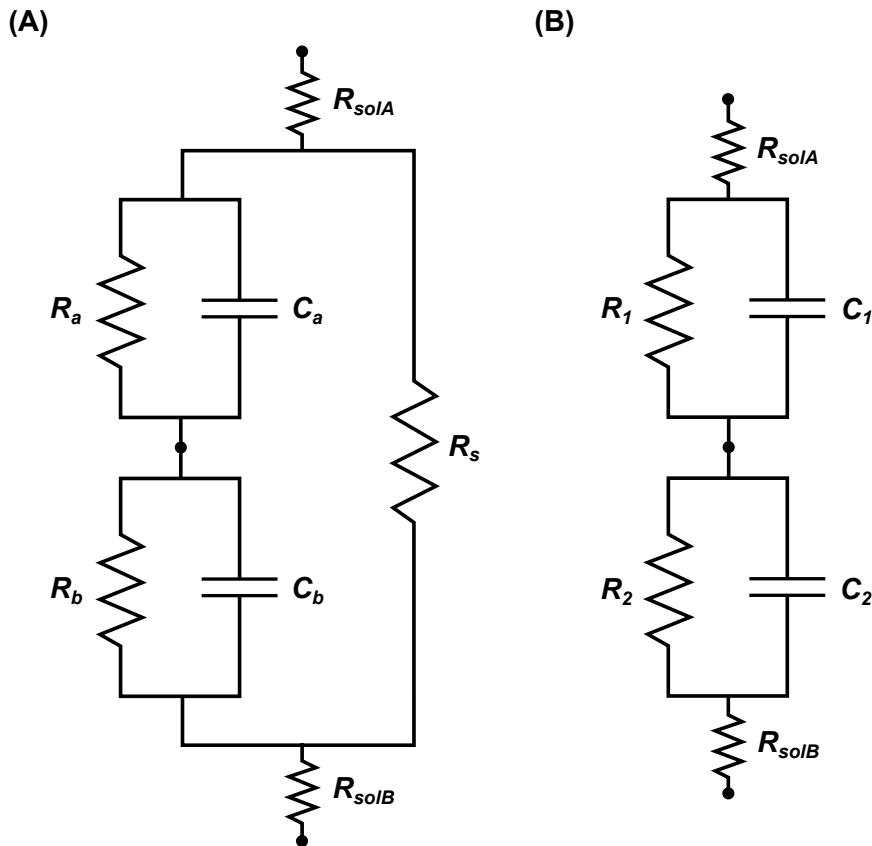


Figure 4.1: Two circuits that fit EIS measurements of epithelia with near-perfect correlation. (A) The most complex, physiologically-relevant circuit that can be analyzed with the addition of an intracellular pipette between the apical and basal cell membranes, as discussed in the previous chapter. (B) The most physiologically relevant circuit (representing two cell membranes, in series) that can be directly solved for using - exclusively - extracellular EIS.

With this model, epithelia can be evaluated using an equivalent circuit that is more detailed than the extracellular equivalent circuit measured with the Üssing chamber (Figure 1.5D), but not quite as detailed as the equivalent circuit measured with the previously described intracellular technique (Figure 4.1A). In Schifferdecker and Frömter's paper, they

explored the implications of this simplification using a plot called a Nyquist diagram (also sometimes called a Cole-Cole plot).

To generate the data visualized in a Nyquist diagram, the tissue is measured at many distinct frequencies by clamping an alternating current across the epithelia. At each frequency, the amplitude and phase of the resultant voltage is measured and the relationship between input and output signal is represented by the complex impedance ( $Z = \Re + i\Im$ ). The magnitude of the real and imaginary components at each distinct frequency can be plotted as a discrete point in a graph where the  $x$ -axis is the real component ( $\Re$ ) and the  $y$ -axis is the imaginary component ( $\Im$ ). A collection of these points - each a distinct frequency - is the Nyquist diagram.

This relationship can be visualized in a variety of other, standard diagrams, (e.g., Bode diagrams or Lissajous figures), but due to the specific properties of the epithelia, the Nyquist diagram is particularly powerful. For example, the asymptotes of the circuits in Figure 4.1, as the measurement frequency approaches either 0 or  $\infty$ , will always approach the  $x$ -axis at two distinct locations. The distance between these two asymptotes is directly equal to the tissue resistance. Furthermore, epithelia are submerged in aqueous solutions that - themselves - have a small amount of resistance. Normally, this solution resistance is calculated before an experiment and subtracted from subsequent data, but, because the solution's resistance is in series with the two membranes and has negligible capacitance, it appears as a small shift away from  $\langle 0, 0 \rangle$  on the  $x$ -axis in a Nyquist diagram. In other words, the distance between the origin and the first intersection of the real axis is exactly equal to the solution resistance and eliminates the need to calculate this property before an experiment.

Schifferdecker and Frömter explored other graphical relationships between circuit properties of Figure 4.1B and the Nyquist diagram. For example, they examine how a change in one of the two low pass filters' time constants ( $\tau$ ) would influence the shape of the corresponding Nyquist diagram (Figure 4.2).

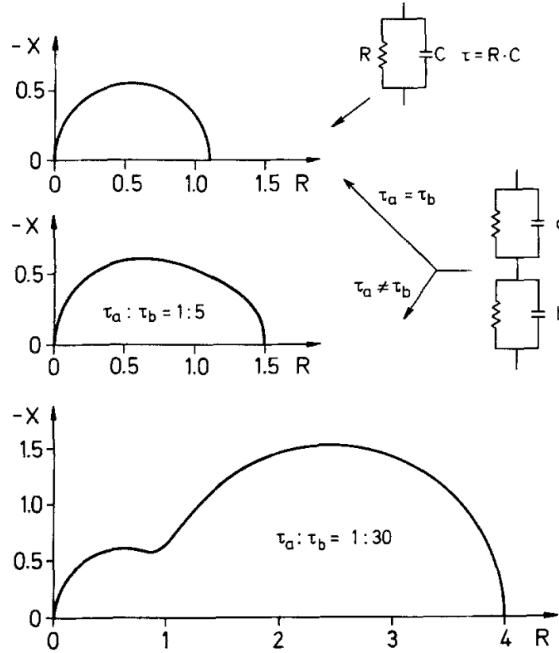


Figure 4.2: Nyquist diagram of 2 parallel RC circuits placed in series. The figure shows how changing only the equivalent basolateral time constant,  $\tau_b$ , changes the shape of a Nyquist plot; demonstrating how individual membrane properties may be visible using EIS. In  $k\Omega$  and  $\mu F$ , respectively: (Upper panel)  $R_a = 1$ ,  $C_a = 5$  and  $R_b = 0.1$ ,  $C_b = 50$ . (Center panel)  $R_a = 1$ ,  $C_a = 5$  and  $R_b = 0.5$ ,  $C_b = 50$ . (Lower panel)  $R_a = 1$ ,  $C_a = 5$  and  $R_b = 3$ ,  $C_b = 50$  [62].

Despite the investigations that Schifferdecker and Frömter began in their paper, scientists have primarily focused on finding simple, independent measurements or assumptions about epithelia that enable the direct solution of (derived from Figure 4.1A) when measured using extracellular EIS [5]. This is likely because the exact magnitudes of the resistances and capacitances in the extracellular EIS circuit (Figure 4.1B) are not correlated - in any way - to the membrane-specific properties of elements in Figure 4.1A.

Kreindler et al., for example, measured the shunt resistance pathway in a separate experiment (prior to EIS) by extrapolating the y-intercept of a tissue conductance versus short circuit current plot and assuming that the paracellular resistance remains constant throughout the experiment [51]. Additionally, during my collaboration with Cottrill et al. [70], we assumed that the paracellular resistance always contributes 71% of the net tissue conductance ( $G_t = 1/R_t$ ) in a CF study of lung epithelia. These assumptions and measurements

are critical for completely solving , but are some combination of (1) destructive to the cells, (2) need to be re-verified for each, unique cell line and experiment protocol, and (3) potentially miss interesting cell behavior because it is necessarily assumed deviation from normal function will not occur.

The assumption made by Kriendler et al. and with Cottrill et al, for instance, would have obfuscated (potentially even misled) the interpretation of what happened with the epithelia recorded in Figure 3.6. Generally, the shunt resistance was neither a constant nor was it a fixed proportion of total tissue resistance. In fact, in all three RPE recordings, the shunt resistance both (1) changed during the application of ATP and (2) the magnitude of the change was not proportional to the total tissue resistance (specifically, from Figure 3.6,  $R_s/TER$  went from 1.05 to 1.12, 1.3 to 1.13, and 1.2 to 1.1, from before to during ATP exposure in (A), (B), and (C), respectively).

This error is a major issue with conventional techniques. Instead of trying to solve for the complete circuit in Figure 4.1A using extracellular EIS and potentially erroneous or ill-posed assumptions, I propose to instead observe if changes in time constants can be used as a crude analog of voltage divider ratio ( $a$ ); providing a high throughput and simple-to-perform technique to bridge the gap between extracellular and intracellular measurements. This could be particularly powerful during a drug screening, for example. An experimenter could use this crude bridge to quickly identify compounds or interactions that generate membrane-specific responses that should be followed up with the more comprehensive (and accurate) intracellular and EIS combination.

At best, extracellular EIS has provided scientists with an additional transepithelial capacitance (TEC) term that, to date, lacks a rigorous link to real cell properties. It is likely that cell capacitance is linked to cell morphology, however, which morphological parameters are most strongly correlated to capacitance needs further investigation (e.g., cell cross-sectional area, membrane surface area, apical process density, length, and type, as well as basal membrane folding). At best, the equation for capacitance (Equation 1.5) indicates that

capacitance can be used as an analog for cell surface area (given membrane thickness and dielectric constant do not change from experiment to experiment). However, experimental data are lacking to validate this claim [78, 74, 79, 72, 64, 80, 67, 81, 66, 62, 71, 69, 82]. Collaborators at the National Eye Institute (NEI) have been working on a machine learning model for extracting individual cell morphology parameters of fixed cells spanning large cross-sectional areas (e.g., the entire human eye) with a tool called REShAPE. One of the parameters that this tool can measure is the cross-sectional area of individual cells. With early access to REShAPE and the techniques presented in previous chapters, this chapter aims to: (1) evaluate how extracellular EIS can be used to quantify how chamber designs affect transepithelial function, (2) compare intracellular pipette data with extracellular EIS in order to determine the links between changing time constants and membrane-specific properties, and (3) compare morphological properties of epithelia with cell capacitance measurements to provide more specific insights into the meaning of these cell properties.

#### 4.1.1 Methods

#### 4.1.2 Immunostaining

The protocol for immunostaining iPSC-derived RPE monolayers in this work has been described previously [83]. In short, after an experiment was completed, the transwell punch-out (7 mm in diameter), was fixed in 4% paraformaldehyde (Electron Microscopy Science, 157-4-100) for 12 min. The sample was then rinsed three times, over the course of 15 min, with PBS at room temperature and stored at 4 °C. Immunohistochemistry blocking solutions (IBS) consisted of 500 mL of 1x Dulbecco's phosphate-buffered saline (DPBS, Line Technologies, 14190250), 5% (mass/volume) bovine serum albumin (Sigma Aldrich, A3311), 0.5% (mass/volume) bovine serum albumin (Sigma Aldrich, A3311), 0.5% (mass/volume) TWEEN21 (Sigma Aldrich, P2287-100ML). Fixed cells were washed with IBS three times and permeabilized for 2 hours with IBS at room temperature. Cells were then stained with anti-ZO-1 Alexa Fluor 488 (to study the tight junctions) and Phal-

loidin Alexa Fluor 555 (to visualize cell boundaries by targeting actin filaments). These stains were incubated at room temperature for 1 hour. Additionally, nuclei were stained with Hoechst 33342 dye for 15 minutes at room temperature. After staining, cells were washed with DPBS and mounted onto slides. All images were captured using a Zeiss Axio Scan Z1 slide scanner. Z-stacks were acquired over 50  $\mu\text{m}$  along the z-direction with 1.5  $\mu\text{m}$  steps and maximum intensity projections were used for all analysis.

#### 4.1.3 Scanning electron microscopy

The protocol for SEM imaging of RPE has been published previously [84]. In short, RPE were fixed in 4% paraformaldehyde (Electron Microscopy Science, 157-4-100) for 12 min, immediately following an experiment. The sample was then rinsed three times, over the course of 15 min, with PBS at room temperature and stored at 4 °C. EM fixative (2.5% glutaraldehyde Grade 1 (Sigma Aldrich) and 10 mM  $\text{CaCl}_2$ ) was added to HEPES buffer and the cells were incubated overnight. Samples were mounted on conductive carbon adhesive stubs and imaged using SEM (S-4800 Hitachi electron microscope).

#### 4.1.4 Mathematical modeling

The detailed mathematics describing the relationships between current, voltage, and impedance are described, in detail, in the previous chapters. In this section, it is useful to highlight the additional methods for interpreting Nyquist diagrams and what portions of the diagram mean, in terms of electrophysiology.

Using the equations for the impedance of resistors and capacitors in Equation 3.10 and Equation 3.11, and combining them using the same rules for resistors, the impedance of the equivalent circuit in Figure 4.1B is:

$$Z_{12}(w) = R_{\text{solA}} + R_{\text{solB}} + \frac{R_1}{1 + \tau_1 w i} + \frac{R_2}{1 + \tau_2 w i} \quad (4.1)$$

For all measurement frequencies ( $w$ ), the magnitude and phase shift for both circuits shown in Figure 4.1 must necessarily be identical. Thus, the following equation must be true:

$$Z_{abs}(w) \equiv Z_{12}(w) \quad (4.2)$$

Setting these two equations equal to each other, and cross-multiplying the denominators, two equivalent, 4th order polynomial equations ( $w^4$ ) in the following form arises:

$$\alpha_1 w^4 + \beta_1 w^3 + \gamma_1 w^2 + \delta_1 w^1 + \epsilon_1 w^0 = \alpha_2 w^4 + \beta_2 w^3 + \gamma_2 w^2 + \delta_2 w^1 + \epsilon_2 w^0 \quad (4.3)$$

Given the rules for equivalent polynomials, the coefficients corresponding to each order term can be set equal to each other. The 4th order terms ( $\alpha_1 = \alpha_2$ ) yields a trivial result of ( $1 = 1$ ). However, the following four equations arise from the remaining coefficients:

$$\beta_1 = \beta_2 \rightarrow \frac{C_1 C_2}{C_1 + C_2} = \frac{C_a C_b}{C_a + C_b} \quad (4.4)$$

which states, in effect that the TEC for both circuits should be identical. The 2nd and 1st order terms produce complicated equations:

$$\begin{aligned}
\gamma_1 = \gamma_2 \rightarrow 0 = & C_1 C_2 R_1 R_2 R_a R_s + C_1 C_2 R_1 R_2 R_b R_s - \\
& C_1 C_a R_1 R_2 R_a R_b - C_2 C_a R_1 R_2 R_a R_b - C_1 C_b R_1 R_2 R_a R_b - \\
& C_2 C_b R_1 R_2 R_a R_b - C_1 C_a R_1 R_2 R_a R_s - C_2 C_a R_1 R_2 R_a R_s - \\
& C_1 C_b R_1 R_2 R_b R_s - C_2 C_b R_1 R_2 R_b R_s + C_1 C_a R_1 R_a R_b R_s + \\
& C_2 C_a R_2 R_a R_b R_s + C_1 C_b R_1 R_a R_b R_s + C_2 C_b R_2 R_a R_b R_s - \\
& C_a C_b R_1 R_a R_b R_s - C_a C_b R_2 R_a R_b R_s
\end{aligned} \tag{4.5}$$

and

$$\begin{aligned}
\delta_1 = \delta_2 \rightarrow 0 = & C_1 R_1 R_2 R_a + C_2 R_1 R_2 R_a + C_1 R_1 R_2 R_b + C_2 R_1 R_2 R_b + \\
& C_1 R_1 R_2 R_s + C_2 R_1 R_2 R_s - C_1 R_1 R_a R_s - C_2 R_2 R_a R_s - \\
& C_1 R_1 R_b R_s - C_2 R_2 R_b R_s + C_a R_1 R_a R_b + C_a R_2 R_a R_b + \\
& C_b R_1 R_a R_b + C_b R_2 R_a R_b + C_a R_1 R_a R_s + C_a R_2 R_a R_s + \\
& C_b R_1 R_b R_s + C_b R_2 R_b R_s - C_a R_a R_b R_s - C_b R_a R_b R_s
\end{aligned} \tag{4.6}$$

The 0th order coefficients produce another simple relationship:

$$\epsilon_1 = \epsilon_2 \rightarrow R_1 + R_2 = \frac{R_s (R_a + R_b)}{R_s + R_a + R_b} \tag{4.7}$$

which states that the total tissue resistances of both circuits should be equal. As described in the Motivation for this chapter, the total tissue resistance can be calculated by measuring the distance between the intersection points on the  $x$ -axis of the Nyquist diagram. The equation above states that the total tissue capacitances must be directly equal, however, it is not obvious from the diagram *how* they are related. Considering that the Nyquist plot

is really a 3-dimensional plot with coordinates  $\langle \Re(Z), \Im(Z), w \rangle$ , if one integrates the real ( $\Re$ ) part of the impedance equation with respect to the measurement frequency,  $w$ , the following relationship arises:

$$\int_0^{\infty} \Re(Z_{12}(w) - R_{solA} - R_{solB}) dw = \frac{\pi}{2} \left( \frac{1}{C_1} + \frac{1}{C_2} \right) \quad (4.8)$$

Following the rules of equivalent capacitors, the TEC ( $C_t$ ) for Figure 4.1B is equal to:

$$\frac{1}{C_t} = \frac{1}{C_1} + \frac{1}{C_2} \quad (4.9)$$

Therefore, given the relationships derived above, it can be shown that the following is also true:

$$\frac{1}{C_t} = \frac{2}{\pi} \int_0^{\infty} \Re(Z_{abs}(w) - R_{solA} - R_{solB}) dw \quad (4.10)$$

## 4.2 Results and discussion

### 4.2.1 Chamber design and extracellular epithelial properties

A custom device was assembled to rapidly and noninvasively evaluate the evoked responses and recovery of RPE to extracellular ATP (Figure 4.3).

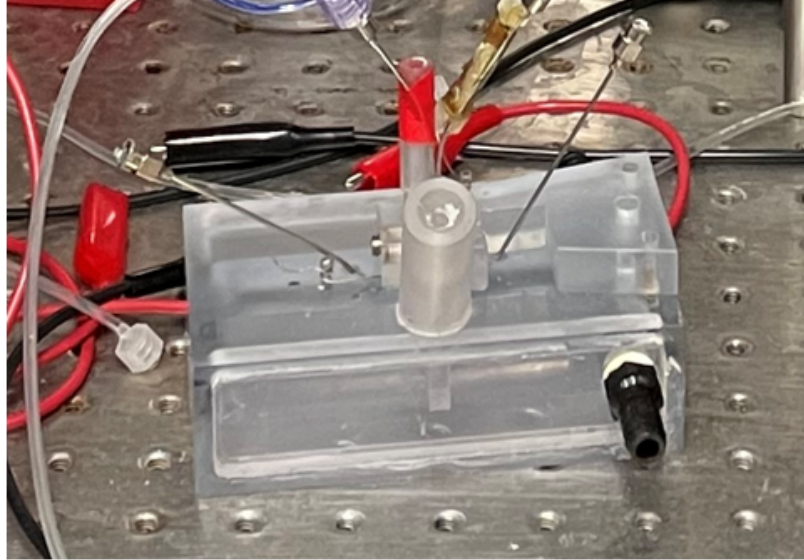


Figure 4.3: Picture of a custom chamber used to study intact, 12-well Transwells. This device is referred to as the “perfusion” chamber in this chapter.

A schematic of this chamber is shown in Figure 4.4.

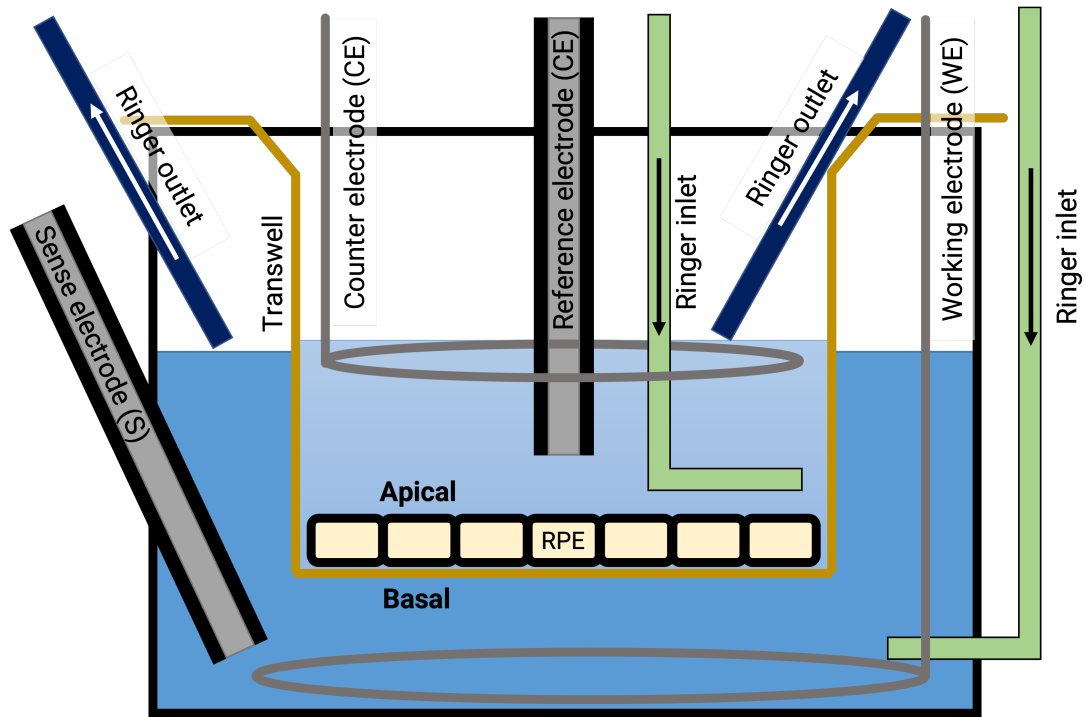


Figure 4.4: Schematic of custom chamber used to study intact, 12-well Transwells. An intact Transwell is suspended in basal solution by resting the upper ring on the Acrylic chamber. Ringer inlets are depicted with green boxes with an arrow indicating the direction of flow. Ringer outlets were vacuum driven and are shown with flow indicated with a white arrow. The height of the solution could be adjusted by raising or lowering the ringer outlets. Ringer inlets were heated to approximately 36 °C by cross flow heat exchangers containing hot water.

The custom “perfusion” chamber in Figure 4.3 and Figure 4.4 was created using the same Acrylic material as the Üssing chamber but was designed to interface with an intact, 12-well Transwell insert (Corning costar 3460). Ag|AgCl wires were used as the working and counter electrodes. These electrodes were shaped into a symmetric ring of maximum diameter that fits inside the chamber and placed as far from the epithelia as possible to maximize uniformity of the current flux across the tissue. The sense and reference electrodes (used to measure TEP), were single-junction KCl reference electrodes. The KCl reference electrode was constructed with an Ag|AgCl wire that was inserted in a glass body (1.5 mm outer diameter), backfilled with 3 M KCl. The terminus of these electrodes was made of a Vycor frit that enabled electrical contact between the 3 M KCl solution and the perfusate.

Ag|AgCl electrodes were selected due to their rapid and reversible redox reactions, and the bridges were designed to minimize the effect of drifting  $\text{Cl}^-$  ion concentrations on the electrode junction potential. The sense and reference electrodes were inserted through the cylinders extruding through the top of the device pictured in Figure 4.3 such that they were positioned as close as possible to the tissue. The design of the Acrylic cylinders included a kinematic constraint for the electrodes to ensure that the distance between the tissue and voltage sensing probes was consistent across all experiments.

Custom chambers are commonly designed to execute unique or complex experiments when commercially available devices do not exist. Control experiments must be performed to verify the physiological mechanisms of epithelia in the new chamber are not significantly different than previous setups. For example, the magnitudes of extracellular tissue properties in normal Ringer's solution (see Chapter 2 Methods for recipe) should be compared. Therefore, to demonstrate how tissue function can be validated using EIS, a single plate of iPSC-RPE (to minimize genetic variation), was split in half and one half was tested in the Üssing chamber while the other half was tested in the perfusion chamber (Figure 4.5).

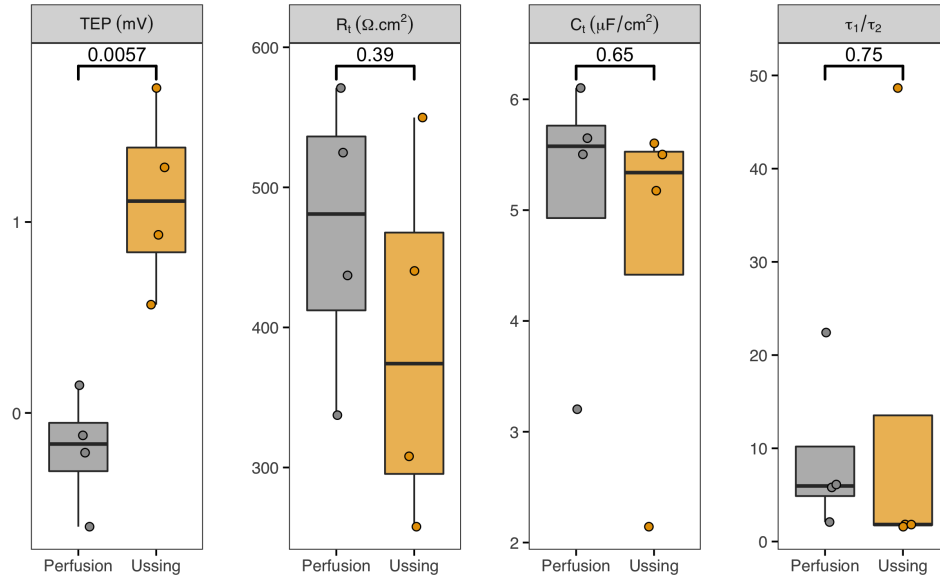


Figure 4.5: Perfusion versus Ussing chamber extracellular electrophysiological differences (n=4). The iPSC-RPE from a single cell line (Z8) were measured in both the traditional Ussing chamber and the custom perfusion chamber using EIS. Numbers above the bracket correspond to the p-value from a t-test between the two chambers.

No statistical differences were observed between resistance, capacitance, and time constant ratio ( $R_t$ ,  $C_t$ , and  $\tau_1/\tau_2$ , respectively) studied in the two chambers after normalizing for the cross-sectional area. However, there was a statistically significant difference between the TEP for cells studied in the two chambers. TEP is sensitive to temperature, perfusion rate per chamber volume, and hydrostatic pressure during an experiment. For example, during Ussing chamber setup, adjusting the apical solution height dramatically affected epithelial TEP. Furthermore, solution temperatures in each chamber were measured to be different by up to 1.5 °C, depending on the ambient temperature of the room. These effects have been observed in literature before, but the exact mechanisms are still poorly understood [85, 86, 82, 87].

Furthermore, to ensure that the perfusion device can maintain the health and function of epithelia during long experiments, a simple experiment was devised to last at least 45 min; sufficient for rigorous RPE experiments performed in literature ([59, 7]). During this experiment the tissues were briefly exposed (approximately 10 min) to 100  $\mu\text{M}$  ATP at the

apical membrane. The time series data for all experiments were normalized for two reasons: (1) if the cells were in an “unhealthy” physiological state, tissue properties will drift towards 0 (unstable), regardless of starting magnitude. (2) The relative magnitude and direction (positive or negative) of the response evoked by ATP, should be similar for both chambers. Specifically, if cell function is altered by chamber design, the magnitude and direction of the evoked response in the new chamber will likely appear different because the mechanisms involved in RPE ATP response require numerous channels to be expressed and functioning normally ([59, 7]). The normalized tissue resistance, for example, is shown in Figure 4.6

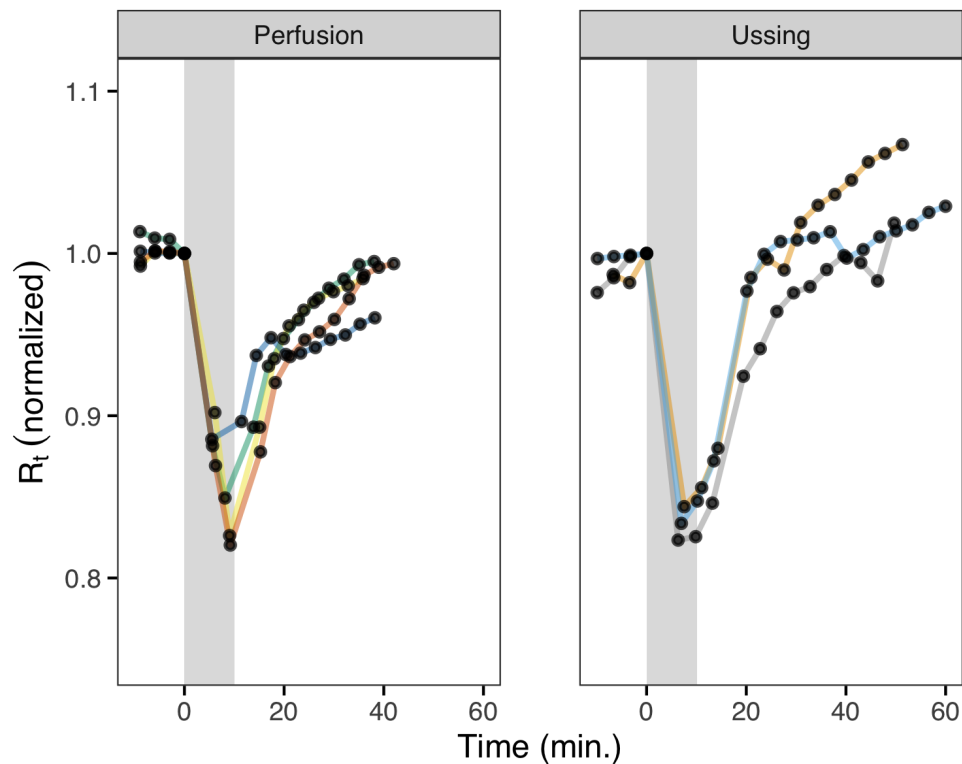


Figure 4.6: All normalized total tissue resistance ( $R_t$ ) response of iPSC-RPE (Z8) to  $100\ \mu\text{M}$  apical ATP exposure. Time 0 min corresponds to the moment of ATP exposure. The average duration of ATP exposure is shown by the grey box (approximately 10 min).

Figure 4.6 shows that for both the perfusion and Ussing chambers, the epithelia responded with a similar magnitude and direction after ATP exposure. Furthermore, after ATP, the epithelia in both chambers returned to within 95% of baseline within 40 min.

Most importantly, in neither chamber did the cell line start to lose resistance after up to an hour; a critical indicator of cell death. Furthermore, the TEP of the cells in both chambers was similar (Figure 4.7).

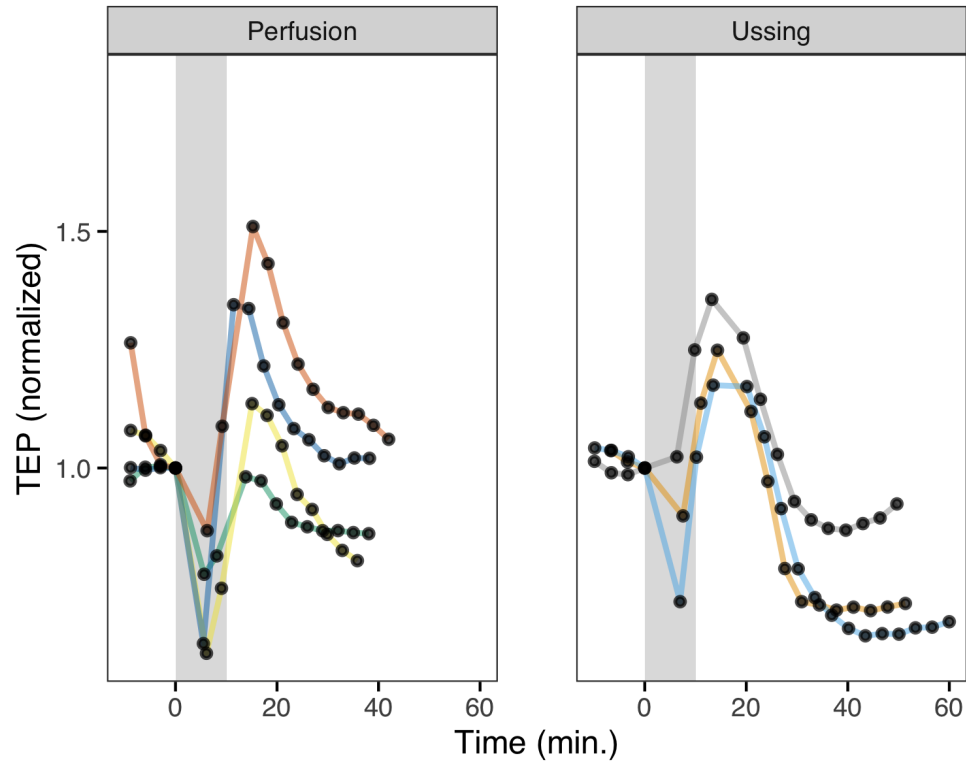


Figure 4.7: All normalized tissue potential (TEP) response of iPSC-RPE (Z8) to 100  $\mu$ M apical ATP exposure. Each trace is a unique recording normalized to the TEP right before apical 100  $\mu$ M ATP exposure. Time 0 min corresponds to the moment of ATP exposure. The average duration of ATP exposure is shown by the grey box (approximately 10 min).

The preceding plots show that cell function does not appear to be impacted by chamber choice for long-duration experiments. Conventionally, if the chamber is (1) maintained from 32  $^{\circ}$ C to 37  $^{\circ}$ C, (2) the perfusate is bubbled with sufficient oxygen (approximately 10%  $O_2$  for RPE), and (3) the flow rate is fast enough to minimize the un-stirred layer and osmotic effects due to evaporation yet slow enough to avoid large shearing forces on the epithelia (from 2 mL/min to 5 mL/min), it appears that cell function remains stable over long-duration experiments. Finally, the magnitudes of the extracellular tissue properties need to be compared to ensure cell function is likely not impacted, in some significant way,

due to chamber configuration or design (Figure 4.5).

The previous data encapsulate the breadth of control experiments traditionally performed to validate the health of epithelia in a new chamber. However, using EIS, extra tissue parameters can be evaluated. For example, the tissue capacitance ( $C_t$ ) can be determined (Figure 4.8).

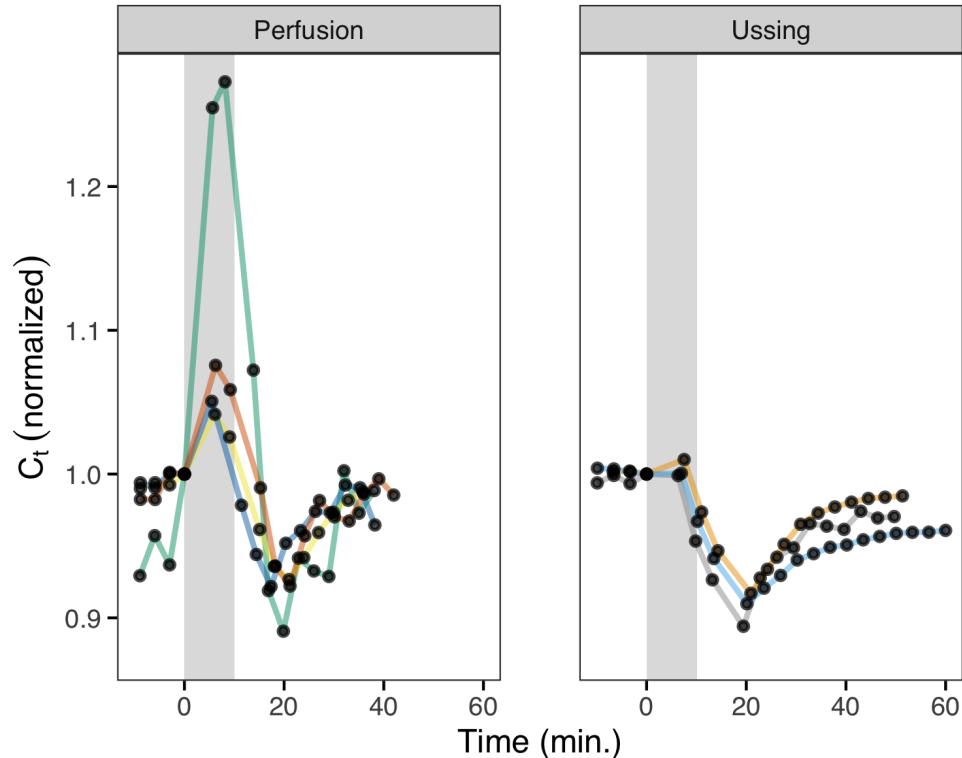


Figure 4.8: All normalized tissue capacitance ( $C_t$ ) response of iPSC-RPE (Z8) to 100  $\mu$ M apical ATP exposure. Time 0 min corresponds to the moment of ATP exposure. The average duration of ATP exposure is shown by the grey box (approximately 10 min).

Figure 4.8 - only possible to obtain using EIS - reveals an interesting divergence between the direction and magnitude that the epithelia respond to apical ATP. First, the perfusion chamber capacitance appears to be noisier than the  $\ddot{U}$ ssing chamber, however, this can be explained by the much larger cross-sectional area of the perfusion chamber. The perfusion chamber has a cross-section of 1.12 cm<sup>2</sup> while the  $\ddot{U}$ ssing chamber has a cross-sectional area of 0.114 cm<sup>2</sup>. With a smaller cross-sectional area, the tissue has a larger voltage response to the clamped current flux (35  $\mu$ A/cm<sup>2</sup> for the  $\ddot{U}$ ssing chamber and

9  $\mu\text{A}/\text{cm}^2$  for perfusion chamber). The maximum current for the perfusion chamber could not be clamped any higher without the addition of new stability and clamping errors due to specific hardware limitations. Thus, the lower current flux in the perfusion chamber likely contributed to the larger variation between measurements.

The second interesting phenomenon is the notably different capacitance response magnitude and direction to apical ATP. In particular, the tissue capacitance increased during apical ATP exposure by an average of 11%, while it decreased in the Üssing chamber by an average 3%. The perfusion chamber's larger total volume - while utilizing an identical perfusion rate of 4.5 mL/min - resulted in a slower replacement of chamber volume per unit time. As observed with the first few data points recorded in Figure 4.7, stabilization after perturbations in extracellular solution is much slower for the perfusion chamber. Therefore, it is likely that the concentration of ATP took longer to reach 100  $\mu\text{M}$ . It is possible that the RPE have additional mechanisms that respond to lower concentration or that are attenuated when ATP is too high. Further evidence towards this hypothesis stem from the magnitude and time course of the epithelial recovery after removing apical ATP. Specifically, in both the perfusion and Üssing chambers, the capacitance dropped for about 20 min before returning to baseline at nearly identical rates. In other words, the positive deflection in tissue capacitance - observed exclusively in the perfusion chamber during apical ATP - did not affect the magnitude and direction of the recovery after a 10 min exposure.

Similarly, the extracellular time constant ratio ( $\tau_1/\tau_2$ ) - only possible to obtain using EIS - yields another surprising result (Figure 4.9).

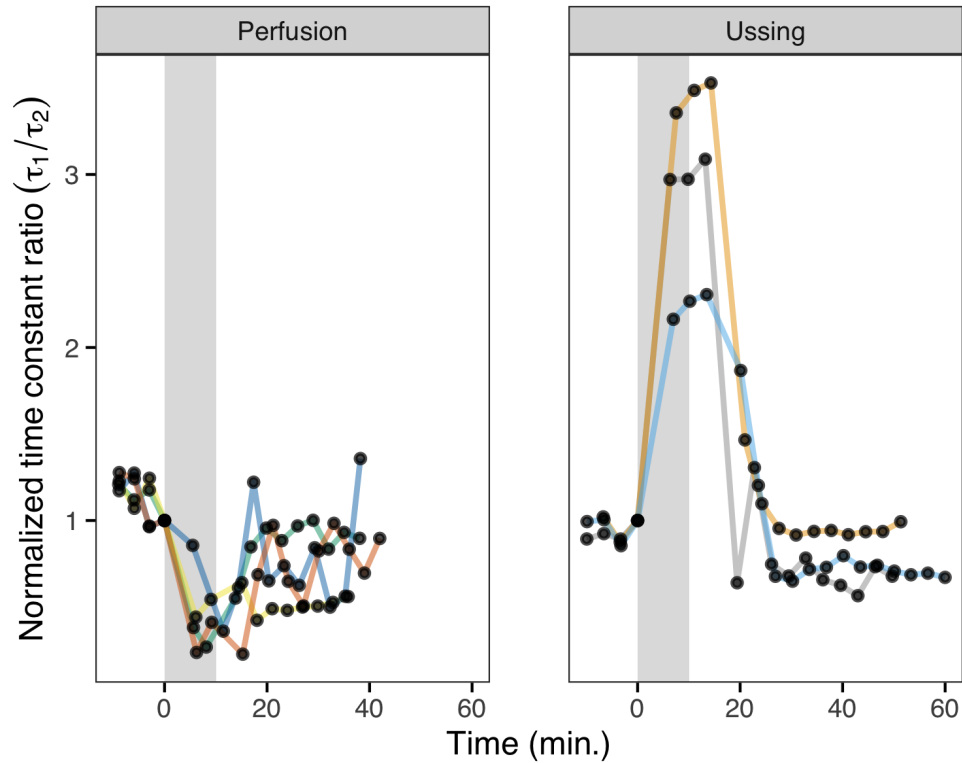


Figure 4.9: All normalized extracellular time constant ratios ( $\tau_1/\tau_2$ ) for iPSC-RPE (Z8) response to 100  $\mu\text{M}$  apical ATP exposure. Time 0 min corresponds to the moment of ATP exposure. The average duration of ATP exposure is shown by the grey box (approximately 10 min).

The time constant ratio approximates the membrane-specific ratio of time constants for the apical and basal membranes ( $\tau_a/\tau_b$ ). Figure 4.9 indicates distinctly different membrane responses during ATP exposure between the two chambers, despite a lack of statistical difference in baseline value (Figure 4.5). However, during recovery after ATP exposure, both chambers returned towards their starting values, suggesting the inverse time constant ratio responses are reversible.

Little is known about how to interpret the tissue capacitance and the ratio of time constants response of RPE to ATP exposure. However, without the addition of these parameters, no significant difference in epithelial response to apical ATP can be detected. Thus, it appears that EIS can be used to reveal unique and previously unobservable phenomenon in epithelia such as the possible dosage dependant response of iPSC-RPE to apical ATP.

#### 4.2.2 Extracellular EIS as an analog for intracellular properties

The methods section of this chapter discussed the potential correlation between membrane time constants and the - previously unobservable - membrane-specific voltage divider ratio  $a$ . To evaluate this theory, epithelia that were recorded using traditional intracellular methods were also recorded with extracellular EIS. An example of Nyquist diagram changes observed during extracellular application of apical ATP are shown in Figure 4.10.

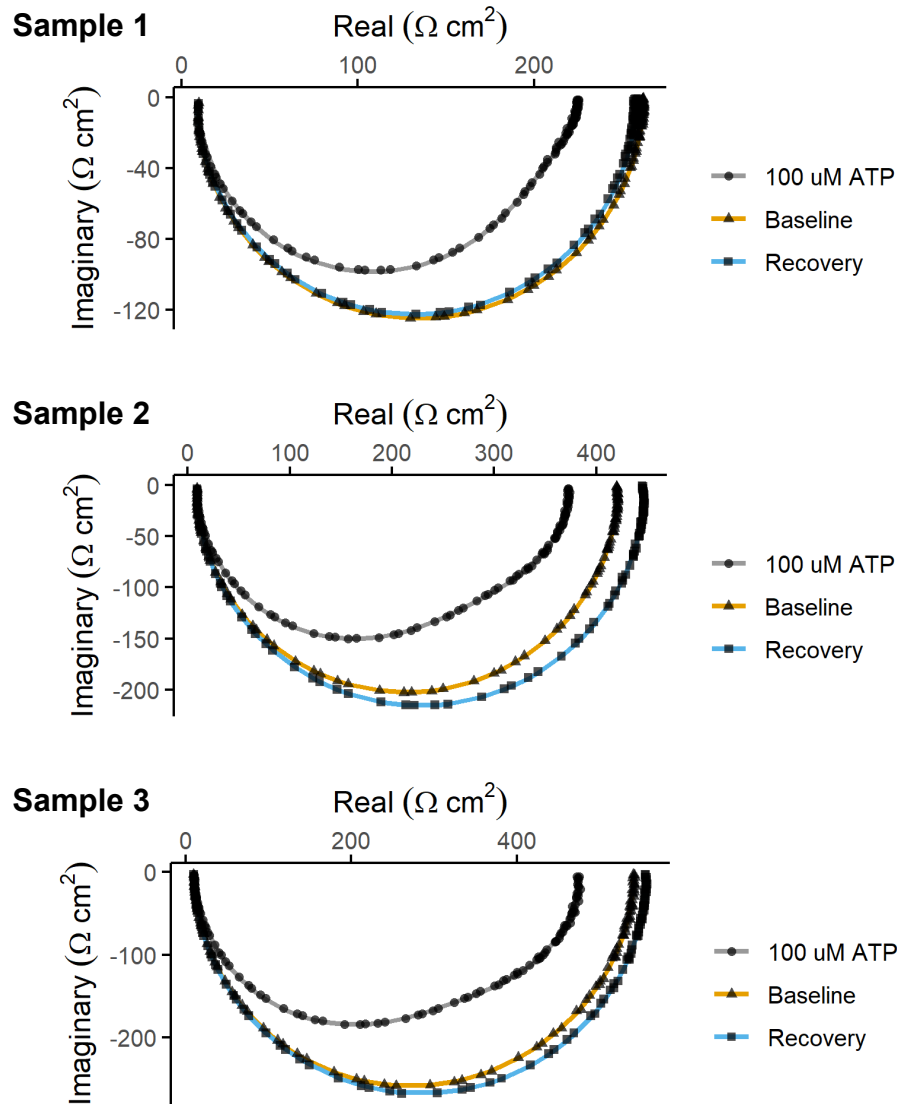


Figure 4.10: Example Nyquist diagrams of iPSC-RPE (Z8) before, during, and after ATP exposure. Samples 1, 2, and 3 match the panels in Figure 3.6 and Figure 3.7. Baseline condition corresponds to the impedance measurement immediately before apical ATP, 100 uM ATP corresponds to the impedance measurement during apical application of ATP ( $t \approx 6$  min), and recovery corresponds to the impedance measurement after ATP washout ( $t \approx 30$  min). Points on the plot correspond to measured data and the lines correspond to the best fit from the EIS circuit model in Figure 4.1B.

For all 3 samples tested in Figure 4.10, a notable change in the shape of the Nyquist diagram during ATP compared to the baseline was detected. Furthermore, the baseline and recovery Nyquist diagrams appear to be nearly identical for all samples; indicating that the application of apical ATP was reversible. Recall that in Figure 3.6 and Figure 3.7,

sample 1 had an inverse apical membrane response compared to samples 2 and 3. Instead of increasing during apical ATP - as expected for healthy RPE - apical resistance decreased. When looking at Figure 4.10, a concomitant variation appears in the overall shape of the Nyquist plot for sample 1 compared to sample 2 and 3. Therefore, the voltage divider ratio ( $a = R_a/R_b$ ) was compared, quantitatively, to the following extracellular EIS properties: time constant ratio ( $\tau_1/\tau_2$ ), total tissue capacitance ( $C_t$ ), and total tissue resistance ( $R_t$ ) in Figure 4.11.

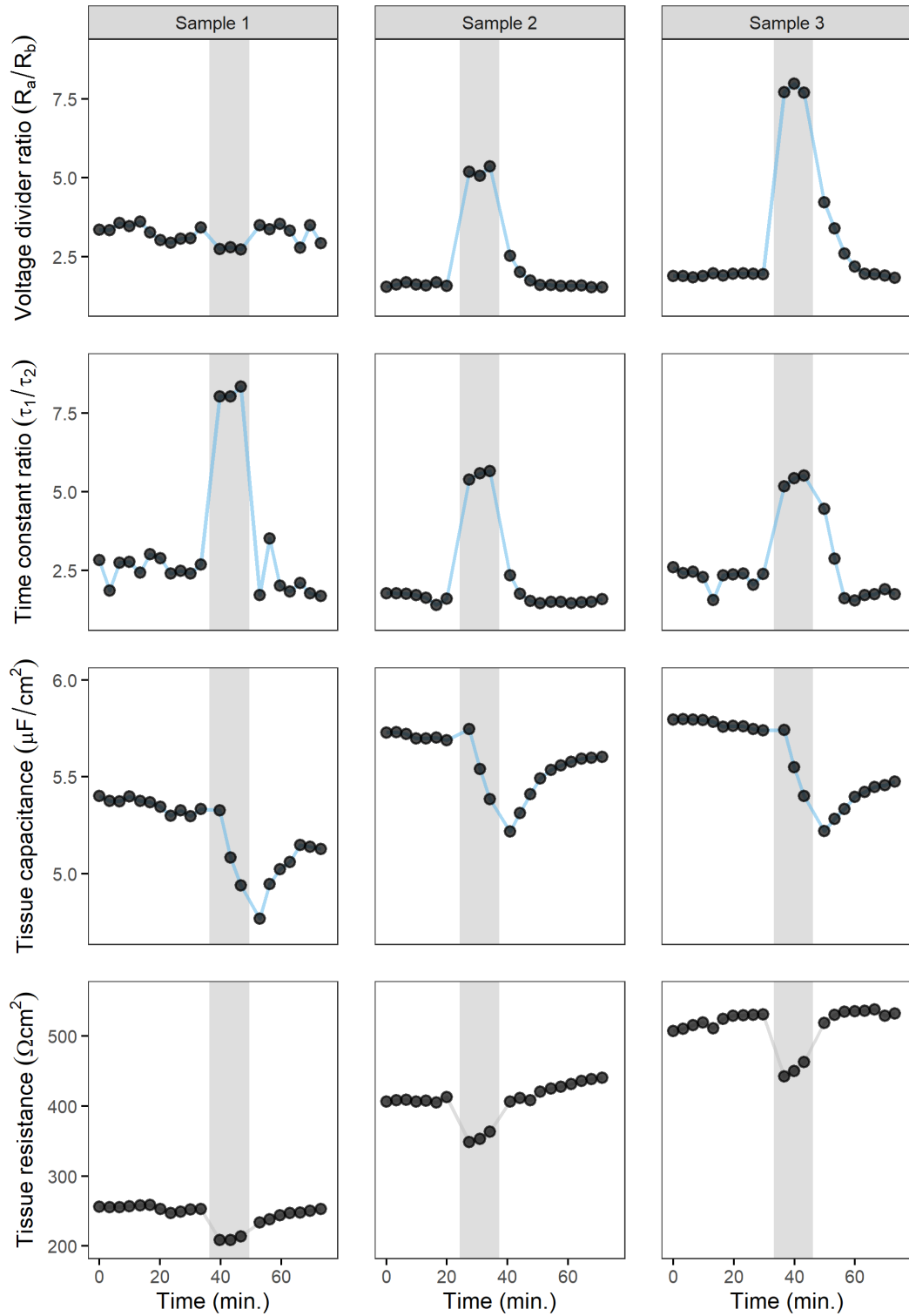


Figure 4.11: Quantitative comparison between extracellular EIS and the voltage divider ratio (a). Points on the plot correspond to measured data, and the grey box in the background indicate ATP exposure.

In this figure, the proportional decrease in tissue resistance and tissue capacitance relative to baseline during ATP exposure were approximately equal amongst all plots despite sample 1 starting at lower baseline values (samples 1, 2, and 3 are a subset of data included in Figure 4.6 and Figure 4.8 normalized Üssing chamber traces). Interestingly, the voltage divider ratio and time constant ratio have nearly identical magnitudes during baseline readings. In fact, the exact magnitude of all time constant and voltage divider ratios were nearly identical - per sample - during baseline measurements before apical ATP. However, during ATP exposure, sample 1 had a time constant ratio deflection that was nearly double samples 2 and 3. Furthermore, all time ratio constants increased in magnitude, despite the direction that the voltage divider ratio changed. This is an expected limitation of extracellular EIS measurements because, without an intracellular electrode to identify the polarity of the time constant ratios (namely, should the time constant be  $\tau_1/\tau_2$  or  $\tau_2/\tau_1$ ), the experimenter must predetermine - in the fitting algorithm - if the resultant time constant ratio is greater than or less than 1. Despite this limitation, the time constant ratio seems to quantitatively measure a difference between sample 1 and samples 2 and 3. In future work, the magnitude of this evoked response should be explored in greater detail. In particular, the intracellular techniques presented in Chapter 3 could be leveraged to examine which membrane properties most significantly contribute to the magnitude of the time constant ratio changes. Perhaps, providing scientists with a measurement capable of distinguishing membrane-specific variation between epithelia, non-invasively.

#### 4.2.3 Briefly exploring the potential links between cell morphology and capacitance

During cell culture, it is imperative that sensitive, yet rapid and non-invasive techniques exist to assess cell line variability, in-line or at-line. In particular, iPSCs still suffer from notable variations during culture, which seem to be unrelated to cell line, seeding date, passage, or a number of other starting points. Thus, for iPSCs to become a standardized therapy and drug discovery platform, it would be tremendously beneficial for scientists

to have quantitative metrics that are proven to be sensitive to cell line specific properties. Since electrophysiological parameters described in this thesis seem to lend useful insights into cell line-specific deviations (e.g., Figure 3.6 sample 3 vs. sample 1 and sample 2), EIS was performed across 3 donor iPSC-RPE cell lines (named AMDCD, Z8, and D3C) to investigate how consistent these extracellular electrophysiology terms are, per culture, and if there was any distinct clustering between cell lines.

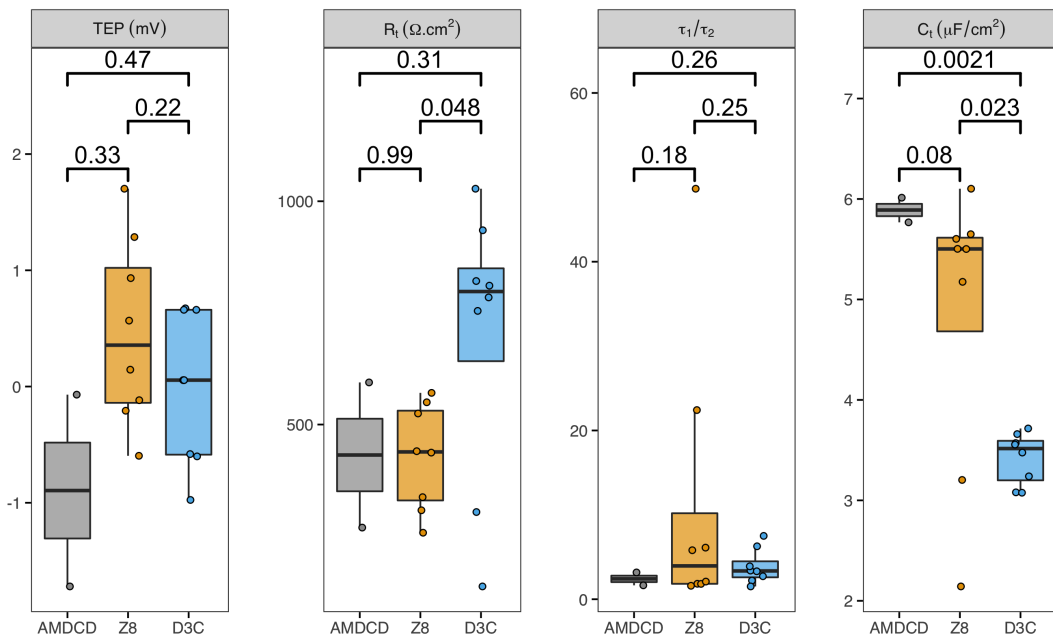


Figure 4.12: Extracellular EIS properties for 3 iPSC-RPE cell lines. A t-test was performed between all permutations of groups to evaluate statistically significant differences between cell lines, and the corresponding p-value is displayed in the brackets above. Each point on the plot corresponds to a unique Transwell.

From Figure 4.12, it seems that the strongest clustering per cell line - if any - is tissue capacitance. As established in Equation 1.5, capacitance is a function of membrane dielectric constant ( $\epsilon$ ), the membrane surface area ( $A$ ), and the membrane thickness ( $d$ ). These terms describe the composition and the structure of the cell membrane, and are traditionally difficult to quantify.

Conveniently, studying some of the morphological properties of each cell in large tissue samples (e.g., the entire human eye) has been a focus of my collaborators at the NEI.

To study these properties, a machine learning-based technique - called REShAPE - was developed that detects and draws complete cell borders. The overall workflow and output of this process is shown in Figure 4.13.

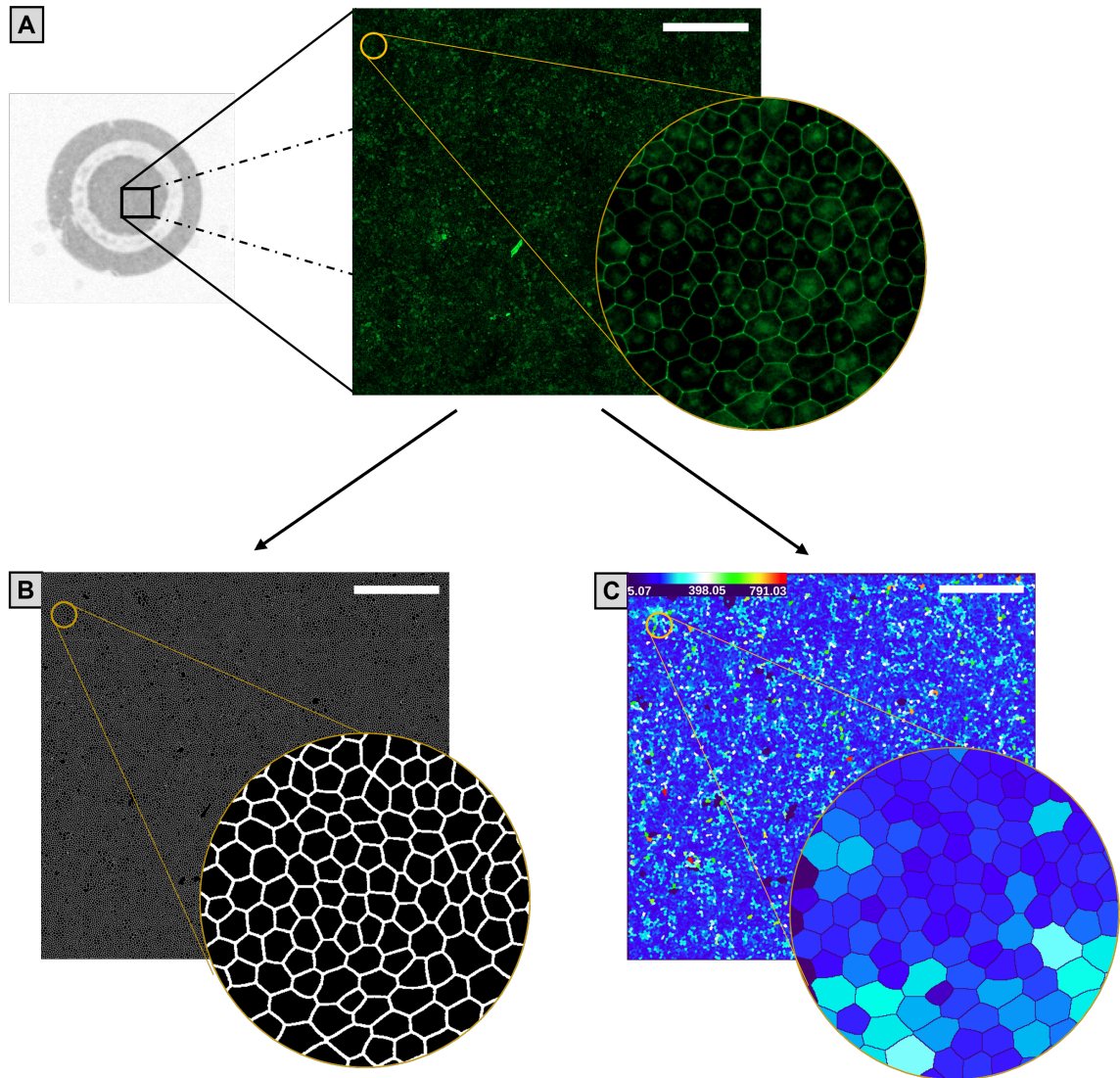


Figure 4.13: REShAPE morphology from fluorescent imaging of a transwell punch-out measured with EIS. (A) 7 mm iPSC-RPE (D3C) punch-out measured with EIS. The lighter ring is generated by the Üssing chamber apical lid clamping down on the cells to create an electrical separation between apical and basal chambers. These cells were stained against ZO-1 to visualize tight junctions as shown in the inset and magnification window. (B) The stained image was processed in REShAPE and the corresponding automatic border detection is shown in this panel and magnification window. (C) REShAPE takes the cell borders and calculates cell-specific area for thousands of cells (color temperature minimum is  $5.07 \mu\text{m}^2$  and maximum is  $791.03 \mu\text{m}^2$ ). All size scale bars (white) are  $500 \mu\text{m}$ .

The REShape algorithm extracts numerous parameters that describe the cross-sectional morphology of epithelia. For example, it assigns a “hexagonality” score based on how close the shape of a single cell is to a perfect hexagon. Amongst the numerous parameters quantified by REShape, it can calculate the cross-sectional area for each cell in an image (Figure 4.14).

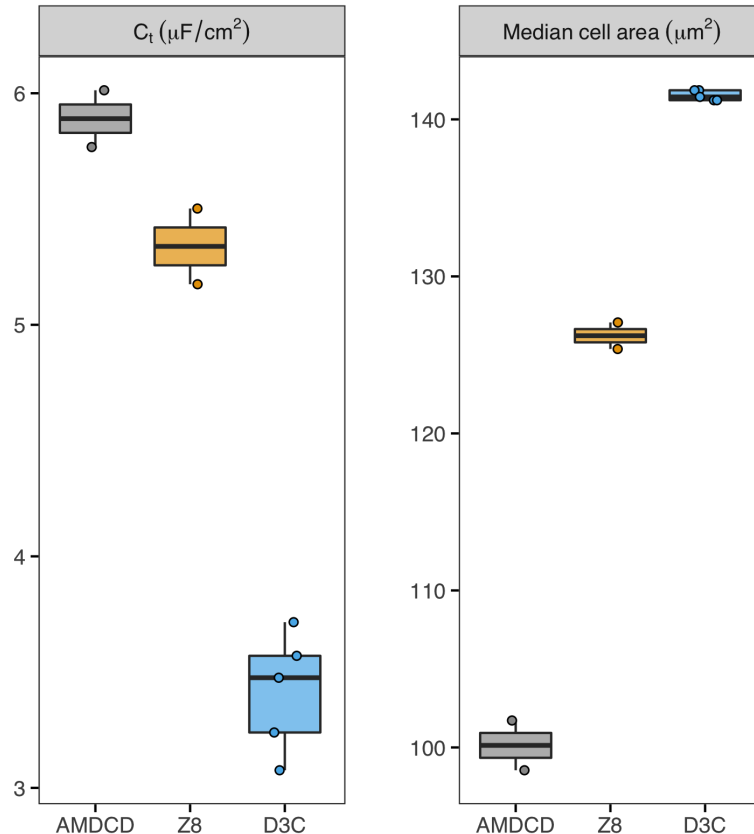


Figure 4.14: An example of how EIS and REShape can be leveraged to investigate the relationships between tissue capacitance and cell cross-sectional area. A subset of iPSC-RPE from Figure 4.12, were stained against ZO-1 and processed using REShape to get the cross-sectional area for each cell. The median value for each tissue sample, is depicted in this figure and collected per cell line.

Interestingly, the median cell cross-sectional area appears to be inversely proportional to cell capacitance. It is possible that the effective cell surface area per unit cross-sectional area actually increases as cell density increases. Briefly, cell density is inversely proportional to cell cross-sectional area because epithelia share borders with their neighbors via

tight junctions. However, with the sample sizes presented in this section, these conclusions are only speculative. To test this hypothesis, a larger variety of cell lines (and tissues per cell line) must be collected and similarly analyzed. Furthermore, the dielectric effects and the effective membrane thickness may also play a role in the measured tissue capacitance, conflating the interpretation of the theory presented in this paragraph.

Credence to this complication can be observed in the D3C cell line shown in Figure 4.14. Specifically, the median cross-sectional area of all D3C tissues had an average value of  $141.6 \pm 0.3 \mu\text{m}^2$  ( $\pm$  standard deviation). The standard deviation is approximately 0.2% of the average. However, the tissue capacitance had an average of  $3.4 \pm 0.2 \mu\text{F}/\text{cm}^2$ . Thus, for tissue capacitance, the standard deviation is approximately equal to 6% of the mean. A mismatch in the relative errors should - at a minimum - require the experimenter to hesitate before drawing conclusions without additional evidence. However, despite these complications, the trends depicted in Figure 4.14 do warrant further study.

### **4.3 Conclusions**

In this chapter, EIS was added to a suite of extracellular physiology and morphological tests and was found to provide critical, non-invasive insights into - previously unobservable - cell function and tissue variability. For example, tissue capacitance was the only extracellular metric that was able to detect a difference in chamber-specific epithelial response during apical application of ATP; likely caused by differences in the perfusion and Üssing chamber mixing rates. Furthermore, the ratio of time constants seems to be a useful approximation of the intracellular voltage divider ratio. The voltage divider ratio is a membrane-specific property that requires expensive equipment and extensive lab space. Regardless, collaborators at the NEI have shown that the voltage divider ratio is a critical metric for identifying tissue-to-tissue variability. Therefore, as shown in this chapter, the extracellular measurement of time constant ratios provides a non-invasive approximation of this critical parameter that can be performed with (relatively) little equipment or

lab space; enabling the evaluation of membrane-specific electrophysiology accessible to a larger contingent of laboratories. Finally, the link between tissue capacitance and cell morphology was studied. It appears that tissue capacitance is inversely proportional to cell cross-sectional area (as measured with REShAPE). This relationship is likely caused by the cell packing density resulting in smaller cells having a higher surface area per unit cross-sectional area ratio. This relationship was studied using REShAPE, confocal, and SEM imaging techniques but does not require (1) the destructive processes of fixing and staining the cells prior to measurement and (2) can be performed in less than 5 min with commercially available devices (e.g., EndOhm-12 from WPI) rather than a multi-day process with expensive imaging tools.

## **CHAPTER 5**

### **RESEARCH CONCLUSIONS AND FUTURE WORK**

Epithelia are barrier-type cells that regulate the transport of materials into and out of the body. Dysfunction of these cells is implicated in numerous diseases such as cystic fibrosis, age-related macular degeneration, and diabetes. Since the discovery of iPSCs by Takahashi and Yamanaka in 2006, scientists around the world have begun utilizing iPSC-based therapies to halt, and potentially reverse, the progression of these diseases. For epithelia-based therapies, validation of tissue polarity and function is an essential component of a thorough physiological exam, and are commonly performed electrochemically, but existing methods are some combination of (1) destructive to the cells, (2) incomplete, (3) extremely difficult, and (4) low throughput (e.g., 1-2 tissues/day). Therefore, in this work, novel tools and measurement techniques were developed to study epithelial cell function that address these issues.

#### **5.1 Summary of major contributions**

In this work, four major objectives were completed. First, an algorithm that automates the insertion of a pipette into the cytoplasm of a single cell was developed (chapter 2). This algorithm outperforms a highly trained expert and makes the technique more accessible for a broader field of scientists. Next, a new mathematical model was developed that simultaneously utilizes EIS and the newly automated intracellular technique to extract membrane-specific properties of epithelia (chapter 3). Previously, the only techniques for measuring membrane-specific properties of epithelia involved (1) making assumptions about cell function, (2) often requiring an extra measurement prior to each experiment (e.g., measuring paracellular flux to estimate the shunt resistance), and (3) were highly sensitive to measurement bias due to pipette clogging or poor membrane-to-pipette seals. These

old techniques can lead to misleading or possibly incorrect calculations of cell function if the tissue being tested is dysfunctional; invalidating the aforementioned assumptions which is especially pertinent if the objective of an experiment is to identify dysfunctional cells. Furthermore, it was demonstrated that tissue capacitance appears to be linked with cell cross-sectional area, and, after preliminary tests, appears to provide the most sensitive extracellular electrophysiological identifier of cell-line specific variability (chapter 4). Finally, extracellular EIS was proven to be a suitable compromise between the comprehensive, yet slow and invasive, intracellular measurements and the fast, yet simple, extracellular measurements of epithelial function (chapter 4). Specifically, EIS can provide a more sensitive analysis of membrane-specific function by utilizing a ratio of time constants that mimics the voltage divider ratio; a membrane-specific property only measurable when utilizing intracellular techniques.

## **5.2 Future work**

This dissertation provides a suite of tools that can become the platform for future iPSC-based epithelial function assays. These tools, as described in this dissertation, have limitations that future research can improve upon. For starters, the algorithm for automatic pipette insertion is merely one aspect of the challenges involved in intracellular recordings. It turns out that pipette insertion is highly dependent on the quality of the pipette that has been fabricated prior to installation in the robot. This fabrication technique suffered greatly from changing weather and frequently resulted in multiple days of re-tuning the pipette pulling machine.

Our lab has developed and validated a technique for reusing old patch-clamp pipettes, but this technique has never been tested with intracellular sharps pipettes (approximately 1/10th the diameter of a patch-clamp pipette) [88]. If cleaning works with sharp pipettes - such as those used in this dissertation - more time could be spent fabricating individual pipettes with a “perfect” geometry because they could be utilized for multiple recordings.

The ability to reuse a single pipette would completely eliminate the issues with pipette variability stemming from inclement weather, and, as observed in the lab, vastly improve throughput.

Another limitation with the research presented in this work is the time required to complete a single EIS measurement. Each time a measurement was performed, a series of no more than 5 simultaneous frequencies were applied across the tissue, logarithmically spaced between 0.1 Hz and 10 kHz. To ensure that no surprising data were missed, approximately 100 discrete frequencies were clamped across the epithelia which took about 2 min to complete. Therefore, the frequencies utilized for EIS can be optimized to include only the frequencies that are minimally sufficient for capturing the entire impedance locus on the Nyquist diagram. Furthermore, techniques for measuring a larger spectrum of frequencies, in less time, can also be investigated (e.g., chirp, impulse, and power-spectrum-optimized broadband noise). These improvements would further reduce the time required to measure the tissue. Right now, the measurements are too slow to capture a majority of the dynamic behavior of epithelia. For example, Peterson et. al. [59], studied the multi-phase response of bovine RPE to ATP where he described 2 early phases of the response that occur in less than 3 min; thus, these phases cannot be studied with the measurement process utilized in this dissertation.

A third direction this work can go is to further investigate the links between cell capacitance, morphology, and function. In this dissertation, a few likely links were presented, but a comprehensive suite of scientific experiments should be performed to validate these claims and enhance scientific understanding. For example, experiments could be performed to intentionally modify the surface area to unit volume ratio of different cell lines and attempt to link critical cell function to these properties. For example, cell swelling and shrinking can be induced by adjusting the osmolarity of the apical and basal solutions [89]. By inducing swelling while recording extracellular properties and monitoring cell swelling with intracellular tetramethylammonium (TMA) using double-barreled K-resin microelec-

trodes, physiological links may be discovered [89]. Furthermore, experiments could be devised to replicate the experiments described in chapter 4 in order to determine why the tissue capacitance and the time constant ratio had a different response to apical ATP, depending on the chamber utilized to perform the experiment. It may be possible that there are dosage-sensitive pathways in epithelia that are difficult to resolve with traditional extracellular techniques, but, with the techniques described in this dissertation, a suite of well-designed experiments could attempt to resolve this interesting conundrum.

## REFERENCES

- [1] V. A. Shaposhnik, "Evolution of the membrane electrochemistry," *Russian Journal of Electrochemistry*, vol. 38, no. 8, pp. 800–805, 2002.
- [2] W. R. Amberson and H. Klein, "The influence of pH upon the concentration potentials across the skin of the frog," *Journal of General Physiology*, vol. 11, no. 6, pp. 823–841, 1928.
- [3] O. Alvarez and R. Latorre, "The enduring legacy of the "constant-field equation" in membrane ion transport," *Journal of General Physiology*, vol. 149, no. 10, pp. 911–920, 2017.
- [4] S. S. Miller and R. H. Steinberg, "Passive ionic properties of frog retinal pigment epithelium," *The Journal of Membrane Biology*, vol. 36, no. 1, pp. 337–372, 1977.
- [5] W. R. Skach, *Cystic Fibrosis Methods and Protocols*. 2002, ISBN: 0896038971.
- [6] S. C. Tang, J. C. Leung, L. Y. Chan, A. W. Tsang, and K. N. Lai, "Activation of tubular epithelial cells in diabetic nephropathy and the role of the peroxisome proliferator-activated receptor- $\gamma$  agonist," *Journal of the American Society of Nephrology*, vol. 17, no. 6, pp. 1633–1643, 2006.
- [7] K. J. Miyagishima *et al.*, "In Pursuit of Authenticity: Induced Pluripotent Stem Cell-Derived Retinal Pigment Epithelium for Clinical Applications.," *Stem cells translational medicine*, vol. 5, no. 11, pp. 1562–1574, Nov. 2016.
- [8] I. Bhutto and G. Luttly, "Understanding age-related macular degeneration (AMD): Relationships between the photoreceptor/retinal pigment epithelium/Bruch's membrane/choriocapillaris complex," *Molecular Aspects of Medicine*, vol. 33, no. 4, pp. 295–317, Aug. 2012.
- [9] A. C. Bird, "Bruch's membrane change with age.," pp. 166–168, 1992.
- [10] A. C. Bird, "Review series Therapeutic targets in age-related macular disease," *The Journal of Clinical Investigation*, vol. 120, no. 9, pp. 3033–3041, 2010.
- [11] M. K. Jones, B. Lu, S. Girman, and S. Wang, "Cell-based therapeutic strategies for replacement and preservation in retinal degenerative diseases," *Progress in Retinal and Eye Research*, vol. 58, pp. 1–27, 2017.
- [12] R. Klein, C. Chou, K. BK, X. Zhang, M. SM, and S. JB, "Prevalence of age-related macular degeneration in the us population," *Archives of Ophthalmology*, vol. 129, no. 1, pp. 75–80, Jan. 2011.

- [13] L. S. Lim, P. Mitchell, J. M. Seddon, F. G. Holz, and T. Y. Wong, “Age-related macular degeneration,” *The Lancet*, vol. 379, no. 9827, pp. 1728–1738, 2012.
- [14] W. L. Wong *et al.*, “Global prevalence of age-related macular degeneration and disease burden projection for 2020 and 2040: a systematic review and meta-analysis,” *The Lancet Global Health*, vol. 2, no. 2, e106–e116, Feb. 2014.
- [15] H. H. USSING and K. ZERAHN, “Active transport of sodium as the source of electric current in the short-circuited isolated frog skin.,” *Acta physiologica Scandinavica*, vol. 23, no. 2-3, pp. 110–27, Aug. 1951.
- [16] L. L. Clarke, “A guide to Ussing chamber studies of mouse intestine,” *American Journal of Physiology-Gastrointestinal and Liver Physiology*, vol. 296, no. 6, G1151–G1166, Jun. 2009.
- [17] M. Juusola, A. Dau, L. Zheng, and D. Rien, “Electrophysiological Method for Recording Intracellular Voltage Responses of Drosophila Photoreceptors and Interneurons to Light Stimuli In Vivo.,” *Journal of visualized experiments : JoVE*, no. 112, pp. 1–16, Jun. 2016.
- [18] A. Maminishkis *et al.*, “Confluent Monolayers of Cultured Human Fetal Retinal Pigment Epithelium Exhibit Morphology and Physiology of Native Tissue,” *Investigative Ophthalmology & Visual Science*, vol. 47, no. 8, p. 3612, Aug. 2006. arXiv: NIHMS150003.
- [19] M. Kokkinaki, N. Sahibzada, and N. Golestaneh, “Human iPS-derived retinal pigment epithelium (RPE) cells exhibit ion transport, membrane potential, polarized VEGF secretion and gene expression pattern similar to native RPE,” *Stem Cells*, vol. 29, no. 5, pp. 825–835, 2011.
- [20] E. V. Hernandez, J. G. Hu, D. A. Frambach, and R. P. Gallemore, “Potassium conductances in cultured bovine and human retinal pigment epithelium,” *Investigative Ophthalmology and Visual Science*, vol. 36, no. 1, pp. 113–122, 1995.
- [21] J. G. Hu, R. P. Gallemore, D. Bok, and D. A. Frambach, “Chloride transport in cultured fetal human retinal pigment epithelium,” *Experimental Eye Research*, vol. 62, no. 4, pp. 443–448, 1996.
- [22] S. Bialek and S. S. Miller, “K<sup>+</sup> and Cl<sup>-</sup> transport mechanisms in bovine pigment epithelium that could modulate subretinal space volume and composition.,” *The Journal of physiology*, vol. 475, no. 3, pp. 401–17, 1994.
- [23] S. Blaug, K. Hybiske, J. Cohn, G. L. Firestone, T. E. Machen, and S. S. Miller, “ENaC- and CFTR-dependent ion and fluid transport in mammary epithelia,” *Amer-*

- ican Journal of Physiology-Cell Physiology*, vol. 281, no. 2, pp. C633–C648, Aug. 2001.
- [24] S. Blaug, J. Rymer, S. Jalickee, and S. S. Miller, “P2 purinoceptors regulate calcium-activated chloride and fluid transport in 31EG4 mammary epithelia,” *American Journal of Physiology-Cell Physiology*, vol. 284, no. 4, pp. C897–C909, Apr. 2003.
- [25] C. U. Cotton, M. J. Stutts, M. R. Knowles, J. T. Gatzky, and R. C. Boucher, “Abnormal apical cell membrane in cystic fibrosis respiratory epithelium. An in vitro electrophysiologic analysis,” *Journal of Clinical Investigation*, vol. 79, no. 1, pp. 80–85, Jan. 1987.
- [26] P. Rothenberg, L. Reuss, and L. Glaser, “Serum and epidermal growth factor transiently depolarize quiescent BSC-1 epithelial cells,” *Proceedings of the National Academy of Sciences of the United States of America*, vol. 79, no. 24, pp. 7783–7, Dec. 1982.
- [27] J. Tang, F. J. Abramcheck, W. Van Driessche, and S. I. Helman, “Electrophysiology and noise analysis of K<sup>+</sup>-depolarized epithelia of frog skin,” *American Journal of Physiology-Cell Physiology*, vol. 249, no. 5, pp. C421–C429, Nov. 1985.
- [28] M. J. Welsh, “Anthracene-9-carboxylic acid inhibits an apical membrane, chloride conductance in canine tracheal epithelium,” *The Journal of Membrane Biology*, vol. 78, no. 1, pp. 61–71, 1984.
- [29] R. H. Quinn and S. S. Miller, “Ion transport mechanisms in native human retinal pigment epithelium,” *Investigative Ophthalmology and Visual Science*, vol. 33, no. 13, pp. 3513–3527, 1992.
- [30] K. Takahashi and S. Yamanaka, “Induction of Pluripotent Stem Cells from Mouse Embryonic and Adult Fibroblast Cultures by Defined Factors,” *Cell*, vol. 126, no. 4, pp. 663–676, 2006.
- [31] K. J. Miyagishima, Q. Wan, S. S. Miller, and K. Bharti, “A basis for comparison: sensitive authentication of stem cell derived RPE using physiological responses of intact RPE monolayers,” *Stem cell and translational investigation*, vol. 4, 2017.
- [32] J. Zhu, M. Slevin, B. Q. Guo, and S. R. Zhu, “Induced pluripotent stem cells as a potential therapeutic source for corneal epithelial stem cells,” *International Journal of Ophthalmology*, vol. 11, no. 12, pp. 2004–2010, 2018.
- [33] R. Sharma *et al.*, “Clinical-grade stem cell–derived retinal pigment epithelium patch rescues retinal degeneration in rodents and pigs,” *Science Translational Medicine*, vol. 11, no. 475, eaat5580, Jan. 2019.

- [34] A. J. Miller *et al.*, “In Vitro Induction and In Vivo Engraftment of Lung Bud Tip Progenitor Cells Derived from Human Pluripotent Stem Cells,” *Stem Cell Reports*, vol. 10, no. 1, pp. 101–119, 2018.
- [35] Q. Hassan, S. Ahmadi, and K. Kerman, “Recent advances in monitoring cell behavior using cell-based impedance spectroscopy,” *Micromachines*, vol. 11, no. 6, 2020.
- [36] C. F. Lewallen *et al.*, “High-yield, automated intracellular electrophysiology in retinal pigment epithelia,” *Journal of Neuroscience Methods*, vol. 328, no. April, p. 108 442, Sep. 2019.
- [37] M. Campbell and P. Humphries, “The Blood-Retina Barrier,” in *Biology and Regulation of Blood-Tissue Barriers*, Springer, New York, NY, 2013, pp. 70–84.
- [38] D. P. Joseph and S. S. Miller, “Apical and basal membrane ion transport mechanisms in bovine retinal pigment epithelium,” *The Journal of Physiology*, vol. 435, no. 1, pp. 439–463, 1991.
- [39] V. S. Parikh *et al.*, “Nonleaking Cystoid Macular Edema as a Presentation of Hydroxychloroquine Retinal Toxicity,” *Ophthalmology*, vol. 123, no. 3, pp. 664–666, Mar. 2016.
- [40] O. E. Makri, F. N. Tsapardoni, P. Plotas, N. Ifantis, P. T. Xanthopoulou, and C. D. Georgakopoulos, “Cystoid macular edema associated with preservative-free latanoprost after uncomplicated cataract surgery: case report and review of the literature,” *BMC Research Notes*, vol. 10, no. 1, p. 127, Dec. 2017.
- [41] G. Heath, A. Airody, and R. P. Gale, “The Ocular Manifestations of Drugs Used to Treat Multiple Sclerosis,” *Drugs*, vol. 77, no. 3, pp. 303–311, Mar. 2017.
- [42] C. L. Montana and R. S. Apte, “MEKanismis of a Serous Complication,” *JAMA Ophthalmology*, vol. 135, no. 5, p. 413, May 2017.
- [43] L. Da Cruz *et al.*, “Phase 1 clinical study of an embryonic stem cell-derived retinal pigment epithelium patch in age-related macular degeneration,” *Nature Biotechnology*, vol. 36, no. 4, pp. 1–10, 2018.
- [44] A. H. Kashani *et al.*, “A bioengineered retinal pigment epithelial monolayer for advanced, dry age-related macular degeneration,” *Science translational medicine*, vol. 10, no. 435, eaao4097, Apr. 2018.
- [45] R. A. Linsenmeier and R. H. Steinberg, “Effects of hypoxia on potassium homeostasis and pigment epithelial cells in the cat retina,” *J Gen Physiol*, vol. 84, no. 6, pp. 945–970, 1984.

- [46] R. A. Linsenmeier and R. H. Steinberg, "Origin and sensitivity of the light peak in the intact cat eye," *The Journal of Physiology*, vol. 331, no. 1, pp. 653–673, Oct. 1982.
- [47] B. A. Hughes, S. S. Miller, D. P. Joseph, and J. L. Edelman, "cAMP stimulates the Na<sup>+</sup>-K<sup>+</sup> pump in frog retinal pigment epithelium," *Am J Physiol*, vol. 254, no. 1 Pt 1, pp. C84–98, 1988.
- [48] J. Immel and R. H. Steinberg, "Spatial buffering of K<sup>+</sup> by the retinal pigment epithelium in frog," *J Neurosci*, vol. 6, no. 11, pp. 3197–3204, 1986.
- [49] M. la Cour, H. Lund-Andersen, and T. Zeuthen, "Potassium transport of the frog retinal pigment epithelium: autoregulation of potassium activity in the subretinal space.," *The Journal of Physiology*, vol. 375, no. 1, pp. 461–479, 1986.
- [50] S. S. Miller and R. H. Steinberg, "Potassium modulation of taurine transport across the frog retinal pigment epithelium," *J Gen Physiol*, vol. 74, no. 2, pp. 237–259, 1979.
- [51] J. L. Kreindler, A. D. Jackson, P. A. Kemp, R. J. Bridges, and H. Danahay, "Inhibition of chloride secretion in human bronchial epithelial cells by cigarette smoke extract," *American Journal of Physiology - Lung Cellular and Molecular Physiology*, vol. 288, no. 5 32-5, pp. 894–902, 2005.
- [52] D. P. Joseph, "Alpha-1-adrenergic modulation of K and Cl transport in bovine retinal pigment epithelium," *The Journal of General Physiology*, vol. 99, no. 2, pp. 263–290, Feb. 1992.
- [53] K. Takahashi, M. Narita, M. Yokura, T. Ichisaka, and S. Yamanaka, "Human induced pluripotent stem cells on autologous feeders," *PLoS ONE*, vol. 4, no. 12, pp. 2–7, 2009.
- [54] M. Ferrer *et al.*, "A Multiplex High-Throughput Gene Expression Assay to Simultaneously Detect Disease and Functional Markers in Induced Pluripotent Stem Cell-Derived Retinal Pigment Epithelium," *STEM CELLS Translational Medicine*, vol. 3, no. 8, pp. 911–922, 2014.
- [55] S. B. Kodandaramaiah *et al.*, "Assembly and operation of the autopatcher for automated intracellular neural recording in vivo," *Nature Protocols*, vol. 11, no. 4, pp. 634–654, Mar. 2016.
- [56] L. Lu, "Retinal pigment epithelial cell function on substrates with chemically micropatterned surfaces," *Biomaterials*, vol. 20, no. 23-24, pp. 2351–2361, Dec. 1999.

- [57] W. C. Li, S. R. Soffe, and A. Roberts, “A direct comparison of whole cell patch and sharp electrodes by simultaneous recording from single spinal neurons in frog tadpoles,” *Journal of Neurophysiology*, vol. 92, no. 1, pp. 380–386, 2004.
- [58] A. V. Dmitriev, V. I. Govardovskii, and R. H. Steinberg, “Light-induced changes of principal extracellular ions, and the extracellular space volume in the chick retina,” *Investigative Ophthalmology and Visual Science*, vol. 37, no. 3, pp. 1157–1167, 1996.
- [59] W. M. Peterson, C. Meggyesy, K. Yu, and S. S. Miller, “Extracellular ATP activates calcium signaling, ion, and fluid transport in retinal pigment epithelium,” *Journal of Neuroscience*, vol. 17, no. 7, pp. 2324–2337, 1997.
- [60] G. Holst *et al.*, “Autonomous patch clamp robot for functional characterization of neurons in vivo : development and application to mouse visual cortex,” *Journal of Neurophysiology*, pp. 2341–2357, 2019.
- [61] I. Kolb *et al.*, “PatcherBot: A single-cell electrophysiology robot for adherent cells and brain slices,” *Journal of Neural Engineering*, vol. 16, no. 4, 2019.
- [62] E. Schifferdecker and E. Frömter, “The AC impedance of necturus gallbladder epithelium,” *Pflügers Archiv European Journal of Physiology*, vol. 377, no. 2, pp. 125–133, 1978.
- [63] S. M. Krug, M. Fromm, and D. Günzel, “Two-path impedance spectroscopy for measuring paracellular and transcellular epithelial resistance,” *Biophysical Journal*, vol. 97, no. 8, pp. 2202–2211, 2009.
- [64] G. Kottra and E. Frömter, “Rapid determination of intraepithelial resistance barriers by alternating current spectroscopy. II. Test of model circuits and quantification of results,” *Pflugers Archiv : European journal of physiology*, vol. 402, no. 4, pp. 421–32, Dec. 1984.
- [65] N. K. Wills, S. A. Lewis, and D. C. Eaton, “Active and passive properties of rabbit descending colon: A microelectrode and nystatin study,” *The Journal of Membrane Biology*, vol. 45, no. 1-2, pp. 81–108, 1979.
- [66] N. K. Wills and C. Clausen, “Transport-dependent alterations of membrane properties of mammalian colon measured using impedance analysis,” *The Journal of membrane biology*, vol. 95, no. 1, pp. 21–35, 1987.
- [67] N. Onnela, V. Savolainen, K. Juuti-Uusitalo, H. Vaajasaari, H. Skottman, and J. Hyttinen, “Electric impedance of human embryonic stem cell-derived retinal pigment epithelium,” *Medical and Biological Engineering and Computing*, vol. 50, no. 2, pp. 107–116, 2012.

- [68] V. Savolainen *et al.*, “Impedance spectroscopy in monitoring the maturation of stem cell-derived retinal pigment epithelium,” *Annals of Biomedical Engineering*, vol. 39, no. 12, pp. 3055–3069, 2011.
- [69] G. Linz, S. Djeljadini, L. Steinbeck, G. Köse, F. Kiessling, and M. Wessling, “Cell barrier characterization in transwell inserts by electrical impedance spectroscopy,” *Biosensors and Bioelectronics*, vol. 165, no. May, p. 112 345, 2020.
- [70] K. A. Cottrill, R. J. Peterson, C. F. Lewallen, M. Koval, R. J. Bridges, and N. A. McCarty, “Sphingomyelinase decreases transepithelial anion secretion in airway epithelial cells in part by inhibiting CFTR-mediated apical conductance,” *Physiological Reports*, vol. 9, no. 15, pp. 1–17, 2021.
- [71] C. Clausen, S. A. Lewis, and J. M. Diamond, “Impedance analysis of a tight epithelium using a distributed resistance model,” *Biophysical Journal*, vol. 26, no. 2, pp. 291–317, 1979.
- [72] C. Clausen, P. S. Reinach, and D. C. Marcus, “Membrane transport parameters in frog corneal epithelium measured using impedance analysis techniques.,” *The Journal of membrane biology*, vol. 91, no. 3, pp. 213–25, 1986.
- [73] L. D. Robilliard, D. T. Kho, R. H. Johnson, A. Anchan, S. J. O’Carroll, and E. S. Graham, “The Importance of Multifrequency Impedance Sensing of Endothelial Barrier Formation Using ECIS Technology for the Generation of a Strong and Durable Paracellular Barrier.,” *Biosensors*, vol. 8, no. 3, Jul. 2018.
- [74] D. Günzel *et al.*, “From TER to trans- and paracellular resistance: Lessons from impedance spectroscopy,” *Annals of the New York Academy of Sciences*, vol. 1257, no. 1, pp. 142–151, 2012.
- [75] F. Groeber *et al.*, “Impedance Spectroscopy for the Non-Destructive Evaluation of in Vitro Epidermal Models,” *Pharmaceutical Research*, vol. 32, no. 5, pp. 1845–1854, 2015.
- [76] T. Schmid, M. Bogdan, and D. Günzel, “Discerning Apical and Basolateral Properties of HT-29/B6 and IPEC-J2 Cell Layers by Impedance Spectroscopy, Mathematical Modeling and Machine Learning,” *PLoS ONE*, vol. 8, no. 7, pp. 1–12, 2013.
- [77] B. Srinivasan, A. R. Kolli, M. B. Esch, H. E. Abaci, M. L. Shuler, and J. J. Hickman, “TEER Measurement Techniques for In Vitro Barrier Model Systems,” *Journal of Laboratory Automation*, vol. 20, no. 2, pp. 107–126, Apr. 2015.
- [78] M. S. Awayda, W. Van Driessche, and S. I. Helman, “Frequency-dependent capacitance of the apical membrane of frog skin: Dielectric relaxation processes,” *Biophysical Journal*, vol. 76, no. 1 I, pp. 219–232, 1999.

- [79] W. Van Driessche, J. L. Kreindler, A. B. Malik, S. Margulies, S. A. Lewis, and K. J. Kim, "Interrelations/cross talk between transcellular transport function and paracellular tight junctional properties in lung epithelial and endothelial barriers," *American Journal of Physiology - Lung Cellular and Molecular Physiology*, vol. 293, no. 3, pp. 520–524, 2007.
- [80] D. G. Mărgineanu and W. Van Driessche, "Effects of millimolar concentrations of glutaraldehyde on the electrical properties of frog skin.," *The Journal of physiology*, vol. 427, pp. 567–81, Aug. 1990.
- [81] A. H. Gitter, M. Fromm, and J. D. Schulzke, "Impedance analysis for the determination of epithelial and subepithelial resistance in intestinal tissues," *Journal of Biochemical and Biophysical Methods*, vol. 37, no. 1-2, pp. 35–46, 1998.
- [82] S. A. Lewis and J. L. C. De Moura, "Apical Membrane Area of Rabbit Urinary Bladder Increases by Fusion of Intracellular Vesicles: An Electrophysiological Study," Tech. Rep., 1984, pp. 123–136.
- [83] N. J. Schaub *et al.*, "Deep learning predicts function of live retinal pigment epithelium from quantitative microscopy," *Journal of Clinical Investigation*, vol. 130, no. 2, pp. 1010–1023, 2020.
- [84] H. L. May-Simera *et al.*, "Primary Cilium-Mediated Retinal Pigment Epithelium Maturation Is Disrupted in Ciliopathy Patient Cells," *Cell Reports*, vol. 22, no. 1, pp. 189–205, 2018.
- [85] S. Tokuda and A. S. L. Yu, "Regulation of Epithelial Cell Functions by the Osmolality and Hydrostatic Pressure Gradients: A Possible Role of the Tight Junction as a Sensor," *International Journal of Molecular Sciences*, vol. 20, no. 14, p. 3513, 2019.
- [86] K. S. Spiegler, "Transport processes in ionic membranes," *Transactions of the Faraday Society*, vol. 54, pp. 1408–1428, 1958.
- [87] S. G. Schultz, "Transport across epithelia: Some basic principles," *Kidney International*, vol. 9, no. 2, pp. 65–75, 1976.
- [88] I. Kolb, W. A. Stoy, E. B. Rousseau, O. A. Moody, A. Jenkins, and C. R. Forrest, "Cleaning patch-clamp pipettes for immediate reuse," *Scientific Reports*, vol. 6, pp. 1–10, 2016.
- [89] J. S. Adorante and S. S. Miller, "Potassium-dependent volume regulation in retinal pigment epithelium is mediated by Na, K, Cl cotransport," *Journal of General Physiology*, vol. 96, no. 6, pp. 1153–1176, 1990.